E-610

PRODUCTION OF CHARMONIUM STATES IN 225 GEV/C PI-MINUS BERYLLIUM INTERACTIONS

BY

STEPHEN R. HAHN

B. S., University of Illinois, 1972
M. S., University of Illinois, 1973

THESIS

Submitted in partial fulfillment of the requirements
for the degree of Doctor of Philosophy in Physics
in the Graduate College of the
University of Illinois at Urbana-Champaign, 1983

Urbana, Illinois

PACS Index 13.85.Qk

PRODUCTION OF CHARMONIUM STATES IN 225 GEV/C PI-MINUS BERYLLIUM INTERACTIONS

Stephen R. Hahn, Ph. D.
Department of Physics
University of Illinois at Urbana-Champaign, 1983

This thesis reports on the analysis of data obtained during FNAL experiment E610. The Chicago Cyclotron Magnet Spectrometer was used to perform a study of the hadronic production of charmonium. A 225 GeV/c negative pion beam was incident on a beryllium target. The trigger required a dimuon signature which favored opposite sign muon pairs with a large combined p_T. A search was then made for χ mesons of the charmonium spectrum by combining J/ψ mesons found in the dimuon spectrum with photons detected in a large lead glass shower detector. These events were used to determine the fraction of J/ψs produced from χs. A $\psi(3685)$ signal seen in the dimuon spectrum was used to determine the fraction of J/ψs resulting from $\psi(3685)$. Assuming that these are the only particles decaying to J/ψ, we obtain the fraction of J/ψs produced directly in hadronic collisions— 0.58 ± 0.09 —which is relevant to the production mechanism for charmonium in strong interactions.

ACKNOWLEDGEMENTS

I would like to thank my colleagues on Fermilab Experiment E610—especially the professors and graduate students here at Illinois: Howard Budd, Lee Holloway, Lou Koester, Uli Kruse, Paul Schoessow, Pat Lukens, Tom Graff, and Wei-Guo Li. I owe a special debt of thanks to John Cooper (now at the University of Pennsylvania) and Mike Shupe (now at the University of Minnesota) for both being constant sources of inspiration and encouragement. At the top of the list stands my advisor, Bob Sard, whose understanding and knowledge have proved invaluable. Also, I wish to thank those of my friends who suffered through E369 and have now moved on to greener pastures: George Alverson (who dared to return), Waldo MacKay, Dan Bender, and Eric Smith. I also acknowledge the invaluable help we were given at Fermilab during the running of the experiment to our technicians, especially Eric Erdos, Delmar Miller, and Ken Gray. The systems programmers at the University of Illinois kept the computers that made portions of the data analysis possible running, and were very helpful with any sort of computing problem. I would especially like to thank Dave Lesny and Jerry Wray in this respect. Also, I learned some of the finer nuances of RT-11 at the able hands of Terry Lagerlund and Dave Ritchie on the Fermilab computing staff, and a lot about

phototube characteristics from Cordon Kerns at Fermilab. But most of all, I would like to thank my wife Deedee for sticking with me through thick and thin. She served as an able technician during the course of the experiment and a programming go-fer afterward, in addition to organizing many a fine communal dinner during the experiment. Lastly, I thank my son Chad for giving me something to smile about in the morning.

The work presented in this thesis was supported in part by the U.S. Department of Energy under grant DE-AC02-76ER01195. This thesis is dedicated to my loving parents, Robert Erick and Dorothy Jane Hahn.

TABLE OF CONTENTS

CHAPTER

CHAPTER ONE

INTRODUCTION

The following analysis involves data collected during the test running and actual data logging of Experiment E610 at the Fermi National Accelerator Laboratory during 1979 and 1980. This experiment was joined in by a collaboration of physicists from Fermilab, the University of Illinois, Purdue University, and Tufts University. As with all of the experiments in recent years in the Muon Lab, this one was made possible by the Chicago Cyclotron Magnet (CCM) as the foundation of a large spectrometer; however, this experiment broke with the past in that most of the apparatus was new—for example, all the spark chambers used in previous years were replaced by drift chambers and the photon calorimeter was completely redesigned and enlarged. Particles were produced in the lab by collisions of 225 GeV/c negative pions on a beryllium target.

The event trigger was designed to find opposite charged dimuon pairs with large masses—a signature of the J/ψ meson. The masses and quantum numbers of the J/ψ and its related family are shown in Figure 2-2. A large lead glass shower detector was used to permit reconstruction of the $J/\psi-\gamma$ decays of the χ charmonium states. The large gas Cerenkov counter used in the previous experiment was

lengthened to improve the efficiency of particle identification for reconstruction of dikaon and overt charm states but this will be only briefly mentioned in this thesis. A large data base of such dimuon events was collected (approximately 4 million events on tape), analyzed and filtered for events with J/ψs (about 1200 events), and then further analyzed for χ mesons in the reaction:

$$\pi^- \text{Be} \longrightarrow \chi + X$$
$$\chi \longrightarrow J/\psi + \gamma$$

Although both the ψ and χ mesons have been seen in very clean signals in electron-positron colliding beam experiments, the production of these states in hadronic collisions is of great interest because such production mechanisms provide us with one of the few tests of the form of the theory of strong interactions, quantum chromodynamics. The results and details of this analysis are reported on in the following chapters.

CHAPTER TWO

THEORY

2.1 The Quark-Parton Model

The great success story in the history of particle physics has been the application of a hierarchical model to elementary particles. Just as chemistry is based on the proposition that compounds are made of molecules which in turn are made of atoms, nuclear and particle physics are based on the proposition that atoms are composed of electrons (where the chemistry of the atom actually resides) and nuclei, and nuclei are composed of neutrons and protons. New theoretical tools and new experimental data led to the discoveries and development of first atomic and then nuclear theory. As the "microscopes" of the physics community improved in their resolution, smaller constituents became "visible". Of course, here I am not talking of microscopes in the literal sense, but instead of high-energy particle collisions, first from radioactive sources and cosmic rays and later from the particle accelerators of Lawrence onward. In the past few decades, it has become clear that the remarkable power of Feynman's theory of quantum electrodynamics (QED)—providing us today with some of the most accurately known constants in any science—is due to the point-like nature of the electron. Even at today's accelerator energies, no evidence is found

for any internal structure of the electron; that is, the electron appears to be a basic constituent of matter. One might hope that if all the basic constituents of matter could be identified, a complete theory of matter and energy could be formulated.

However, the behavior of nucleons in high-energy collisions showed an internal structure, usually parameterized by form factors. Concurrently, it was realized that many of the symmetry properties of the bewildering variety of subatomic particles found in the late 1940's and afterward could be classified using group theory applied to the unitary symmetry group SU(3) (Gell-Mann 1964; Ne'eman 1961; Zweig 1964). This was initially viewed by many as only a mathematical classification; but larger accelerators produced evidence in deep inelastic scattering that the hadrons are composed of internal constituents or "partons". It was only natural to indentify the generators of SU(3) with the partons, and in this guise, these constituent particles of hadrons became known as "quarks" (Gell-Mann's designation). Endowing the quarks with quantum numbers such that the proper combinations of quarks produce the known mesons and baryons seemed a much more straightforward method of introducing the proper group theoretic properties than any other method.

Even before the current constituent model of hadrons was developed, the need for a fourth quark—the "charmed" quark—was proposed for symmetry's sake. Bjorken and Glashow suggested its existence so that the number of hadronic constituents is equal to the number of known leptons (Bjorken 1964). Adding a fourth charged hadron current to the Lagrangian of Weinberg and Salam's theory of weak interactions was found to remove an unseen strangeness changing neutral current (Glashow 1976). Unexpectedly, the new higher energies which have made available the charmed particles have also revealed an even higher mass quark, the "bottom" quark (Herb 1977) and a higher mass lepton, the tau lepton (Perl 1975). Furthermore, certain triangle Feynman graph anomalies suggested quantum number relations which also favored another quark (Jackiw 1972) in that they also demanded an equal number of quarks and leptons. The discovery of the J/ψ in 1974 (Augustin 1974; Aubert 1974) not only confirmed the qualitative predictive power of the quark model; it also presented an ideal testing ground for the Lagrangian formulation of the quark model--quantum chromodynamics (QCD). Table 2-1 shows the currently favored six "flavors" of quarks: up, down, strange, charm, bottom, and top. Their associated quantum numbers are shown including those that distinguish the newer flavors: Strangeness, Charm, Beauty (or "Bottomness"), and Truth (or "Topness"). The top quark has not been identified in any reaction, but is theoretically necessary in

Flavor	I	I_z	S	C	B	T	Q/e
u	1/2	1/2	0	0	0	0	2/3
d	1/2	-1/2	0	0	0	0	-1/3
c	0	0	0	1	0	0	2/3
s	0	0	-1	0	0	0	-1/3
t	0	0	0	0	0	1	2/3
b	0	0	0	0	-1	0	-1/3

Table 2-1

Quark Quantum Numbers

I - total isospin

I_z - z-component of isospin

S - strangeness quantum number

C - charm quantum number

B - bottom quantum number

T - top quantum number

Q/e - electric charge

association with the bottom quark as the charmed quark was in association with the strange quark. Thus, in the last decade, the group describing the quark flavors has expanded from SU(3) to SU(4) to SU(6), although in this discussion only SU(4) will be necessary.

QCD attempts to describe the strong interaction in terms of exchange currents as QED has so successfully described the electromagnetic interaction. Corresponding to the massless vector boson--the photon--and the massive point-like charged fermions--the leptons--of QED are the gluon and quarks of QCD. Study of the ratio

$$R = (e^+e^- \longrightarrow \text{hadrons})/(e^+e^- \longrightarrow \mu^+\mu^-)$$

in colliding beam machines led to the conclusion that each of the quarks came in three "colors" (e.g., Novikov 1977). The total wavefunction of the physical particles is then described by $SU(4) \times SU(2) \times O(3) \times SU(3)_c$: SU(4) for the quark flavors, SU(2) for the fermion spins of the quarks, O(3) for the orbital angular momentum of the quarks, and $SU(3)_c$ for the "color charge" of the quarks. This addition also resolves several other problems with the quark model (Close 1981). With the color group included it becomes possible to construct an antisymmetric wavefunction for baryons with three identical quarks in the ground state. Also, with color included, a theorem relating the rate of the π^0 Dalitz decay to the

total number of quarks and their charges agrees with experiment. The inclusion of color suggested to the theorists that QCD was a non-Abelian gauge theory where, unlike QED, the intermediate boson also carried the "charge" of the interaction, known as "color" or "color charge". This not only modified the form of the vertex factors and propagators for the Feynman diagrams of QCD but actually increased the possible interaction vertices of QCD (Figure 2-1b) from the single vertex of QED (Figure 2-1a).

The facts that neither isolated quarks (with their obvious fractional charge signature) nor "color" have been observed imply in turn that 1)the quark-quark potential is so strong that we cannot sever quarks in hadrons at current (and perhaps any) energies, and 2)that real hadrons are "colorless" which further constrains the possible interactions.

2.2 The Charmonium Spectrum

Various theories of quark confinement suggest that deep within the potential well, the quarks behave as if they were free (Nambu 1974; Jaffe 1977). In addition, the heavier quarks (the c and b quarks) can be treated non-relativistically. Thus the quarkonium states $c\bar{c}$ and $b\bar{b}$ have the most calculable spectra. Using the experimental data to establish empirical fits, numerical calculations

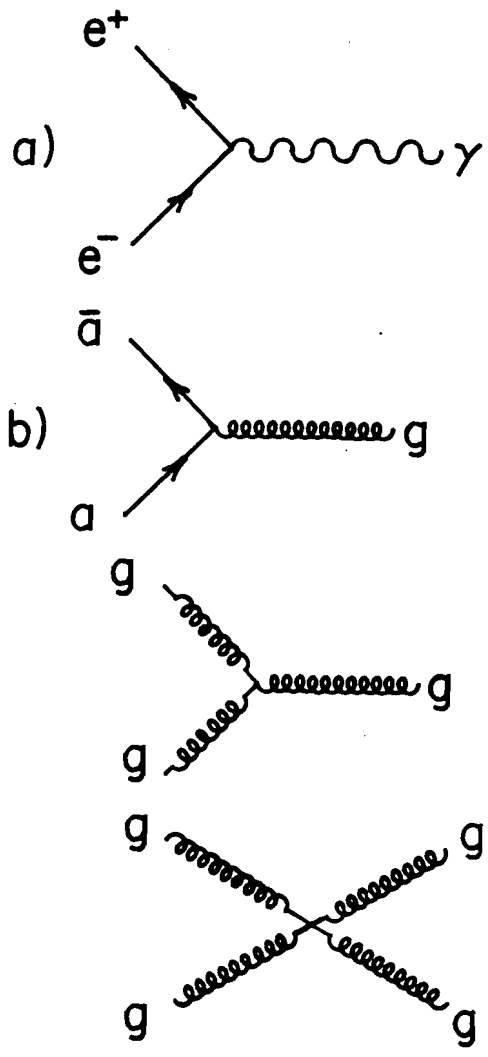

Figure 2-1

a) allowed vertex in QED

b) allowed vertices in QCD

have been performed employing potentials without unbound solutions (Barbieri 1976; Carlson 1976). These potentials usually consist of a Coulombic term and a term such that quarks are confined. The observed charmonium spectrum (Figure 2-2) agrees well with the predictions of these potential models which use only the charmed quark mass, the strong coupling constant, and the functional form of the potential as input parameters. Those states which couple to the photon (the $J^{PC}=1^{--}$ states) are produced copiously in colliding electron-positron beam machines and their electromagnetic decays have been extensively studied. These states' decay products include the rest of the charmonium spectrum, and the burden of the data is again provided by e+e- experiments. Many hadronic decay channels are also known to exist (Table 2-2).

The narrow widths of the $J/\psi(3100)$ and the $\psi(3685)$ for strong decays are consistent with the phenomenological Okubu-Zweig-Iizuka (OZI) rule (Iizuka 1977) which states that "disconnected" quark diagrams are suppressed relative to "connected" quark diagrams (Figure 2-3). Charmonium states which are massive enough preferentially decay to pairs of charmed mesons $\bar{c}q$ and $c\bar{q}$, where q is a light quark (the u, d, or s quarks), as shown in Figure 2-3a. This limit, at twice the D meson mass--3730 MeV, is known as the charm threshold.

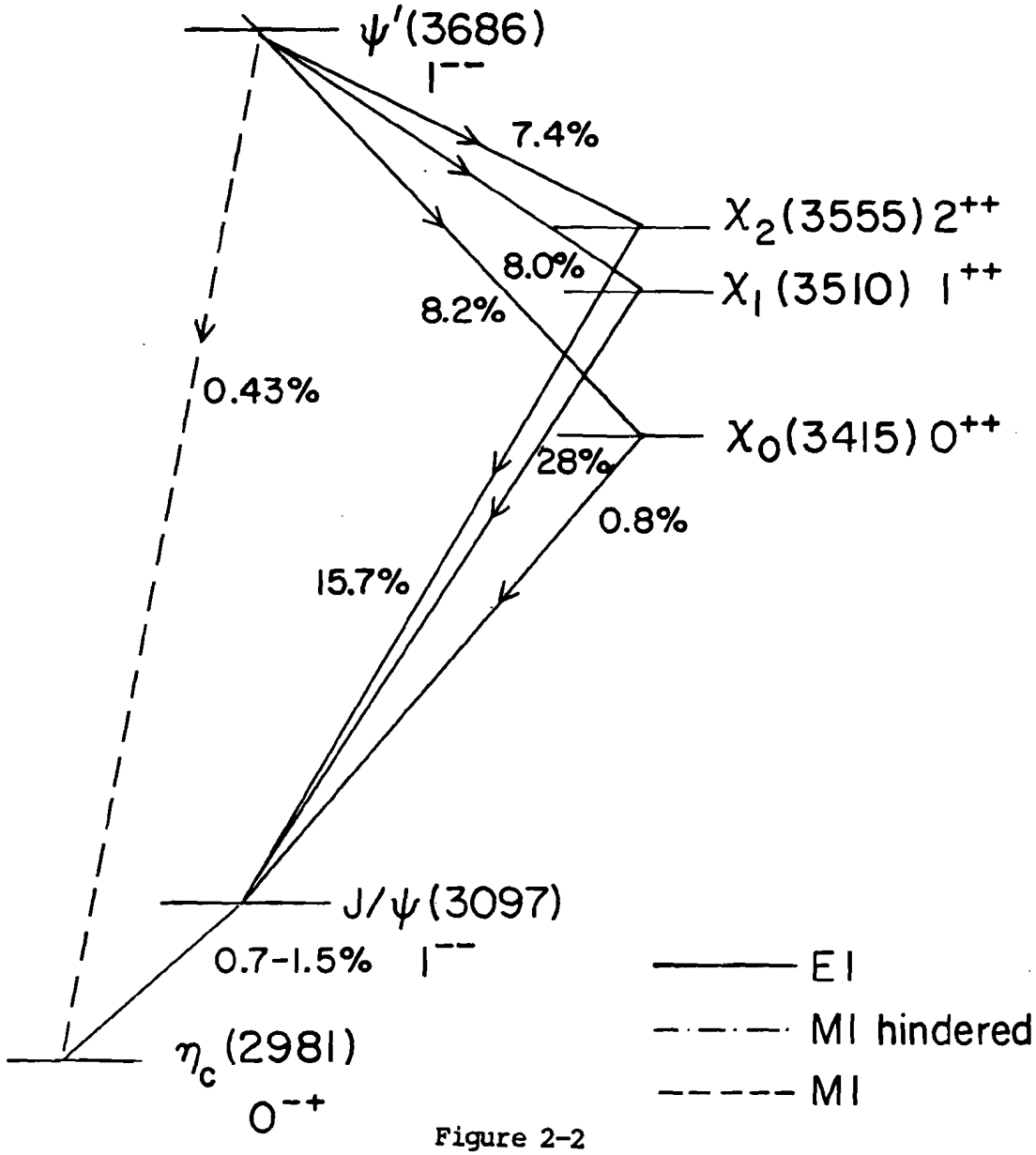

Figure 2-2

The Charmonium Spectrum with Radiative Decays

	$I^G J^{PC}$ or J^{PC}	Mass M (MeV)	Full Width Γ (MeV)	M^2 $\pm\Gamma M^a$ (GeV^2)	Partial decay mode: Mode	Fraction %; [Upper limits (%) are 90% CL]	p or p_{max} [b] (MeV/c)
$\eta_c(2980)$	$0^+(\ )^+$	*2981* ±6	*< 20*	8.89	$\gamma\pi^+\pi^-$	*seen*	1426
					$2(\pi^+\pi^-)$	*seen*	1458
					$K^+K^-\pi^+\pi^-$	*seen*	1343
					$p\bar{p}$	*seen*	1158
$J/\psi(3100)$	$0^-(1^-)-$	3096.9 ±0.1	0.063 ±0.009	9.591 ±0.000	e^+e^-	7.4 ±1.2	1548
					$\mu^+\mu^-$	7.4 ±1.2	1545
					hadrons + radiative	85 ±2	
					Radiative decay modes		
					†$\gamma\eta(1440)$	*0.55 ±0.22*[n]	1224
					$\gamma\eta'$	*0.36 ±0.05*	1408
					γf	0.15 ±0.04	1287
					$\gamma\eta$	*0.086 ±0.009*	1500
					$\gamma\pi^0$	*0.007 ±0.005*	1546
					$\gamma D(1285)$	*< 0.6*	1283
					2γ	*< 0.05*	1548
					$\gamma f'(1515)$	*< 0.03*	1175
					$\gamma p\bar{p}$	*< 0.01*	1232
					3γ	*< 0.006*]	1548
$\chi(3415)$	$0^+(0^+)+$	3415.0 ±1.0		11.662	$2(\pi^+\pi^-)$ (incl. $\pi\pi\rho$)	4.3 ±0.9	1679
					$\pi^+\pi^-K^+K^-$ (incl. $\pi K\bar{K}^*$)	3.4 ±0.9	1580
					$3(\pi^+\pi^-)$	1.7 ±0.6	1633
					$\pi^+\pi^-$	0.9 ±0.2	1702
					$\gamma J/\psi(3100)$	*0.8 ±0.2*	303
					K^+K^-	0.8 ±0.2	1635
					$p\bar{p}\pi^+\pi^-$	0.6 ±0.2	1320
					For upper limits, see footnote *o*		
p_c or $\chi(3510)$	$0^+(1^+)+$	3510.0 ±0.6		12.320	$\gamma J/\psi(3100)$	28 ±3	389
					$3(\pi^+\pi^-)$	2.4 ±0.9	1683
					$2(\pi^+\pi^-)$ (incl. $\pi\pi\rho$)	1.8 ±0.5	1727
					$\pi^+\pi^-K^+K^-$ (incl. $\pi K\bar{K}^*$)	1.0 ±0.4	1632
					$\pi^+\pi^-p\bar{p}$	0.15 ±0.10	1381
					For upper limits, see footnote *p*		
$\chi(3555)$	$0^+(2^+)+$	3555.8 ±0.6		12.644	$\gamma J/\psi(3100)$	15.7 ±1.7	429
					$2(\pi^+\pi^-)$ (incl. $\pi\pi\rho$)	2.3 ±0.5	1750
					$\pi^+\pi^-K^+K^-$ (incl. $\pi K\bar{K}^*$)	2.0 ±0.5	1656
					$3(\pi^+\pi^-)$	1.2 ±0.8	1706
					$\pi^+\pi^-p\bar{p}$	0.35 ±0.14	1410
					$\pi^+\pi^-$	*0.20 ±0.11*	1772
					K^+K^-	*0.16 ±0.12*	1708
					For upper limits, see footnote *q*		
$\psi(3685)$	$0^-(1^-)-$	3686.0 ±0.1	0.215 ±0.040	13.587 ±0.001	e^+e^-	0.9 ±0.1	1843
					$\mu^+\mu^-$	0.8 ±0.2	1840
					hadrons + radiative	98.1 ±0.3	
		$m_{\psi(3685)} - m_{J/\psi(3100)} = 589.06 \pm 0.13$					
		Radiative decay modes					
	†$\gamma\chi(3415)$	8.2 ±1.4		261			
	$\gamma\chi(3510)$	8.0 ±1.3		172			
	$\gamma\chi(3555)$	7.4 ±1.3		128			
	$\gamma\eta_c(2980)$	*0.43 ±0.26*		638			
	$\gamma\eta_c(3590)$	*0.2 to 1.3*		91			
	$\gamma\pi^0$	*< 0.5* (CL=95%)		1841			
	$\gamma\eta$	*< 0.02*		1802			
	$\gamma\eta'$	*< 0.02*		1719			
	$\gamma\iota(1440)$	*< 0.018*[n]]		1570			

Table 2-2

Parameters of the charmonium spectrum

(from Phys. Lett. 111B (1982))

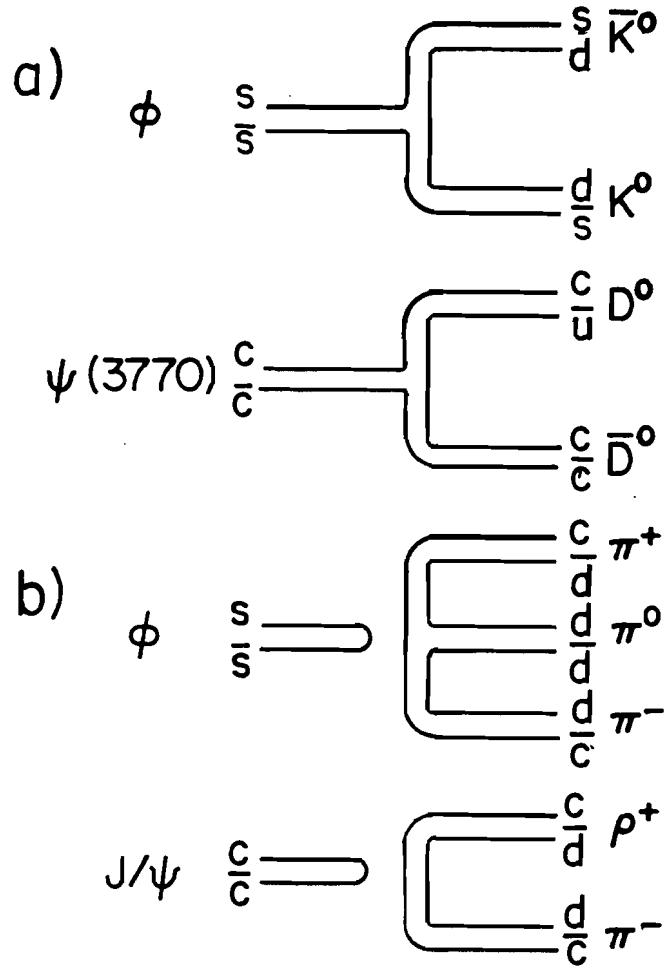

Figure 2-3

a) connected duality diagrams

b) disconnected duality diagrams

2.3 Production Mechanisms of Charmonium

Three or four years ago, it appeared progress was being made toward a theory of charmonium production in hadronic interactions. Electromagnetic production of charmonium is understood in analogy to the Drell-Yan mechanism for production of dilepton pairs (Escobar 1981). This provides us with a probe of the vertex form factor of the QCD vertex of photon-quark-anti-quark which is analogous to the photon-electron-positron vertex of QED. Hadronic production of charmonium is understood in terms of the gluon-quark-anti-quark vertex ("quark fusion") and the gluon-gluon-gluon vertex ("gluon fusion") as shown in Figure 2-1b. However, conservation laws restrict the possible final states. A single gluon cannot couple into a physical particle which is colorless, or, to use group theoretical language, the gluon, being a color octet state, cannot couple directly to a physical color singlet state. One solution to this problem is the emission of a soft gluon from the charmonium state before it actually becomes "physical". However, such a solution does not have a clear theoretical interpretation. If, on the other hand, we demand no soft gluon emission, two or three gluon lines between the fusion mechanism and the charmonium particle are necessary. In analogy to the photon, the gluons have negative charge conjugation, but because color charge SU(3) enters the picture, three gluons can form a positive or negative charge conjugation state whereas three photons can only form a negative charge conjugation state. Two gluons can only form a

positive charge conjugation state as with photons. Thus, either ψ (C = -) or χ (C = +) states can be produced hadronically via these fusion mechanisms, but the ψ states with their negative charge conjugation will be suppressed by at least one extra vertex factor as shown in Figure 2-4.

In recent years, theoretical calculations taking into account higher order effects to these fusion mechanism models have been undertaken. The results seem to indicate that neither soft gluon emission nor higher order diagrams can be dismissed in the perturbation theory (Escobar 1981; Buras 1981).

The relative widths of the three charmonium P-states (χ_0, χ_1, and χ_2) can be calculated with QCD diagrams if one is willing to discard whatever effects the "hadronization" from the bare quarks to the physical state might have since these are currently not calculable. Originally, only the widths from gluon fusion (without the complications of soft gluon emission) were calculated (Carlson 1976); these calculations gave:

$$\Gamma(\chi_0) = \frac{2}{3} \frac{9 \alpha_s^2}{m_c^4} \left| \frac{d\Phi(0)}{dr} \right|^2$$

$$\Gamma(\chi_1) = 0$$

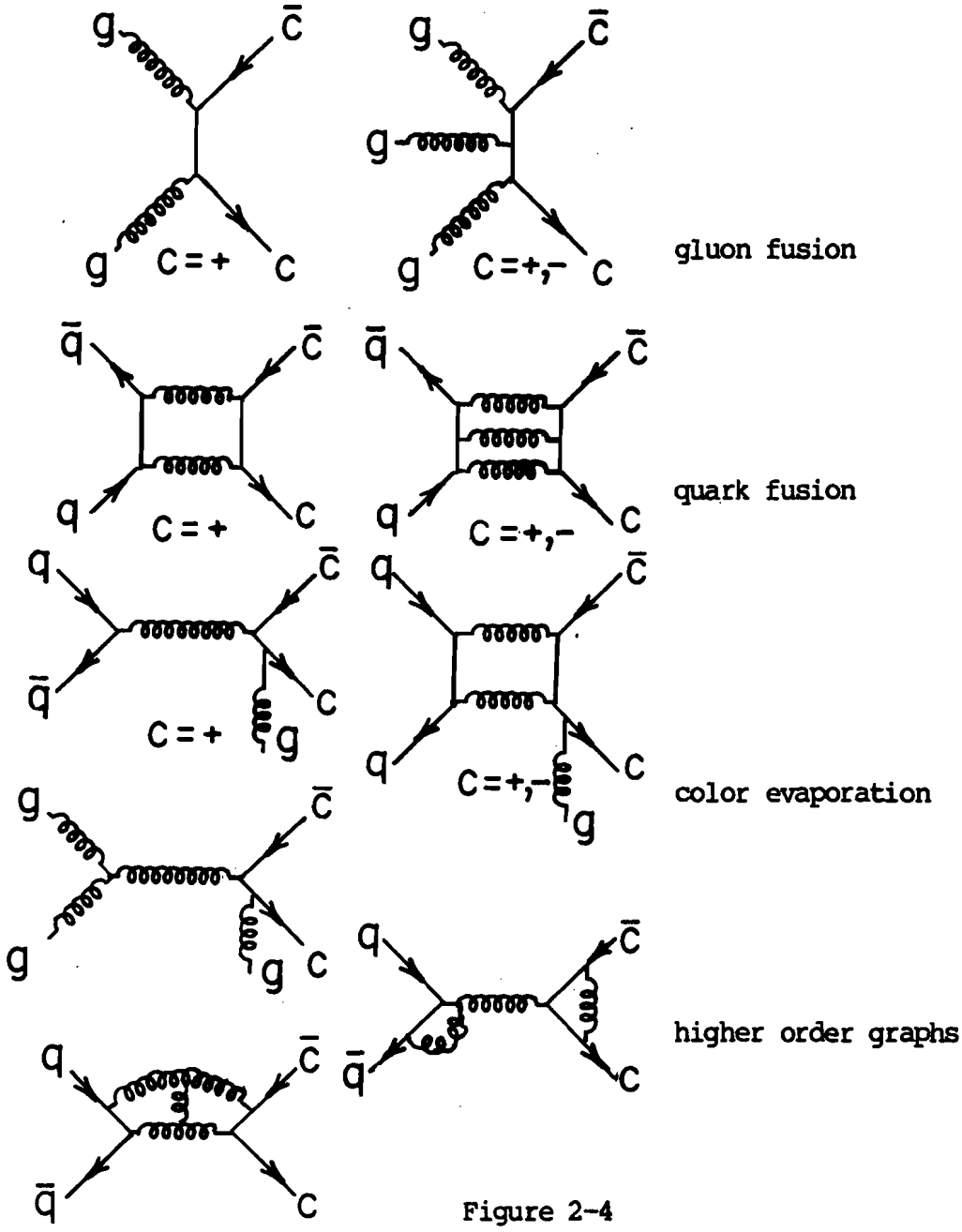

Figure 2-4

Possible hadroproduction mechanisms of charmonium

$$\Gamma(\chi_2) = \frac{2}{3}\frac{12\alpha_s^2}{5m_c^4}\left|\frac{d\Phi(0)}{dr}\right|^2$$

with $\hbar = c = 1$, m_c the mass of the charmed quark, and α_s the strong coupling constant. Here the wavefunctions derived from the potential models mentioned earlier are used as input to the radial derivatives. The J=1 P-state cannot couple to two massless J=1 gluons; this statement is sometimes known as the Yang-Landau theorem (Yang, 1950). The vector state can only be constructed out of three available vectors: the two polarization vectors of the gluons, and their relative momentum vector. The only possible construct which is even under exchange of the two gluons is:

$$\vec{k} \times (\vec{e}_1 \times \vec{e}_2)$$

but when this expression is expanded and the transversality condition $\vec{e} \cdot \vec{p} = 0$ for massless particles is imposed, this expression also vanishes.

With the same restrictions, the QCD diagrams for quark fusion can also be calculated with the results (Carlson 1976):

$$\Gamma(\chi_0) = 0$$

$$\Gamma(\chi_1) = \frac{1}{3}\frac{1}{4\pi}\left|-\frac{\alpha_s}{M_\chi}\ln\left(\frac{4m_c - 2M_\chi}{M_\chi}\right)\right|^2 M_\chi \left|\frac{d\Phi(0)}{dr}\right|^2$$

$$\Gamma(\chi_2) = \frac{1}{5}\,\frac{1}{16\pi}\left|\frac{\alpha_s\sqrt{2}}{M_\chi}\ln\left(\frac{4m_c - M_\chi}{M_\chi}\right) + \frac{1}{3}\left(i\pi + \ln 2 - 1\right)\right|^2 M_\chi \left|\frac{d\Phi(0)}{dr}\right|^2$$

Here, M_χ is the physical mass of the χ meson in question. These results are all due to calculations of sums of QCD graphs. A modification to the gluon fusion model which allows production of the J=1 P-state consists of allowing one of the gluons to be virtual and therefore massive. In this case, the gluon fusion decay width becomes (Altarelli 1982):

$$\Gamma(\chi_1) = \frac{8}{3}\,\frac{4\alpha_s^2}{3m_c^4}\left|\frac{d\Phi(0)}{dr}\right|^2 \ln\left(\frac{4m_c^2}{4m_c^2 - M_\chi^2}\right)$$

If we allow soft gluon emission (also known as the "color evaporation" theory), then the situation is immediately greatly simplified. Since in this case, both quark fusion and gluon fusion are mediated through a single gluon, the decay widths for the three P-states are identical and the cross sections are just proportional to the ratios of the spin factors (2J + 1).

The ratios of the production rates for the three P-states in the various models are then given by:

$\sigma(\chi_0) : \sigma(\chi_1) : \sigma(\chi_2) = 8 : 3 : 10$ gluon fusion

$\sigma(\chi_0) : \sigma(\chi_1) : \sigma(\chi_2) = 0 : 18 : 5$ quark fusion

$\sigma(\chi_0) : \sigma(\chi_1) : \sigma(\chi_2) = 1 : 3 : 5$ color evaporation

The actual ratio of number of χs seen is then given by the ratio of the cross sections times the branching ratios of each state's radiative decay into J/ψ and a photon. These branching ratios are well known from electron-positron colliding beam experiments (Particle Data Group, 1982). The expected ratios are given below. These ratios must then be modified by the experimental acceptances.

$B\sigma(\chi_0) : B\sigma(\chi_1) : B\sigma(\chi_2) = 1 : 13 : 25$ gluon fusion

$B\sigma(\chi_0) : B\sigma(\chi_1) : B\sigma(\chi_2) = 0 : 13 : 2$ quark fusion

$B\sigma(\chi_0) : B\sigma(\chi_1) : B\sigma(\chi_2) = 1 : 105 : 98$ color evaporation

Even if the ratios of the charmonium P-states cannot be measured, a qualitative probe of the hadronic mechanism is available if the total number of χs can be measured. After correcting the number of χs and number of J/ψs for the experimental acceptances, the fraction of J/ψs resulting from the radiative decays of the χs can be

calculated. I shall call this qauntity $F_{\psi\chi}$. The only other indirect sources of J/ψs currently known are the hadronic decays of the $\psi(3685)$ to J/ψ. After correction to the number of J/ψs and $\psi(3685)$s by acceptances and branching ratios to dimuons, the fraction of J/ψs resulting from the hadronic decays of the $\psi(3685)$ can be calculated. I shall call this quantity $F_{\psi\psi'}$. Then, assuming there are no other indirect sources of the J/ψ, the fraction of J/ψs which are produced directly is just

$$F(\text{direct}) = 1 - F_{\psi\chi} - F_{\psi\psi'}$$

This fraction is interesting on a qualitative level for its relevance in resolving whether gluon fusion or some other process is the predominant mechanism for hadronic production of charmonium. In perturbative QCD a process is suppressed by a factor of α_s for every gluon-quark-anti-quark vertex in the Feynman diagram (Figure 2-4). Thus, the lowest order diagram is that for gluon fusion with only two gluons. The resulting state must have charge conjugation plus, and so must be a χ. Thus, to the degree QCD is a perfect perturbative theory, we would expect gluon fusion to be the major process and direct production of the J/ψ to be suppressed. This implies F(direct) approaches zero. Conversely, if F(direct) is substantial, other hadronic mechanisms must be present—for example, those diagrams

shown in Figure 2-4 which allow negative charge conjugation states.

2.4 The Charm Suppression Factor

The additive quark model of Schekter and Shcheglova is described in detail in the thesis of P. Schoessow (Schekter, 1964; Schoessow, 1983). The essential points of the model are the following: for particles produced in the central region of a collision, the colliding particles can be considered a plasma of partons, the majority of which are up or down quarks; the possibility that one of the quarks present in this plasma is a strange quark is suppressed by a factor λ known as the strangeness suppression factor; the production of produced hadrons is then given by a factor of λ for each strange quark in the hadron and a factor of (2J+1) for the possible states of a spin J particle. By taking ratios of different hadrons produced in the same collisions, the factor λ can be calculated. The strangeness suppression factor has been calculated for many reactions with different colliding particles and center of mass energies (Malhotra, 1983). In every case, the result has been remarkably similar; the world average currently is $\langle\lambda\rangle = 0.29 + 0.02$ (Figure 2-5).

A simple elaboration of the model is the inclusion of an additional factor α, the ratio of higher-lying multiplet production to the lowest-lying multiplet production. In the case of the

multiplets L=0 and L=1, a universal value is found to be valid in different reactions and at different center of mass energies. This value is $\langle \alpha \rangle = 0.13 \pm 0.03$.

Likewise, a charm suppression factor λ_c could be defined. This would simply be the probability of producing a charmed quark in a collision instead of the usual up or down quark. Several theoretical models make simple predictions for the values of the strangeness and charm suppression factors (Peterson 1979). A string confinement model predicts that the probability of creating a $Q\bar{Q}$ pair of heavy quarks (proportional to λ_c^2) should have a form:

$$P(q\bar{q} \rightarrow q\bar{q}Q\bar{Q}) \simeq \exp(-\pi m_\perp^2/\kappa)$$

where κ is a constant of the string confinement theory, $\kappa = 0.2$ GeV, and $m_\perp$ is the transverse mass of the quark Q. If we take approximate values of m(u) = m(d) = 0 MeV, m(s) = 100 MeV, m(c) = 1.5 GeV, and $\langle p_\perp \rangle$ = 350 MeV, then we can calculate:

$$u\bar{u} : d\bar{d} : s\bar{s} : c\bar{c} = 1 : 1 : 0.33 : 10^{-10}$$

$$\lambda = 0.57$$

$$\lambda_c = 10^{-5}$$

A second model is a simple thermodynamic or statistical model which

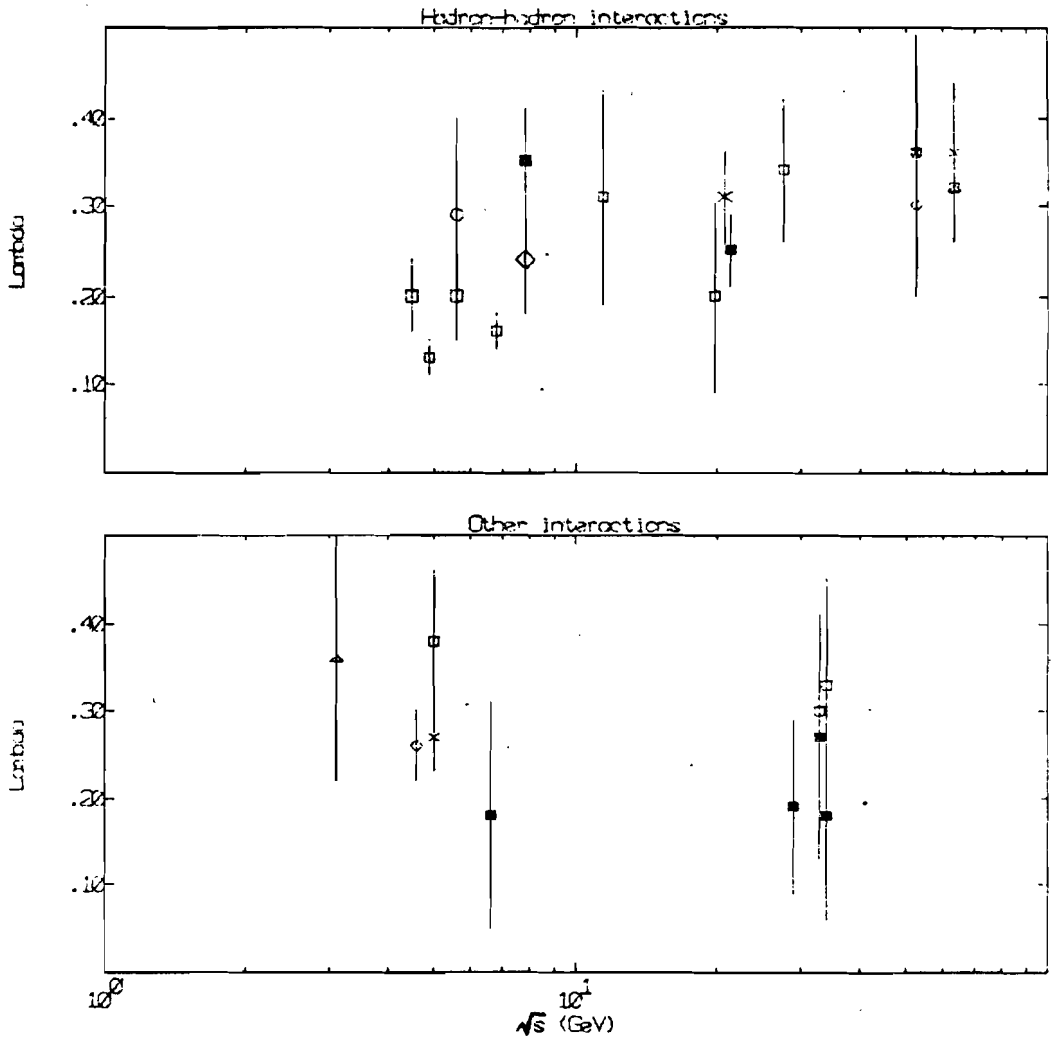

Figure 2-5

World data on the strangeness suppression factor

predicts the probability of producing a meson with a single heavy quark to be of the form:

$$P(hh \rightarrow q\bar{Q}) \simeq \exp(-2m/m_0)$$

here m_0 is a mass set by the ratio of kaons to pions, for example, to give:

$$\pi : K : D = 1 : 0.13 : 3 \times 10^{-5}$$

which in turn should be just the values for the suppression factors since these mesons contain only one heavy quark. The actual value for the strangeness suppression factor falls about halfway in between the two predicted values; the charm suppression factor has not been previously calculated.

Chapter Three

Apparatus

The experiment took place in the Muon Lab during the summer of 1980; actual data logging took place from April 5, 1980 to June 23, 1980. The spectrometer used was quite different from previous configurations which used the Chicago Cyclotron Magnet (CCM) for momentum identification; it will be described in detail in this chapter. The lead glass shower detector with which this analysis is especially concerned will be described at length.

The Chicago Cyclotron Magnet itself and some of the older pieces of apparatus are described in earlier theses from Fermilab Experiments 98, 398, and 369 (Pordes, 1976; Hicks, 1978; Proudfoot, 1978; Alverson, 1979; Bender, 1980; Mackay, 1980) and in concurrent theses from Experiment 610 (Hossain, 1980; Budd, 1983; Schoessow, 1983). Where it is appropriate, references will be made to these theses.

The coordinate system used in the following discussion is the standard Muon Lab coordinate system: the center of the CCM is the origin, the Z axis is the beam line with positive Z in the direction of a beam particle, the Y axis is the vertical direction with positive Y pointing up, and the X axis is then defined such that the coordinate system is right-handed — i.e., since the positive Z direction is "Lab

North" (not actually north) then the positive X direction is "Lab West" (see Figure 3-1 for a plan view of the laboratory and Figure 3-2 for a side view). Positively charged particles were deflected in the positive X direction by the CCM during normal running. The CCM was operated at 14.047 kilogauss over an effective volume of 19 m^3, which imparted a transverse momentum impulse of 2.115 GeV/c to charged particles passing through the magnet along the beam axis.

The apparatus will be described more or less from "upstream" of the CCM where the beam enters the lab to "downstream" of the CCM where particles exit through the last hodoscope, followed by an explanation of the on-line computers and electronics which made data logging possible.

3.1 Beam Line Equipment

The beam line as arranged during our experiment could either be used as a 225 GeV/c negative pion beam for data logging (Figure 3-3) or as an electron beam for calibrating the lead glass shower detector. Electrons were produced as the decay product of secondary target collisions in a polyethylene target inserted upstream of the experiment. In the latter mode, beam tunes were devised to obtain nominal momenta of 7.5, 15, and 25 GeV/c (Figure 3-4). The equipment in the N0 beam line made these two beams possible (Figure 3-5). In

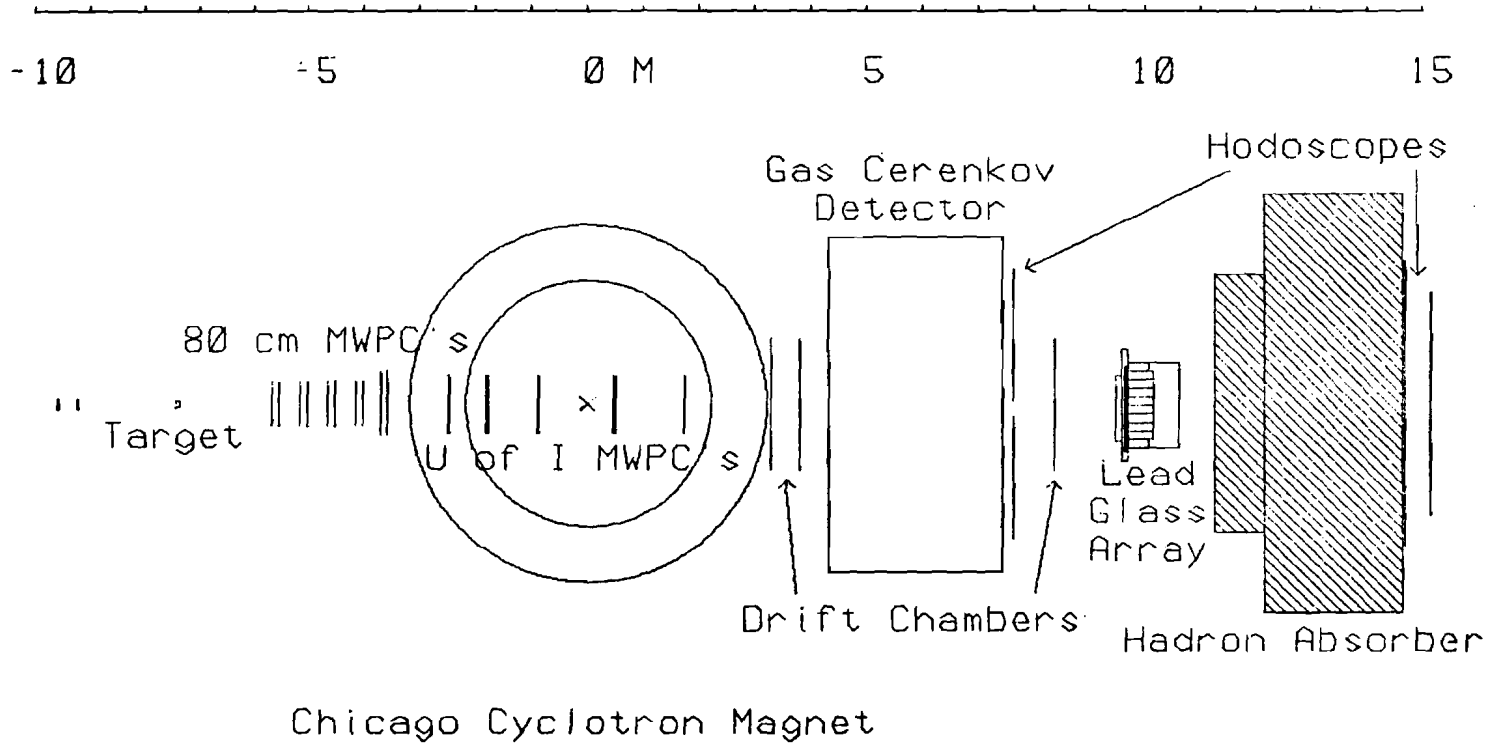

Figure 3-1

Plan view of E610

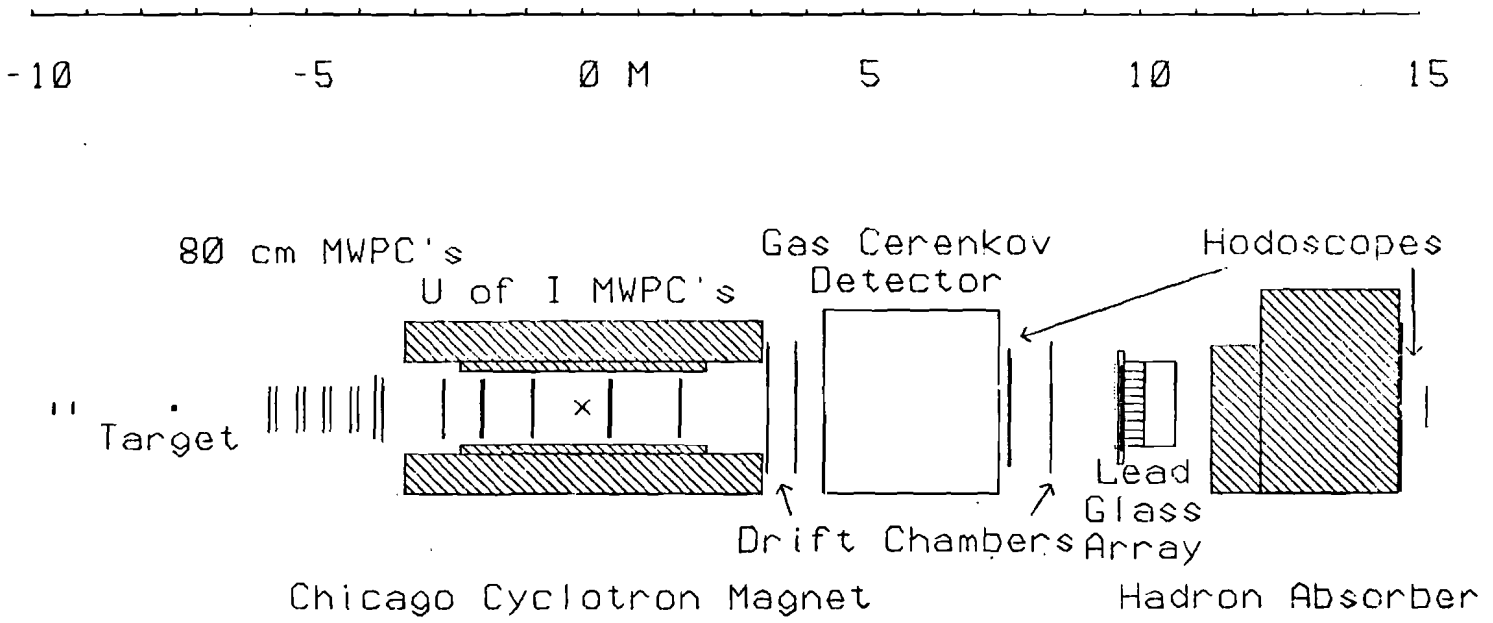

Figure 3-2

Side view of E610

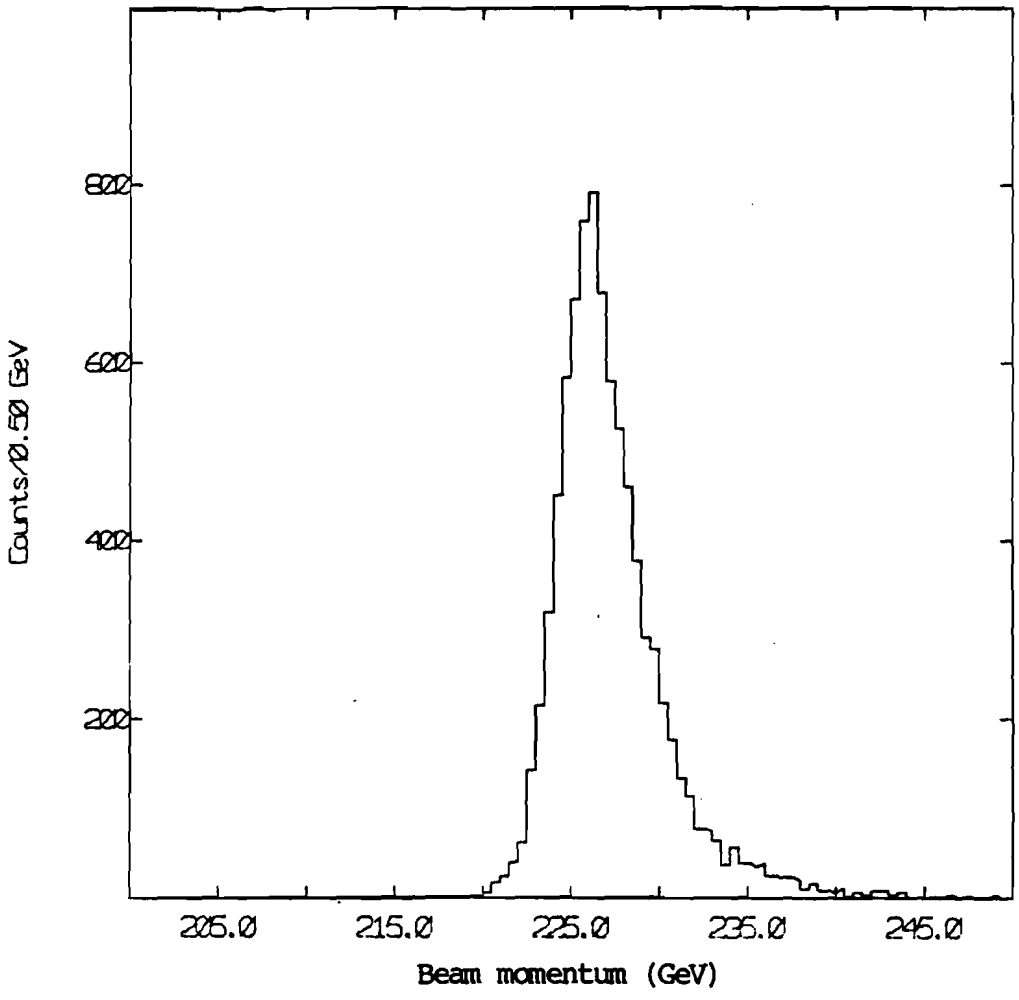

Figure 3-3

Pion beam momentum

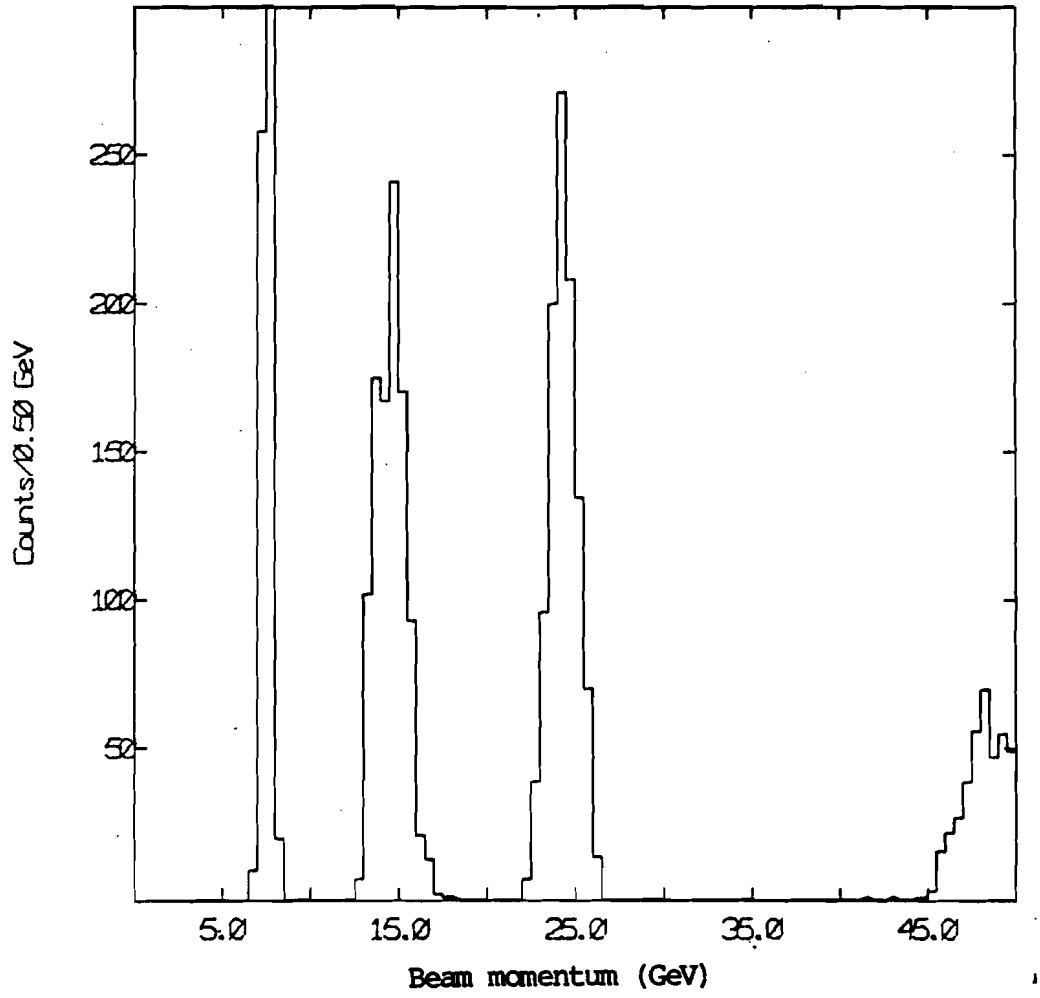

Figure 3-4

Electron beam momentum

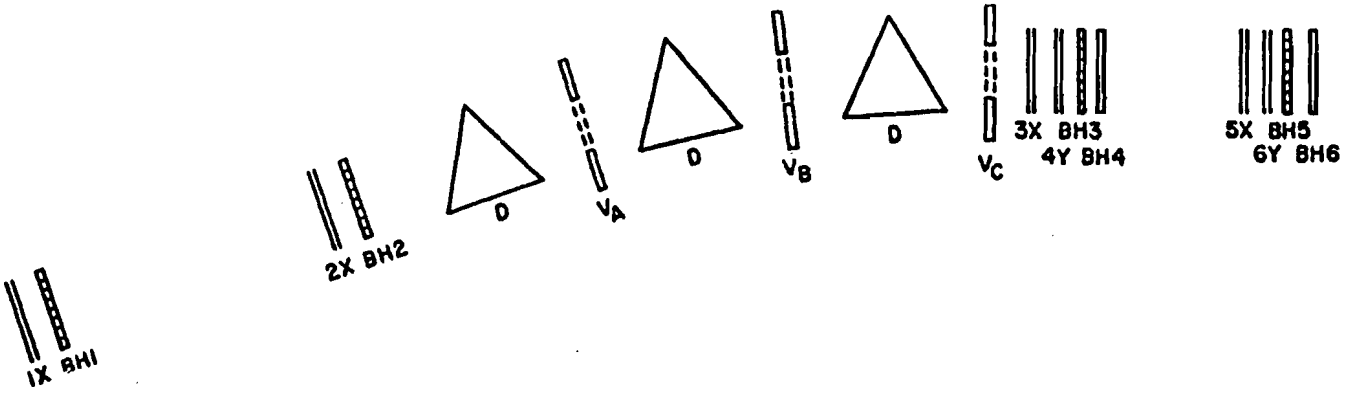

1X, 2X, etc.	6" x 6" MWPC (2 planes each)	
BH1, etc.	Hodoscopes (See Fig 2)	
V_A, V_B, V_C	Veto counters	
D	Magnetic Dipoles	4" x 4" Aperture, each 20 ft. long Total bend is 28.6 mr

Figure 3-5

The N0 beam line

addition, scintillators and MWPC's upstream of and in the Muon Lab—the beam hodoscopes and beam chambers—determined the momentum and position of individual beam particles. Where the beam entered the front (south end) of the Muon Lab, there was also located a removable rotatable dipole magnet to steer the electron beam into the desired lead glass block in the shower detector for calibration purposes; this magnet was not in the beam during normal data logging. At the upstream end of the experiment where the beam entered the laboratory was located a veto hodoscope--the "veto wall"—which vetoed events with halo muons (Figure 3-6). These are muons created upstream of the experiment in the beam line which enter the Muon Lab parallel to the beam; such muons could result in false triggers in our dimuon trigger. The beam line apparatus is described in more detail in the thesis of Howard Budd (1983).

3.2 Target and Trigger Apparatus

The target itself consisted of six 1/2" x 6" x 6" beryllium plates taped together to present 3" of beryllium to the beam. The target and its associated counters all sat on a target table. There were three scintillator counters--one before and two after the target, looking at the target from upstream--labelled T0, and T1 and T2, respectively. This is shown in Figure 3-7 where the beam enters from the left. The thresholds were set on these counters such that T0 had

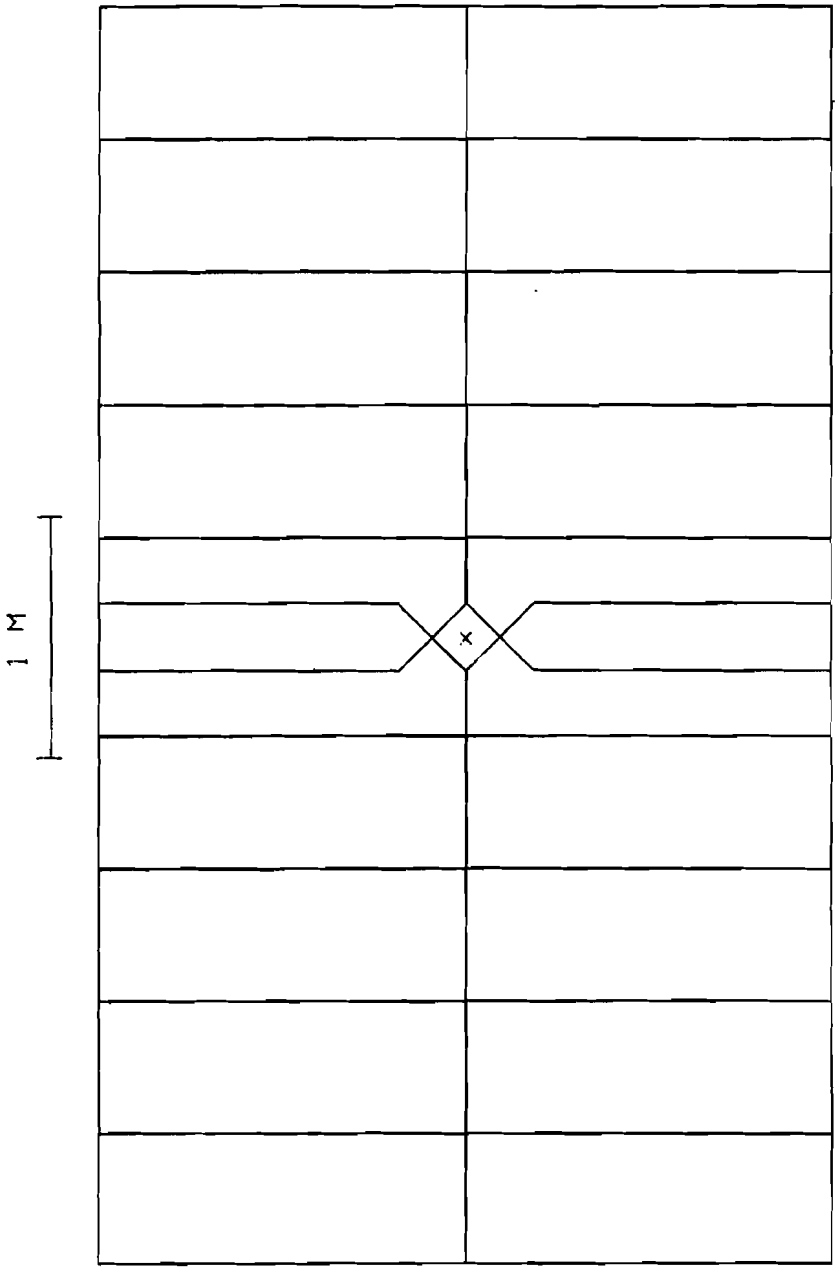

Figure 3-6

The veto wall

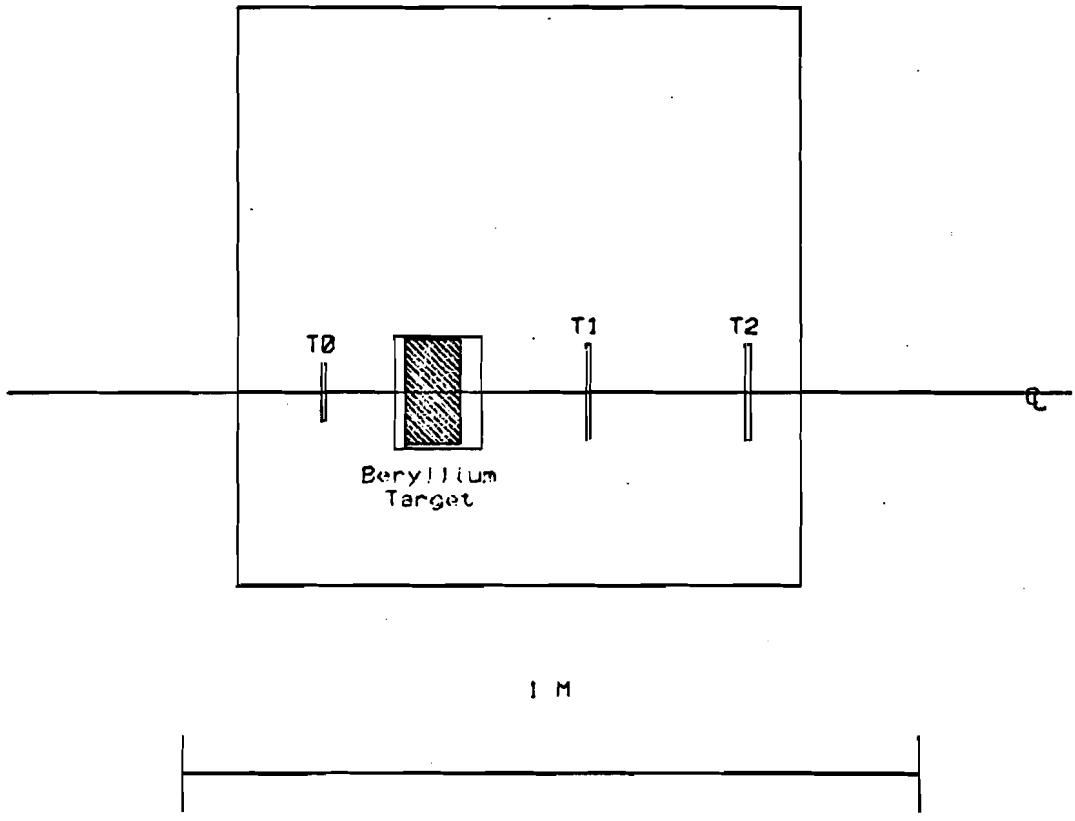

Figure 3-7

The target table assembly

to have less than a certain pulse height while T1 and T2 had to have more than a minimum pulse height; that is, the discriminator levels were chosen so that on the average only a single charged particle went through T0 before the target but two or more charged particles went through T1 and T2 after the target. Ignoring the effects of the Landau distribution's tails, this guaranteed at least one interaction in the target. When the above conditions were met, an "upstream trigger" was formed in the logic which was used to reset the upstream MWPC's and was also used as one of the requirements for a data trigger as described in Appendix C.

3.3 Track Identification Apparatus

Interaction tracks were recorded by nine MWPC's consisting of fifteen planes of sense wires upstream of and in the CCM, and four two-dimensional drift chambers downstream (of which only the three most upstream worked). Upstream of the CCM resided the four 80 cm MWPC's. Each chamber contained an x- and a y-plane consisting of 512 active sense wires spaced 1/16" apart for a total active area of approximately 80 cm x 80 cm (Figure 3-8). Here, the convention is that an x-plane measures x-position and thus has wires strung perpendicular to the x-direction. U- and v-planes refer to tilted planes that measure directions other than x and y. The first four 80 cm chambers were not tilted so that the x-measuring plane actually did

measure x. The fifth chamber, which was closest to the CCM, was tilted at an angle of 45° to help resolve ambiguities in upstream tracks.

The five University of Illinois 1 m MWPC's rested on an aluminum platform which in turn sat on the pole face of the CCM. Each chamber contained a u- , a v-, and a y-plane (the u- and v- planes were rotated about the z-axis 11.310° clockwise and counterclockwise of x as seen viewing the chambers from upstream). Each plane consisted of 480 active wires spaced 0.2 cm apart for the y-plane and 528 active wires for the u- and the v-planes spaced such that their projected wire-spacing onto the x-axis is also 0.2 cm (Figure 3-9). The 80 cm and University of Illinois chambers are described in more detail in the thesis of Howard Budd (1983).

The three active drift chambers consisted of 60 vertical "cells" each 4 cm across for a total fiducial area of 1.2 m x 2.4 m. Each cell consisted of a two-sided vertical delay line on either side of which 0.27 cm away was strung a vertical anode wire (Figure 3-10). Each cell was bordered by vertical cathode and field-shaping wires to ensure uniformity of the electric field. Using the drift time required for the ionization of the track to reach the anode wire and the drift velocity of the drift chamber gas, the x position could be determined to an rms accuracy of 0.066 cm. Using the x position

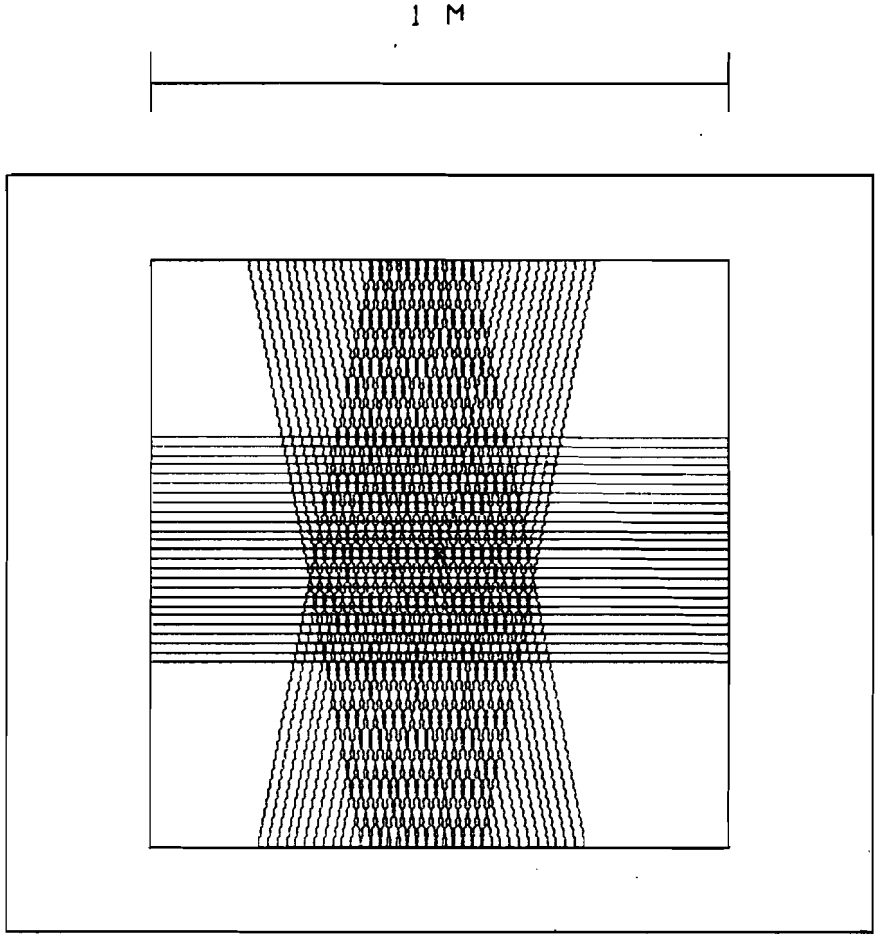

Figure 3-9

University of Illinois chamber construction

(only a portion of wires are shown; wire spacing is not to scale)

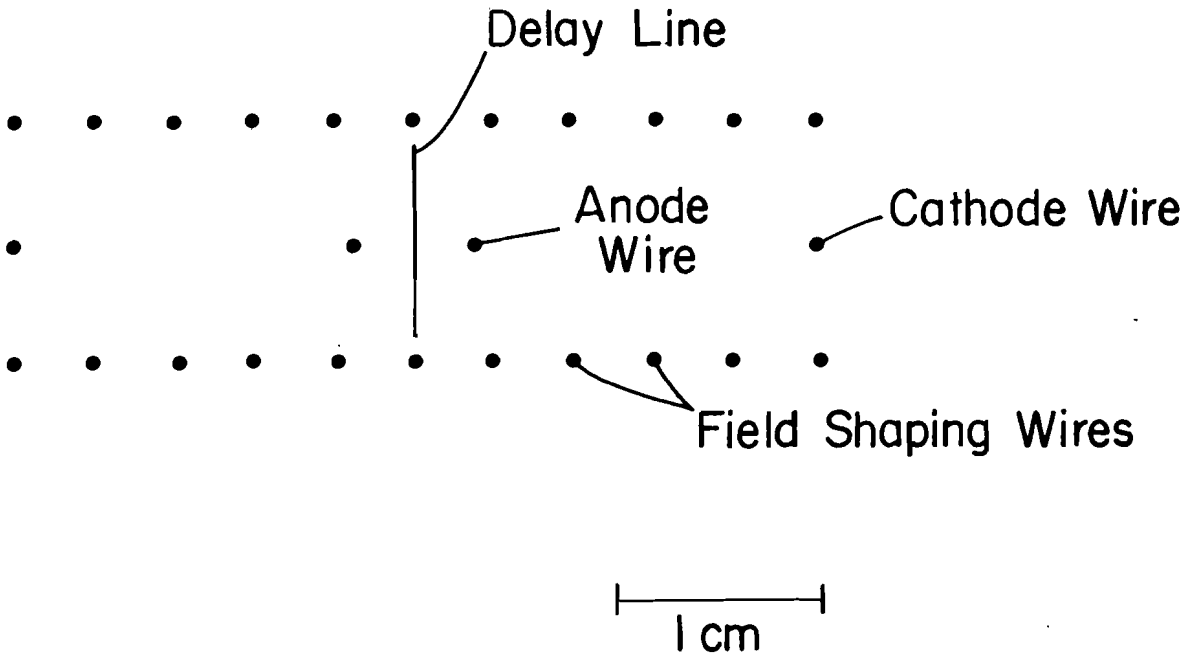

Figure 3-10

Drift chamber cell construction

information and the delay line delay times to the amplifiers at the top and bottom of the drift chambers, the y position could be determined to an rms accuracy of 3.0 cm. The drift chambers' construction and electronics are described in more detail in the thesis of Paul Schoessow (1983).

3.4 Timing and Hodoscopes

Two hodoscopes were located downstream in the experiment--the H hodoscope directly downstream of the Cerenkov counter and the M hodoscope directly downstream of the hadron absorber. The H or HADRON hodoscope consisted of 54 active elements arrayed in two rows of 27 each with a vertical gap in the middle to prevent firing by beam particles as shown in Figure 3-11. The dashed lines in this figure locate the boundaries of those gas Cerenkov cells located upstream of the H hodoscope which were used in a charged kaon trigger, as explained in Appendix C. To insure an interaction, the dimuon trigger required at least one hit in the H hodoscope.

The M or MUON hodoscope consisted of 44 active elements arranged in a "bow-tie" configuration as shown in Figure 3-12. The 8 dashed elements are members of the M' hodoscope downstream of the M hodoscope; this hodoscope did not enter into the trigger except under test conditions. In addition, a small (8" x 8") scintillator was

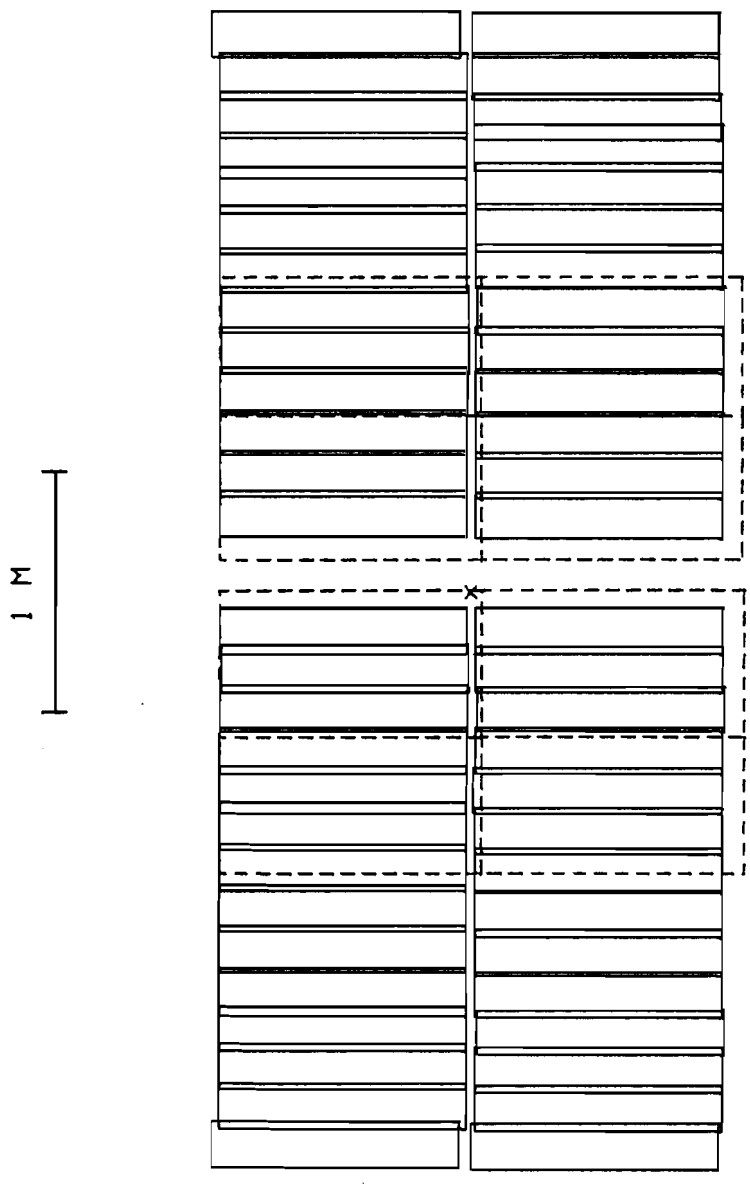

Figure 3-11

The H (hadron) hodoscope

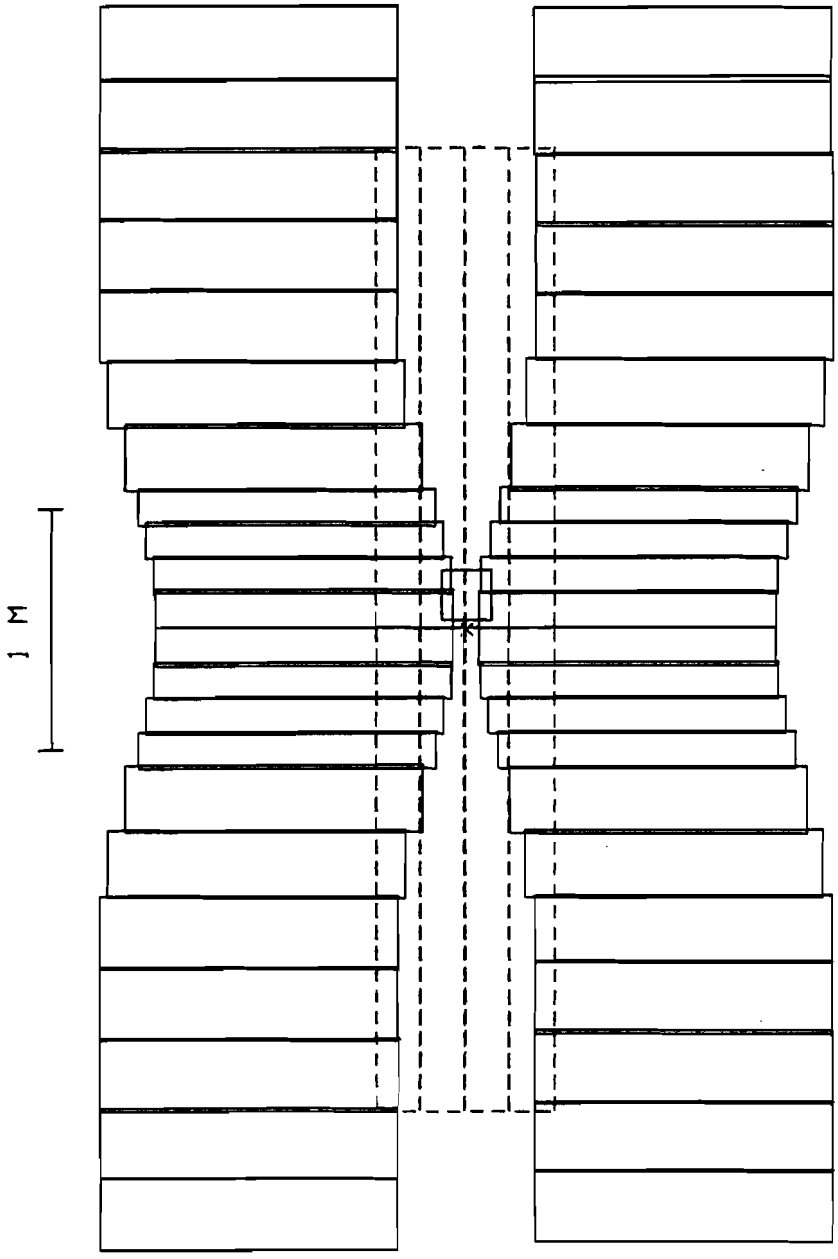

Figure 3-12

The M (muon) and M' hodoscopes

located on the M hodoscope centered on the deflected beam line to act as a further veto against triggers caused by beam particles.

The prime requirement of the dimuon trigger was two hits in opposite quadrants of the M hodoscope. Ideally, only muons should have remained downstream of the hadron absorber, and two hits in opposite quadrants would strongly favor opposite sign pairs of muons. Also, the "bowtie" shape of the M hodoscope biases the triggers toward dimuon pairs with a large p_T. Consider a negatively charged muon, with longitudinal momentum p_L along the beam axis and transverse momentum p_T, passing through the magnet. Then the possible locations of the muon at the M hodoscope lie approximately on a circle with radius and center:

$$r = p_T(z_M - z_T)/p_L = p_T(2210.30 \text{ cm})/p_L$$

$$x = -p_K z_M/p_L = -(2.115 \text{ GeV/c})(1469.20 \text{ cm})/p_L$$

where p_K is the transverse momentum kick due to the CCM; and z_T and z_M are the locations of the target and the M hodoscope. Likewise, a positively charged muon at the M hodoscope lies along a circle with the same radius but with the center the same distance in the opposite direction from the beam axis. The "bow-tie" shape of the hodoscope has been arranged such that the slope of the edges of the elements closest to y = 0 cm is $|y/x| = 0.22$. Equating this slope to the slope of the maximum y location on the circle of possible locations for a muon, we see that $|y/x| = r/x = p_T/(0.711 \text{ GeV/c}) > 0.22$. Taking into

account all possible locations on the circle, the "bow-tie" shape restricts the muons accepted to have:

$$p_T > (0.158 \text{ GeV/c}) \sin\phi$$

where ϕ is the azimuthal angle with respect to the x-axis. Of course, real dimuon pairs are not so ideal in that the total dimuon momentum vector has a component transverse to the beam axis and the muon momentum vectors are changed by multiple scattering in the steel hadron absorber, and the setting of the slope and width of the hodoscope were decided upon by Monte Carlo investigations and dead time considerations. All of these biases were designed to enhance the J/ψ signal over low-mass pairs as much as possible.

3.5 Gas Cerenkov Detector

Located between the two pairs of drift chmabers downstream was a large Cerenkov counter with more than 2 meters of radiative length in dry nitrogen at atmospheric pressure. This was divided up into 18 cells each about 60 cm in x and 110 cm in y (Figure 3-13). The pion and kaon thresholds were 6.0 and 21.0 GeV/c. A vertical gap in the middle allowed beam particles to pass through without interference. Each Cerenkov mirror overlapped three H hodoscope elements; a lit H element without a signal in the corresponding Cerenkov element then provided a quick indication of a kaon and, in fact, such a trigger was created in the logic to detect dikaon pairs and was used during part

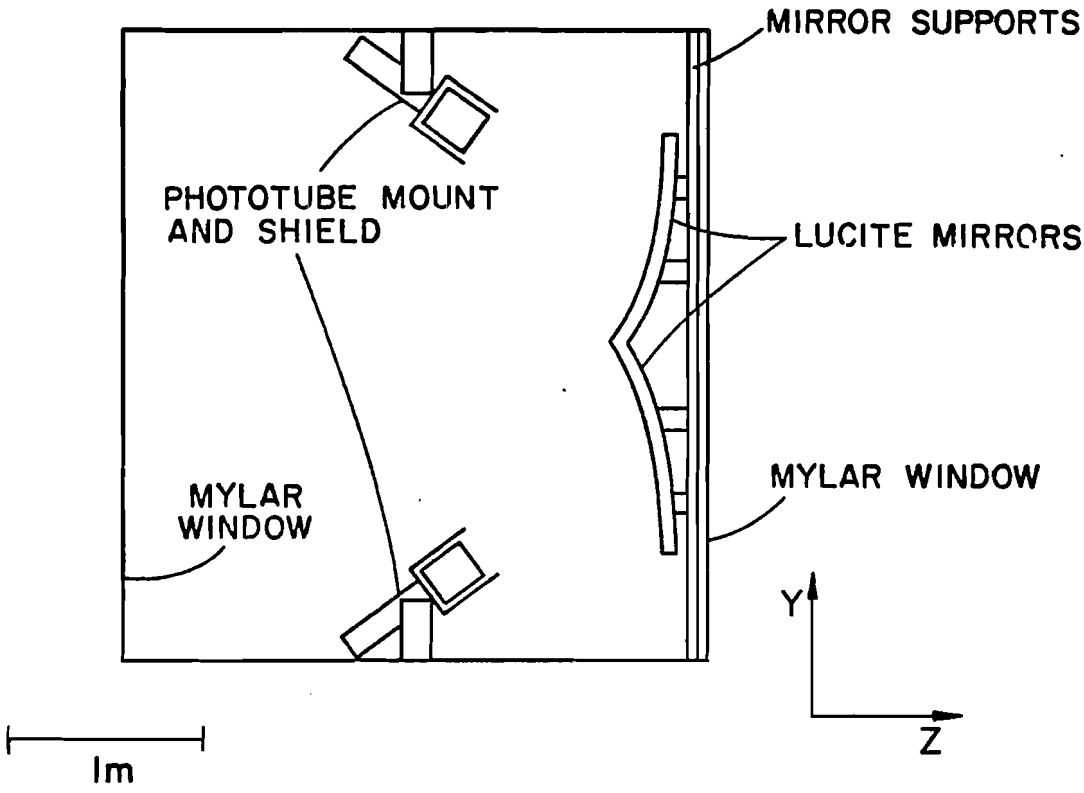

Figure 3-13

The gas Cerenkov counter

of the run. The construction and usage of the gas Cerenkov counter are elucidated in the theses of Paul Schoessow (1983) and James Proudfoot (1978).

3.6 Lead Glass Shower Detector

Located between the last drift chamber and the steel hadron absorber was the lead glass shower detector. The construction of the lead glass detector is described in detail in Appendix A, but a brief description of its components is given here (Figure 3-14). The bulk of the lead glass was encased in a large steel box. This portion of the detector consisted of 99 large lead glass blocks and a hollow aluminum rectangular cylinder or "beam box", all laid longitudinal to the beam direction. The lead glass blocks fell into three categories: 1) University of Illinois lead glass blocks purchased specifically for this experiment from Sovirel (type CEREN 25, comparable to SF5) and of dimensions 15.0 cm X 15.0 cm X 46.0 cm; 2) "Lederman" lead glass blocks of the first type (long) on loan from an inactive Fermilab experiment (E255) of SF5 type lead glass and of dimensions 14.7 cm X 14.7 cm X 46.0 cm; and 3) "Lederman" lead glass blocks of the second type (short), also of SF5 lead glass and of dimensions 14.7 cm X 14.7 cm X 40.0 cm. There were 47, 28, and 24 of each type, respectively. Figure 3-15 shows the locations of each type in the longitudinal array. Individual photomultiplier tubes were epoxied to

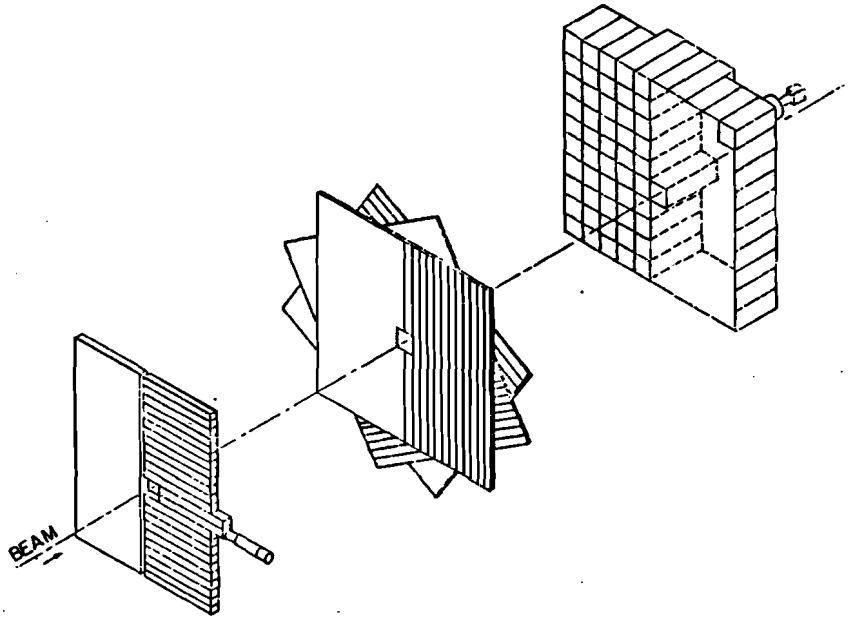

Figure 3-14

An exploded view of the lead glass array

(from left to right)

1) Active transverse lead glass blocks

2) Three planes of proportional tubes

3) Active longitudinal lead glass blocks

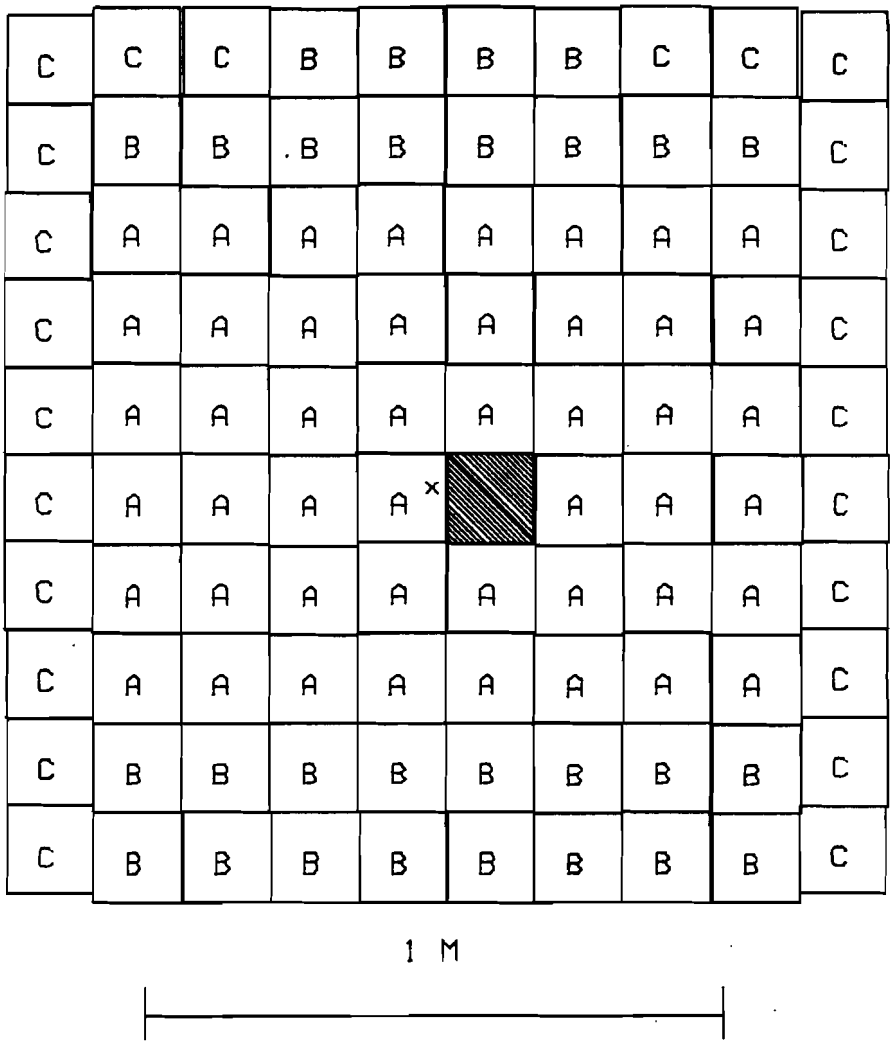

Figure 3-15

Longitudinal lead glass blocks

A - University of Illinois lead glass blocks

B - Long "Lederman" lead glass blocks

C - Short "Lederman" lead glass blocks

the downstream end of each lead glass block, serving to measure the Cerenkov light from all the electron track lengths produced by an electromagnetic shower contained within the block.

Clamped to the front of the longitudinal array was the P-tube array. This array consisted of three planes of 194 proportional tubes each; each tube was 60 cm in active length with an inner diameter of 1.128 cm. The first plane was x-measuring while the other two were rotated at $+60^{\circ}$ and -60° to the x-measuring direction. Through the use of the amplitudes of the signals on these proportional tubes, we could determine shower centroids. Upstream of the P-tube array was the transverse lead glass array. This array consisted of 48 oblong lead glass blocks laid tranverse to the beam direction in two adjacent stacks of 24 blocks each (Figure 3-16). These lead glass blocks were provided by Tufts University and had been used in the predecessor to this experiment. The blocks were composed of SF2 lead glass and measured 6.35 cm X 6.35 cm X 50.4 cm. Each transverse lead glass block was glued to an individual photomultiplier tube. Strapped to the front of these two stacks was 0.92 radiation lengths of lead and iron sheet.

The intended purpose of the entire lead glass array was as follows. Photons enter and begin showering either in the passive radiator or the transverse lead glass blocks. The electromagnetic

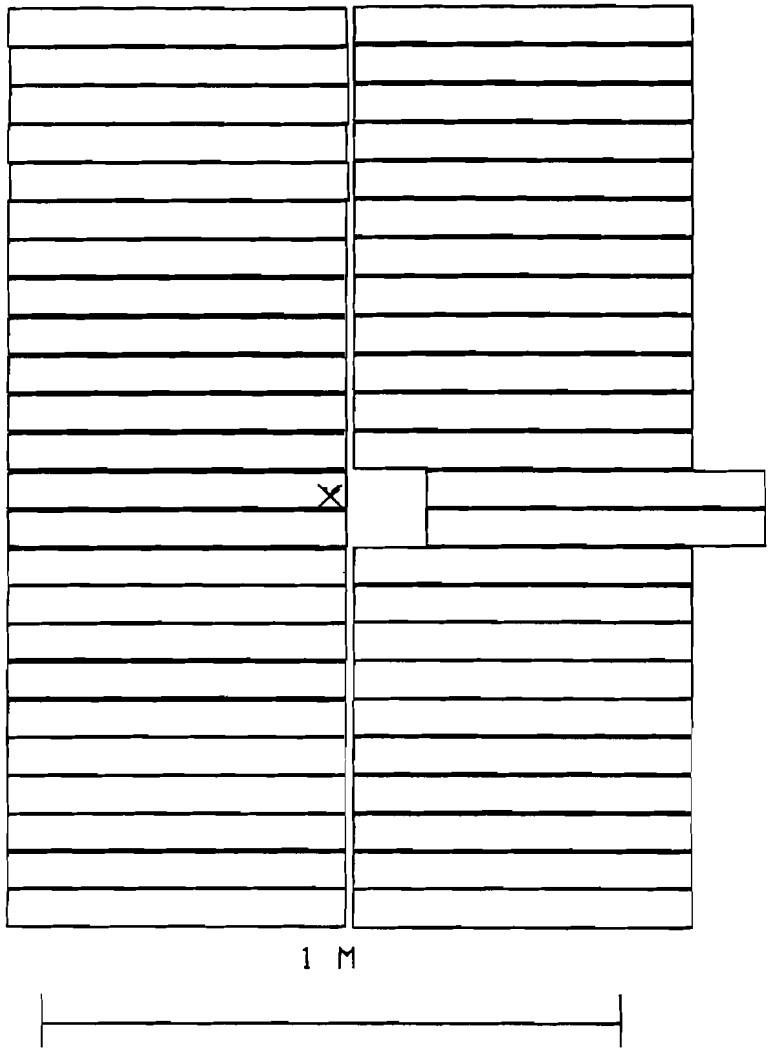

Figure 3-16

Transverse lead glass blocks

shower has developed enough by the time it leaves the transverse array and enters the P-tube array that a distinct signal is seen in each of the three planes. Using the intersection of the three planes' signals and weighted by the signal strengths in the tubes involved, a centroid of the shower can be found, giving a good determination of the photon location at the plane of the P-tubes. The remainder of the shower's development is contained within the longitudinal blocks behind the P-tube array. The Cerenkov light of the electrons in the shower is detected by the phototubes in both the transverse and longitudinal arrays and determines the total energy of the shower and thus the photon. In addition to the "beam box" at the center of the longitudinal array, a hole is provided in both the transverse array and the P-tube planes so that the non-interacting beam particles may pass thru the entire array without showering.

In addition, several calibration systems were associated with the lead glass array. Attached to each lead glass block at the end opposite the phototube was a coupling block by which light from either a green LED or a light fiber connected to an argon flash lamp could be injected into the block for calibration purposes. The LED's were provided voltage and triggered by special electronics in the racks. Each lead glass array had one argon flash lamp assembly through which light from the lamp was diffused into a bundle of light fibers which then spread out to each lead glass block. The longitudinal array's

argon flash lamp assembly sat atop the steel box in which it was encased; the transverse array's argon flash lamp assembly sat atop the steel frame in which these blocks were enclosed. An extra phototube was directly coupled to one fiber from each assembly to provide a correlation between the two arrays calibrations. The P-tubes were provided with two systems to check their calibration. First, their associated electronics (the RIRODAC and LARC systems; see Appendix A) were provided with the capability to inject a test charge onto each P-tube wire. Thus, the linearity of the electronics associated with each tube could be tested by injecting different test charges and reading the results out; in fact, it was found to be not linear, but linear plus quadratic. Second, a separate test P-tube was continually irradiated by an Fe-55 source; this P-tube was provided with the same gas flow as the other P-tubes. Thus, by noting changes in the spectrum of signals from this test P-tube, problems due to gas flow, gas composition, temperature, pressure, and high voltage fluctuations could be averted.

3.7 The On-line Computer and Electronics

The on-line computers and associated electronics are described at length in Appendix B; the trigger logic is described in Appendix C. A brief description is included here. Two on-line computers were used to read in the data when an experimental trigger was received: an

LSI-11/23 was used to read in the data from the P-tube array, while, in parallel, a PDP-11/45 read in the remainder of the data. Then, making use of the free time between events, the information on the LSI-11 was transferred to the PDP-11 and then all the data was logged to tape. Between spills, special records were written to tape containing calibration data and data on the high voltage supplies for the lead glass and the hodoscope phototubes. Each group of apparatus had its own special electronics and high voltage supplies associated with it. The beam line apparatus had special high voltage supplies and signal amplifiers located at the downstream end of the experiment. The 80 cm chambers had their own high voltage supplies, electronics, and gas systems located near the target cave; nearby were located the high voltage supplies, electronics, and gas systems for the University of Illinois chambers in the magnet, as well as a rack of upstream logic modules. The high voltage supplies and electronics for the drift chambers, the gas Cerenkov counter, and the lead glass array were located in the main racks on the west side of the lab downstream of the magnet. The high voltage supplies and electronics for the H and M hodoscopes were located on top of the steel hadron absorber. The gas systems for the drift chambers and the P-tube array were also located atop the steel. All data from all systems eventually arrived in its final form in a CAMAC module in a CAMAC crate (AEC CAMAC Standard TID-25875, 1972; TID-25876, 1972; TID-25877, 1972;

TID-26488, 1973); five crates were connected serially to the PDP-11 (one in the Portakamp and four in the lab proper) and two crates were connected serially to the LSI-11. Two data buffer modules allowed the data transfer between the LSI-11 and the PDP-11. In general, the information from the MWPC's and the drift chambers required an intermediate stage of data compression internal to the specific system before the data was passed to the CAMAC module; whereas the other data (i.e., phototube anode outputs, proportional tube peak voltages, and hodoscope element latches) were fed directly into the appropriate type of CAMAC module. The method by which these signals were read into the computer from the CAMAC modules is described in detail in Appendix B.

CHAPTER FOUR

PRELIMINARY DATA ANALYSIS

4.1 Test Run Analysis

In the spring of 1980 we conducted a test run to determine what scheme should be used for assembling the various parts of the shower detector so as to obtain the best possible location and energy resolution. At this point, the pieces of apparatus we had available consisted of one 80 cm chamber, a small prototype P-tube array consisting of one plane of 20 tubes, and several blocks each of the University of Illinois lead glass and the Tufts University lead glass. The beam line was reconfigured for use as an electron beam, a technique which we also used for our electron calibrations of the lead glass during the actual run. Fermilab provided the necessary electronics and a PDP-11 for data acquisition and tape logging.

Reconfiguring the beam line for electrons required two changes. First, a dipole magnet 347 m upstream of the CCM center was stuffed with blocks of polyethylene. Here the incident particles, mostly negative pions, produced neutral pions which gave rise to electrons through Dalitz decays or gamma conversions. Secondly, the beam line downstream of the polystyrene was retuned so that the optimal flux of electrons at the desired momentum was brought into the experimental

area. An experimental target was absent; the beam of electrons contaminated by pions was directly incident upon the test apparatus.

The electrons' straight-line tracks were detected by the beam chambers and the 80 cm chamber which was placed just upstream of the experimental shower detector in the Muon Lab. There were either one stack of 12 transverse (pre-converter) blocks or two stacks, one behind the other as presented to the beam, of 24 transverse blocks. This was followed by the test P-tube plane of 14 tubes and then a 3 x 3 array of Illinois longitudinal blocks. The shower detector components were than arranged as desired: first, one or two layers deep of transverse lead glass; second, the P-tube prototype plane; and last, the University of Illinois blocks laid parallel to the beam direction. Also the distances between the three components were varied in different tests. The Tufts blocks were 2.4 radiation lengths across and the Illinois blocks were 18.1 radiation lengths in length.

A standard arrangement of blocks is shown in Figure 4-1. Usually, the electromagnetic shower was well developed by the time it entered the P-tubes regardless of whether there was one or two transverse layers of blocks before the P-tubes. Thus, the location of the shower as found in the P-tubes was separated from the problem of finding the energy of the shower. Given the pulse heights in the

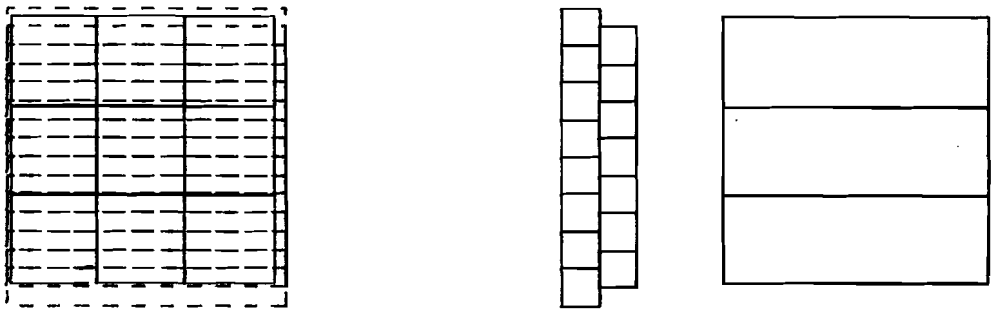

Figure 4-1

Test run lead glass apparatus

single plane of P-tubes, what was the most effective algorithm for finding the location of the shower centroid in the direction measured by that plane (in this case, the y-direction)? The simplest route to take was to define a centroid by:

$$\bar{y} = \frac{\sum_i y_i PH_i^N}{\sum_i PH_i^N}$$

where PH_i is the pulse height (pedestal subtracted) in the i-th P-tube, y_i is the location of the i-th P-tube, N is a constant power varied to optimize the resolution of the algorithm, and the sums are taken over all the P-tubes in the plane for a single event in the plane. This defined a centroid for the shower as found by the P-tubes which could then be compared with the location of the electron found by projecting the electron track into the plane of P-tubes. This track was found by projection from the center of the rotating dipole magnet 13.5 m upstream of the CCM into the single 80 cm chamber located just upstream of the test shower detector. The resolution was just the wire spacing of the 80 cm chamber, for a sigma of $0.159/\sqrt{12} = 0.046$ cm.

In all cases, it was found that the width of the difference between the P-tube centroid and the projected electron location was wider for N=1 or 4 and was fairly flat across the region of N=2 or 3. We have therefore set N=2. We also compared the results using a

single or double transverse layer of lead glass before the P-tube plane. The events selected for these tests were required to have more than a minimal signal in the longitudinal block giving the largest signal. This minimum was 300 ADC channels for a single transverse layer and more than 500 ADC channels for a double transverse layer. An ADC channel corresponded to 0.25 pC of collected charge and about 100 MeV of energy in a shower. These cuts insured that the particle showering in the array was an electron. Unfortunately, it was not realized until after the test run that the distance between the transverse blocks and the P-tube plane was critical; thus the results shown for this variable were found by Monte Carlo calculations using a electromagnetic shower simulation first written at the University of Rochester (Feller 1975). The results are shown in Table 4-1. The worse resolution for real data as opposed to the Monte Carlo results reflect problems that existed with the P-tube read-out which will be discussed later in the shower finding section. It is clear that it is better to have the P-tubes flush with the back of the preconverter blocks.

The calibration constants for each block—that is, the shower energy per ADC channel after subtraction of pedestals—were found by minimizing:

$$\chi^2 = \sum_j (E_j - \sum_i PH_{ij}\lambda_i)^2$$

where the j summation is over all events and the i summation is over

Situation	Distance from transverse lead glass to P-tubes (cm)	FWHM(mm)	# of events
Test run; double layer of transverse blocks; P-tube frame flush to transverse blocks	0.0	8.80	~400
Test run; single layer of transverse blocks; P-tube frame flush to transverse blocks	0.0	8.00	~800
Monte Carlo; double layer	0.0	3.2	
Monte Carlo; single layer	0.0	2.8	
Monte Carlo; double layer	2.0	4.4	
Monte Carlo; single layer	2.0	4.0	

Table 4-1

Test run P-tube position resolution

all blocks involved in the j-th event. E_j is the energy of the j-th electron as found by the beam routine (as discussed in section 4.2), λ_i is the calibration constant for the i-th block, and PH_j^i is the signal in ADC channels for the i-th block in the j-th event. Taking the derivative of this chi-squared and setting it equal to zero gives:

$$\lambda_i = \sum_j (A^{-1})_{ij} \sum_k E_k PH_k^j$$

where A_{ij} is a symmetric matrix:

$$A_{ij} = \sum_l PH_l^i PH_l^j$$

summed over all events. In the test run, all the electrons entered only two of the longitudinal blocks, and so these blocks and the five transverse blocks in front of them were used to form a 7 X 7 array A_{ij} which in turn was used to calculate the calibration constants. This set of calibration constants was used to calculate the shower energy. For 342 events which passed the same cuts as discussed for the P-tubes' centroid tests and the additional cut that in the 80 cm chamber the associated hit be within ± 5 cm of the beam line in x and y, a FWHM resolution of 0.80 GeV was found at a beam energy of 14 GeV. This corresponds to a σ/E of 2.4%.

4.2 Track Reconstruction

Off-line reconstruction of the charged particle tracks proved to be a difficult task in this experiment. This difficulty was due to the large particle multiplicities associated with the dimuon trigger,

the low efficiencies of the MWPC's in the magnet and of the downstream drift chambers, and the large number of "light-ups"—oscillatory behavior of the MWPC's resulting in many wires giving a signal without actually having a particle pass nearby. Two main track-finding algorithms were used: an early version using the tracks upstream of the CCM to search for corresponding "hits" in the MWPC's in the magnet, and a later version which used "hits" in the University of Illinois MWPC's in the magnet and tracks upstream of the CCM in the 80 cm chambers to predict where further hits in the magnet MWPC's might be. In both cases, the drift chambers, due to their low efficiency, could only be used as a "vernier" to better define the downstream track and not as predictors of tracks. The first of these two track-finding algorithms is defined in greater detail in the thesis of Sahadat Hossain (1981), and the second is defined thoroughly in the thesis of Howard Budd (1983). I shall describe both briefly here.

Both trackfinders start out in approximately the same manner—by finding a beam track in the beam chambers and an upstream track in the 80 cm chambers. The beam track is found by looking at the beam hodoscope elements which are on and the hits in the beam chambers. The ideal beam track has associated with it a single hit in each beam chamber and a single element lit in each beam hodoscope. In actuality, the trigger logic required at least one element in each beam hodoscope (Appendix C); however, this by no means insured that

the elements lit were those which intercepted the track. Also, due to the large fluxes of particles passing through these chambers and hodoscopes for many years, their efficiencies were not good—an average of about 90% for the beam chambers and about 95% for the beam hodoscopes. Thus, every bit of available data had to be utilized. A beam momentum was found for every beam track by observing the bending in the final steering magnet before the beam enters the lab. A beam track was defined upstream of this magnet using beam hodoscopes BH1 and BH2 and beam chambers BC1 and BC2 (see Figure 3-5). Another beam track is defined downstream of 1E4 using BH3, BH4, BH5, and BH6 and BC3, BC4, BC5, and BC6. These tracks are then required to match at the midplane of 1E4 within the resolutions of the tracks as found by using the resolutions of those chambers and hodoscopes which made up the track. If they did not match, a nominal momentum was assigned to the beam particle. If they did match, then the "kick" imparted to the beam and the known magnetic field of 1E4 as function of magnet current allowed us to calculate the beam particle's momentum. Furthermore, the projection of the beam track from BC3, BC4, BC5 and BC6 into the target allowed a verification of the interaction vertex independent of that found from the tracks in the 80 cm chambers.

The upstream (of the CCM) trackfinding proceeded in the same way for both the early and the later trackfinders. Essentially, the best tracks in the 80 cm chambers were extrapolated back to the target and

examined for a cluster of tracks occurring near each other. These tracks, along with the beam track, were then averaged to define the primary vertex. Using this vertex as the origin of all the upstream tracks, lower quality tracks were then found in the 80 cm chambers. The more recent trackfinder improved on the old scheme by recalculating the primary vertex using all tracks found up to this point. If the location of the vertex changed by more than 0.4 cm, the new vertex was used to repeat the entire process. At this point, tracks in the x- and y-views are still independent of each other. Upstream tracks are searched for in the 80 cm x-planes for the x-view and both the 80 cm y-planes and the University of Illinois y-planes for the y-view, because the bend in tracks in the y-view due to vertical focusing is too small to affect trackfinding at this crude level. Also, in the more recent trackfinder hits in the tilted 80 cm chamber were used in conjunction with trackfinding in both views, and the small (less than 1°) rotations of the 80 cm chambers from vertical and horizontal were used in the trackfinding.

Downstream (actually, in and downstream of the CCM) trackfinding was accomplished using only the University of Illinois chambers in the CCM due to the low efficiencies (averaging to 78%) of the drift chambers. The tracks through the CCM were first found using the method of standard tracks. For a given upstream track, a hypothetical match was made with a hit in a given University of Illinois chamber,

starting with the most downstream chamber UI5 (the University of Illinois chambers are designated UI1 throught UI5 from most upstream to most downstream) and working upstream. How hits were found in the University of Illinois chambers varied between the two trackfinders and will be discussed later. From a given hit in a University of Illinois chamber and an upstream track, a prediction can be made for associated hits in the remaining chambers. This could be done by actually predicting the orbit of the particle with a given magnetic field, or, more simply, by using a hard-edge approximation to the real magnetic field. But both these methods would consume an immense amount of computer time if done for every hypothetical track through the CCM for every event in the experiment. Instead, a standard track was used. In the earlier form of the trackfinder, there existed a single "standard track": the hits given by a negative particle passing through the CCM which enters along the beam axis and has a momentum of 5.1 GeV/c. In this case, the trajectory in the y-view was considered to be a straight line (i.e., vertical focusing is ignored). Given the hits in the x-view of the standard track, the actual upstream track, and a hypothetical x-point in a particular chamber, we can predict the locations of the other x-points in the remaining University of Illinois chambers as follows:

$$X' = X0' + (X-X0) \times DX'/DX$$

$$P = P0 \times DX/DX'$$

where the primed variables are for the chamber we are making prediction in and the unprimed variables are for the chamber with the hypothetical x-point. X0 and X0' are the locations of the x-points in the chambers if the upstream track were projected into the chambers. X is the location of the hypothetical x-point. DX and DX' the deviations from the beam axis of the standard track in the chambers. Thus, in a single line of calculation, a prediction for one chamber can be found. Also, the second line of calculation gives a quick rough estimate of the momentum of the particle. P0 is the momentum of the standard track and P is the estimate of the track's momentum.

In the later trackfinder, this method was made more sophisticated by using multiple standard tracks. A set of standard tracks produced by using the magnetic field map were produced for different incoming x- and y-slopes, and for different momenta. If a hypothesized track fit well enough to be used as derived using a standard track at the right x- and y-slopes at a standard momentum of 20 GeV, then it would be sent through the procedure again with the standard track of the nearest momentum as well, if the initial momentum prediction was less than 10 GeV. Furthermore, an approximation of the bending in the y-view was also included to take into account vertical focusing, which in extreme cases could give a 1 cm deviation from the straight-line trajectory.

The method of standard tracks is then applied to finding downstream tracks. Every pair of upstream x-view track and y-view track is then matched with hits in the University of Illinois chambers. Predictions of other hits in the other University of Illinois chambers are made using the method of standard tracks. If a hit is found within a certain distance (a "window") of the predicted hit, it is considered to also belong to the downstream track. This window ranged in size from 0.6 cm to 2.0 cm depending on how far the predicted point's chamber was from the chamber with the actual hit. The definition of a hit differed between the early and later versions of the trackfinder. In the early version, a hit was any match between a wire in the U or V planes (tilted 11° from the vertical) and a wire in the Y plane. This coordinate was projected onto the Y plane. In the later version of the trackfinder, the curvature of the track in the magnet is taken into account. An estimate of the "local slope" in x and y is made at the chamber in question, and a matched U-V hit is created taking this slope into account. These hits are used to predict hits in the other chambers, but the predicted hits need be only in any single plane. Finally, each total track (downstream track with its corresponding upstream track in both the x- and y-views) is checked for minimum total of hits required for storing the track. If two total tracks shared an upstream track or tracks, the best track was kept. The criterion for picking the best track was first number

of planes used, second the efficiency of the track (i.e., the ratio of number of planes used to the number of planes the track went through), and third the chi squared of the hits to the predicted track.

For the dimuon sample, only tracks with a momentum greater than 6 GeV were necessary, for only such tracks made their way through the CCM and into the M hodoscope. Thus, if the rough estimate of the track momentum was below 6 GeV, the track was no longer pursued. A separate low momentum trackfinder was written by H. Budd (Budd 1983). At this point, the slope and intercept parameters for downstream of the CCM were derived. A simple hard-edge approximation of the actual magnetic field was used to determine the downstream track parameters from the curvature and upstream track parameters of the particle. Small corrections to the radius and field strength of the hard-edge field as a function of the most downstream chamber with a hit associated with this track had to be made so that the downstream tracks correctly predicted hits in the drift chambers. The radius and field strength of the the hard-edge magnetic field were always varied so that the product of the two variables was a constant, and, thus, the momentum kick to a particle traversing the CCM was a constant. Also, a global upward correction to the field strength only of 0.7% had to be made so that the J/ψ had the correct mass.

The drift chambers could only be used as a "vernier" on the downstream track, due to their low efficiencies. This means that matches with the downstream track are made with hits in the drift chambers, and used to correct the downstream track parameters. Using the most upstream drift chamber hit, the downstream track parameters are corrected and then extrapolated again into the remaining drift chambers in search of more drift chamber hits.

The last correction to the entire track is a global fit to every hit associated with the track. This is described in detail in the thesis of P. Schoessow (Schoessow 1983), but I will redescribe it here briefly because some of the by-products of this process are used later in a 1-C fit to the mass of the J/ψ. With a complete knowledge of the magnetic field, the track is specified completely by its upstream track parameters and the momentum of the particle. Define a vector $\vec{T} = (A_x, B_x, q, A_y, B_y)$, where:

$A_x = x_o$ $\qquad$ $B_x = dx/dz$

$A_y = y_o$ $\qquad$ $B_y = dy/dz$

$q = 1/|\vec{p}|$

The slopes and intercepts are taken at the z = 0 cm plane. The global fit then reduces to minimizing the chi-squared of the sum of the residuals $(x_p^i - x^i)$ between the predicted hit and the actual hit in the i-th chamber plane and linearizing the resulting equations about x_{po}^i and y_{po}^i, the hits predicted by the simple hard-edge magnetic field:

$$\chi^2 = \sum_i \{ [(x_f^i - x^i)/\sigma_x^i]^2 + [(y_f^i - y^i)/\sigma_y^i]^2 \}$$

$$x_f^i = x_{f0}^i + \sum_j (\partial x_f^i/\partial T_j)\delta T_j = x_{f0}^i + \delta x^i$$

$$y_f^i = y_{f0}^i + \sum_j (\partial y_f^i/\partial T_j)\delta T_j = y_{f0}^i + \delta y^i$$

where after the first line, the errors σ_x^i and σ_y^i have been absorbed into the definitions of x^i and y^i. Differentiating the linearized χ^2 and setting the derivatives with respect to T equal to zero yields the matrix equation:

$$\sum_k A_{jk}\delta T_k = C_j$$

$$A_{jk} = \sum_i [(\partial x_f^i/\partial T_j)(\partial x_f^i/\partial T_k) + (\partial y_f^i/\partial T_j)(\partial y_f^i/\partial T_k)]$$

$$C_j = -\sum_i [(x_{f0}^i - x^i)(\partial x_f^i/\partial T_j) + (y_{f0}^i - y^i)(\partial y_f^i/\partial T_j)]$$

which can be inverted to solve for δT_k, the changes in the upstream track parameters and momentum which minimize the chi-squared.

For the final data sample of dimuons, one further improvement was made. The "magnet map"—map of the magnetic field strengths of the CCM—was used in minimizing the chi-squared as explained above. This map was measured during Fermilab experiment E98; unfortunately, no magnet mapping was done during our experiment. In the original version of the track fitter, the derivatives of the x- and y-points with respect to the track parameters and inverse momentum were evaluated exactly upstream (where the algebraic solution is simple) and numerically in the CCM and the drift chambers using a hard-edge approximation to the real magnetic field. The improved track fitter used the magnet map for these numerical evaluations and extended the

influence of the magnetic field beyond the hard-edge radius into the tilted 80 cm chamber and the most upstream drift chamber. The effects of each of these improvements—using the drift chambers, track fitting, and track fitting with the magnet map—will be shown in Chapter 5.

4.3 Shower Detector Data Analysis

Due to the complexity of the shower detector, the gamma finding algorithm reflected a commensurate complexity. The basic scheme was to define shower locations using the P-tubes, associate the pulse heights in the transverse blocks before this location and the longitudinal blocks behind this location with this shower, translate the pulse heights into energies, and thus define the four-momentum of the gamma or electron. In practice, the procedure involved many manipulations not apparent from the above algorithm due to the effects of pulse height gains changing with time, the non-linear relationship between the pulse height and energy, sharing of light between blocks from a single shower and sharing of light between nearby showers into common blocks, attenuation of light in both the transverse and longitudinal blocks, non-linearity and inefficiency of the proportional tubes response, and a multitude of other minor effects. Each of these had to be dealt with in turn.

First, I shall describe the gamma finder in its simplest form. This algorithm was developed by Pat Lukens and myself in response to our dissatisfaction with the previously used gamma finder (Hossain 1981), which found a surplus of low energy showers, duplicated showers, or found showers outside the array. The current E610 gamma finder works as follows. The pulse heights in the lead glass ADC's and the P-tube ADC's first have their pedestals subtracted using the pedestal averages found during the begin run calibration. The gains for the lead glass and P-tubes are read in from run-dependent indexed files. The pulse heights for the P-tubes are multiplied by their gains to give a quantity proportional to the equivalent track path "weights". The P-tubes in each plane were then sorted by weight demanding an arbitrary minimum of 80 channels as determined by examining the distribution of P-tube weights. Then "clusters" of P-tubes were searched for in each plane starting with the highest weight and working down. A cluster was defined as a group of seven contiguous tubes centered on the tube with the largest weight with at least two other tubes with a signal of at least 20 channels, counting only those tubes which were not already included in another cluster. Every intersection of clusters in the U-plane and clusters in the V-plane is then found and the longitudinal block behind this intersection is checked for a signal of more than 3 channels. Those intersections which pass this test are then matched with clusters in

the X-plane to define a "triplet". A maximum of two triplets are allowed in front of one longitundinal block: both must have the U-V intersection no more than 2.5 cm from the X cluster; one triplet is the nearest match in x, and the other allowable triplet is that with the largest sum of P-tube weights for the U-V pair. These define the locations of showers with the highest location quality. More showers are looked for in matches of an X cluster, a transverse lead glass block with a signal of more than 3 channels which is not in front of any previously found shower location, and an unclaimed longitudinal lead glass block with a signal of more than 3 channels. If an intersecting U or V cluster exists for such a match, it is used to further resolve the y coordinate (which defaults to the center of the transverse block otherwise). This defines a lower quality shower location. Lastly, U-X, V-X, or U-V matches are searched for in unused clusters, demanding more than 3 channels of signal in the corresponding longitudinal lead glass block. This defines the lowest quality shower locations. In all cases, the centroids of the showers are defined as explained earlier in the test run section. If two shower locations are found to be within 3.0 cm of each other, the showers are fused into one shower. At this point, each shower location is checked to see which blocks the shower could have energy in. The curve of radial energy deposition from a Monte Carlo study (Longo, 1975) is used out to the radius of 97% of the total energy,

which occurs at four times the radiation length or 9.44 cm in the longitudinal blocks. The radial energy deposition is numerically integrated and the expected fractions of the total shower energy for each of the maximum possible four blocks are stored. Every longitudinal block is tagged for every shower to which it contributes; and showers are marked as to whether they hold blocks in common with other showers.

Now the energies in the lead glass are calculated using the pulse heights and the gains. The energy in a transverse block is apportioned between the showers located in the block in the ratio of the P-tube weights of those showers. If a single longitudinal block contains more than one shower, no attempt is made to untangle the energies and the energy in the block is shared evenly between the showers. Otherwise, if a block contains one shower and spillage from showers in adjacent blocks or only spillage from showers in two or more adjacent blocks, the predicted energy fractions calculated earlier are used to calculate how the block's energy should be divided amongst the showers. Using the interaction vertex, the shower location, and the total transverse and longitudinal lead glass energy for a shower, the four-momentum of the shower is then calculated, assuming the cause of the shower to be a photon.

A graphics package was also developed along with the gamma finder for debugging and testing purposes. A typical event is shown in Figure 4-2. The three scales below and diagonal to the representation of the longitudinal blocks contain perpendicular lines with heights proportional to the pulse heights of the P-tubes in the three planes. The dashed line above the scale represents the threshold above which at least one tube had to fire to define a cluster of P-tubes. The lines drawn through the longitudinal blocks in the same direction as the P-tube pulse heights show the centroid of the clusters found in each plane. To each side of the longitudinal blocks is a segmented line. Those segments with numbers in them are representative of transverse blocks with the indicated energy in GeV. Likewise, the numbers in the longitudinal blocks indicate the energy in GeV contained within them. Shower locations are indicated by the circle within which 97% of the total energy is contained and a diamond at the center of this circle. One can then see if it satisfies the criteria of a shower with respect to the P-tube clusters and energy in the transverse blocks, and which blocks are expected to contain some of this shower's energy. Also, each shower has a number printed within the circle which corresponds to the number in the list of shower energies shown off to the side. Optionally, if track information is available, hadron and muon tracks can be indicated on the display by special symbols.

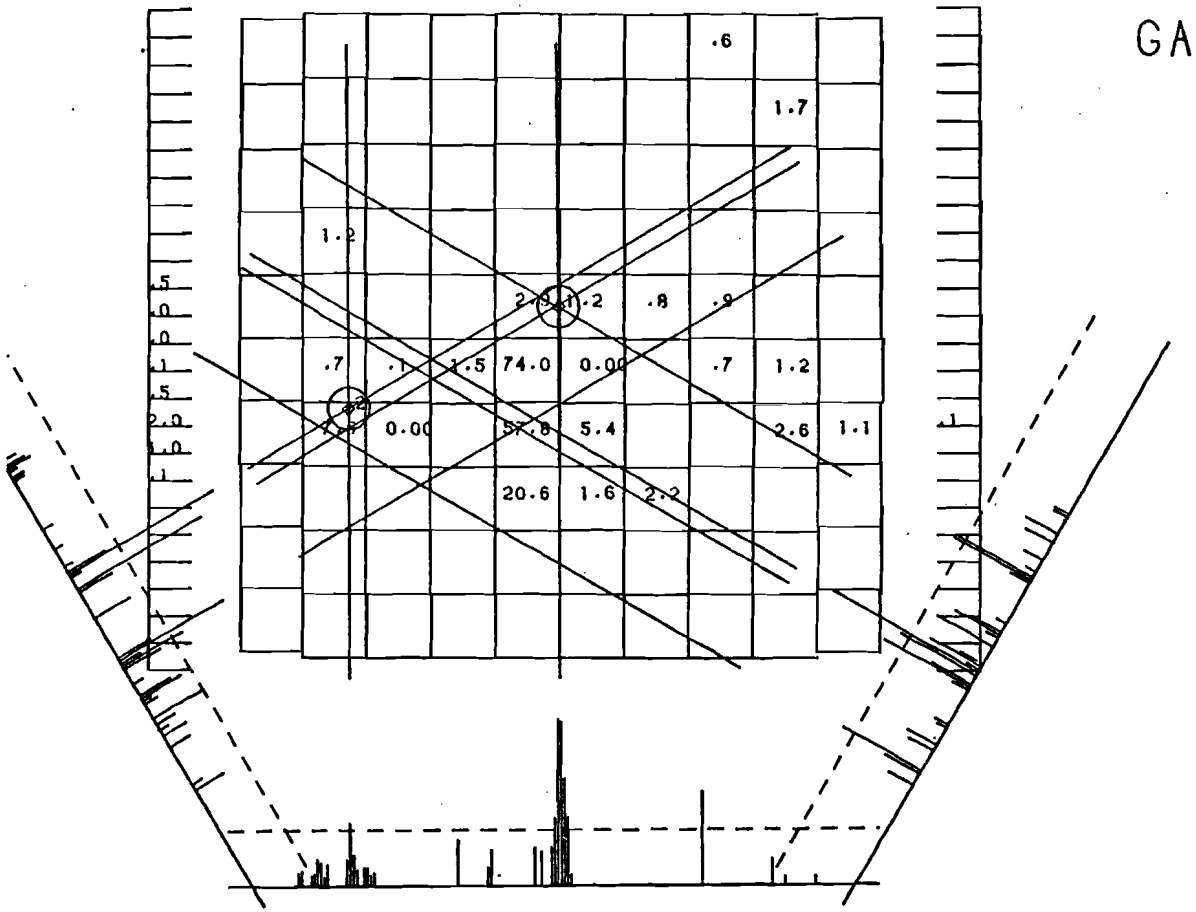

Figure 4-2

Typical lead glass event

The remainder of this section will deal with the corrections necessary to improve the gamma finder to its present state. First, the P-tube response to collected charge (which in turn is proportional to track length and number of electrons passing through the tube) was non-linear in the RIRODAC system's electronics. This was a known problem and a facility was built into the electronics to inject a known amount of charge into each amplifier and then read out the ADC values. After subtraction of the pedestal, the response fit a quadratic form with a linear term but no constant term. We found we obtained more consistent results if we matched the quadratic curve to a straight line after the point of the maximum injected charge; otherwise, the corrected pulse heights were unreasonably large for large uncorrected pulse heights. A typical plot of corrected pulse height versus uncorrected pulse height is shown in Figure 4-3. Other problems were associated with the P-tubes over which we had no control. The P-tube ADC's were peak voltage sensitive as opposed to collected charge sensitive; these were used because the RIRODAC system amplifiers output a signal whose peak voltage was proportional to the charge collected on the P-tube anodes. These pulses had a fairly long rise time of about 100 ns and, in addition, an undershoot after the pulse went down to the baseline. Thus, the effective deadtime of the P-tubes were longer than if there was no undershoot. Unfortunately, event deadtime did not allow the P-tubes to be gated as

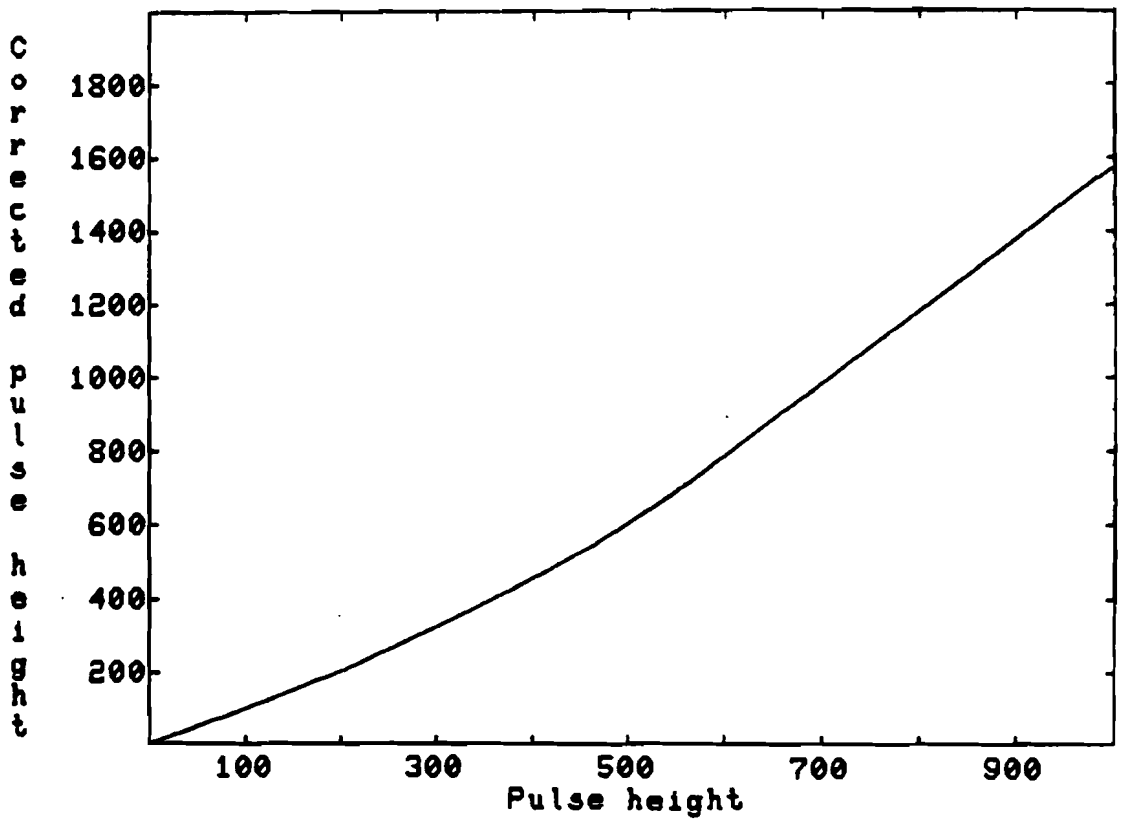

Figure 4-3

Typical P-tube pulse height correction

long as the undershoot so that accidentals could cause P-tubes to give the wrong reading.

Another problem which had to be taken into account was the "tracking" of the lead glass calibrations. Here, "tracking" means the use of the lead glass calibration systems to correct for time-dependent gain changes in the lead glass during the course of the experiment. The tracking problem can be divided into two parts: short-term gain changes and long-term gain changes.

Short-term gain changes were investigated by looking at the actual change in the calibration signals during the course of a run and by looking at the statistical deviations of the calibrations over the course of a single run. A good run entailed about 30,000 events written on tape (at 6250 BPI) and took approximately two hours. Two signals were available during the course of a run, the between-spill calibrations for both the LEDs and the argon flash lamp, and the "quick-calibration" calibrations for only the LEDs after each trigger. The logic and electronics necessary to accomplish this end are described in Appendices B and C. A typical plot of LED calibration versus event number is shown in Figure 4-4; a plot of argon flash calibration versus spill number is shown in Figure 4-5. L12 denotes a Lederman block in the second row from the bottom; UI22 is a University of Illinois block far from the beam block; UI46 is a

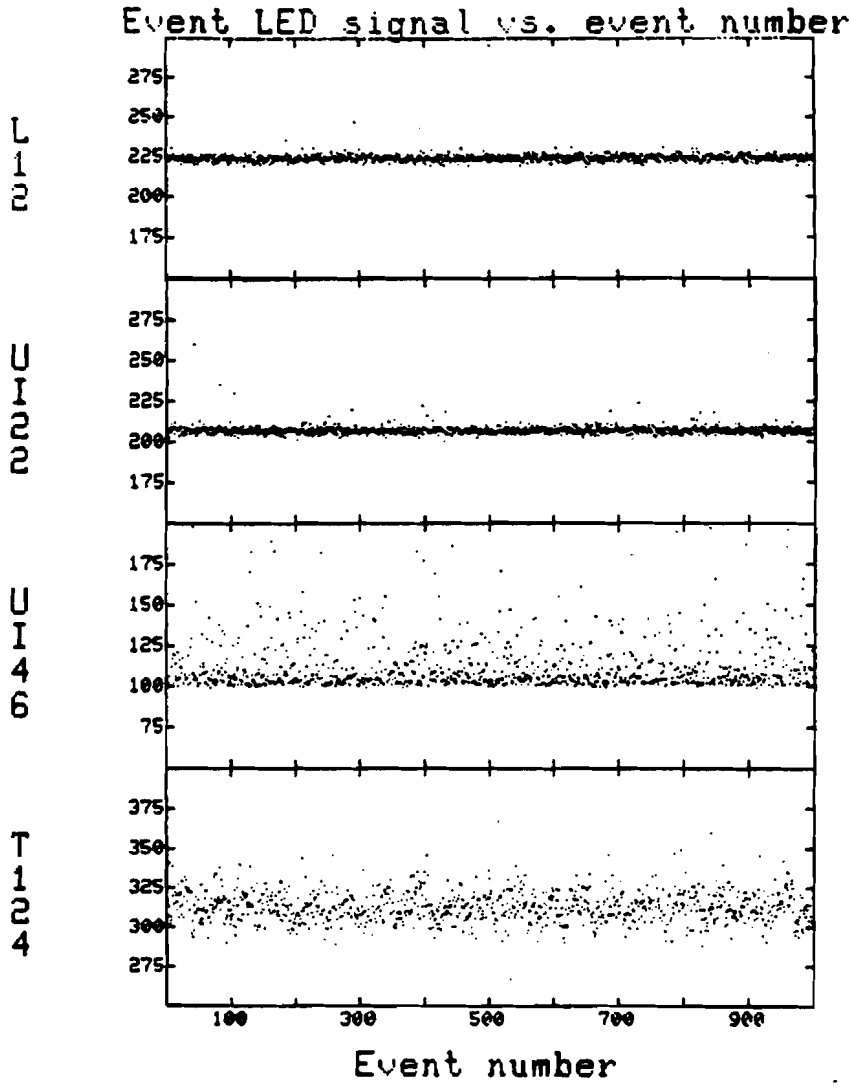

Figure 4-4

LED calibration signal versus event number

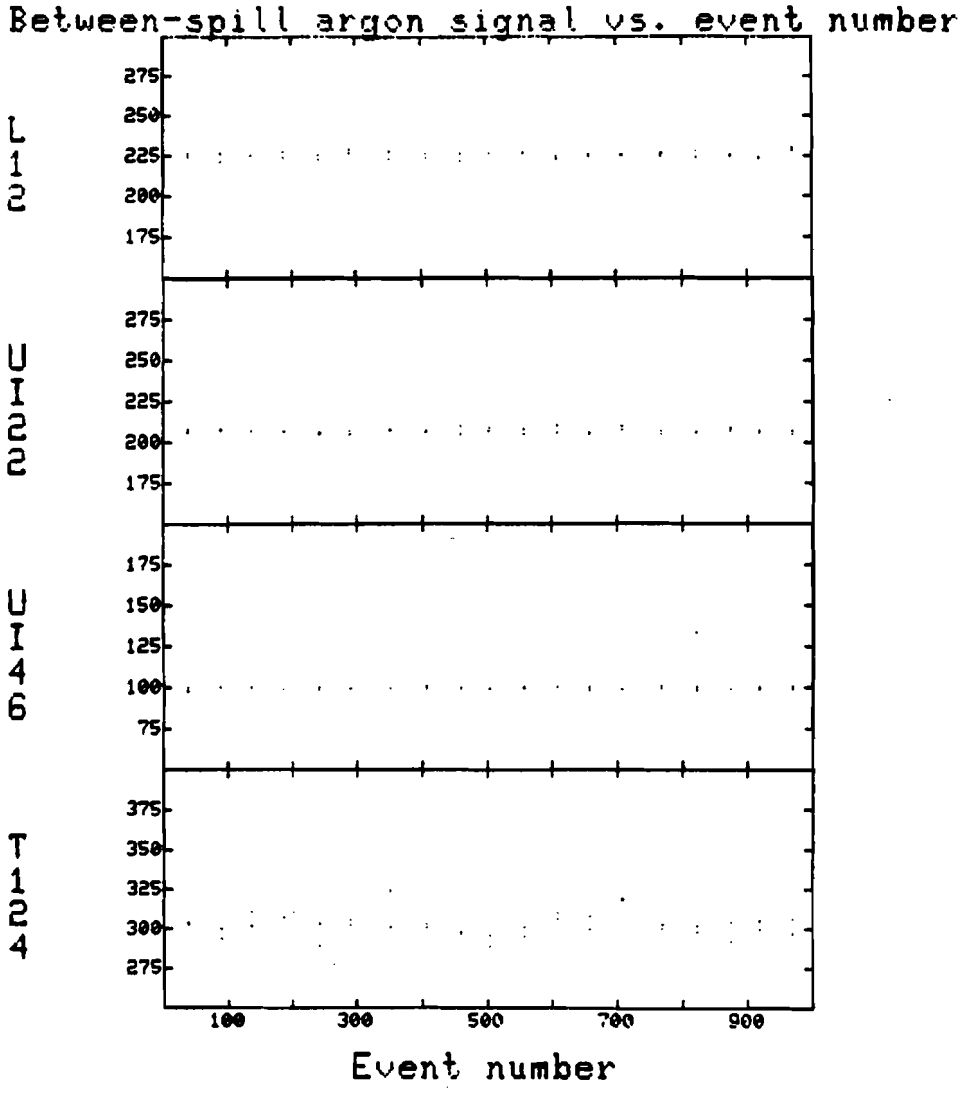

Figure 4-5

Argon flash calibration signal versus spill number

University of Illinois block adjacent to the beam block; and T124 is a transverse block which shadows UI46. As can be seen, the error in calibration is on the order of one or two channels (about 100 MeV of energy per channel) in the longitudinal blocks; the transverse block, with about five times the gain, has about five times the error. The points above the baseline are due to events where some energy was present in the lead glass block due to accidentals occurring while the "quick-calibration" sequence was underway, as can be seen by their greater incidence in the longitudinal block near the beam block. We conclude that short-term calibration problems were on the same order as the resolution of the apparatus, and so were ignored.

Long-term gain changes were a far more serious problem. The gain of each lead glass block was found on an absolute scale using electrons during two calibration runs before and near the end of dimuon running (the scale was known absolutely to the extent that the momentum of the electrons was known; this will discussed later). If we assume that a LED or argon flash is constant and equivalent to some amount of shower energy, and that the energy in the block is simply the gain times the pulse height, then any change in the gain is reflected by a change in the pulse height of the calibration sources, as follows:

$$G = G0 \times P0/P$$

where G and P are the gain and pulse height for this run, and G0 and

P0 were the gain and pulse height during the electron calibration run. Figures 4-6 and 4-7 show several lead glass blocks' LED and argon flash signals with pedestals subtracted averaged over each run for all the dimuon runs in the experiment where the signal was present. Two trends are evident: first, that for the blocks near the beam axis, there is a downward change in the signal over the course of the experiment, and, second, that the calibration signals varied a great deal from run to run. Also, the variance in the LEDs was much greater than that for the argon flash. The first observation is interpreted to mean that yellowing of the lead glass due to radiation damage occurred preferentially near the beam hole. Figure 4-8 shows the fractional percentage loss of total argon flash signal from the first calibration to the end of dimuon running, and confirms the yellowing. The argon flash system was found to be a more reliable calibration than the LED over the course of the experiment, both for its greater long-term stability and its marginally better short-term stability as reflected in the standard deviations of the two calibration signals for a single run. The green Monsanto LED's were found to have a temperature-dependent light output which probably explains their unstable behavior in the open environment of the Muon Laboratory, where the tempareratures could vary rapidly. However, neither calibration system did a good job of tracking the calibration as can be seen in Figures 4-9 and 4-10 where the fractional percentage

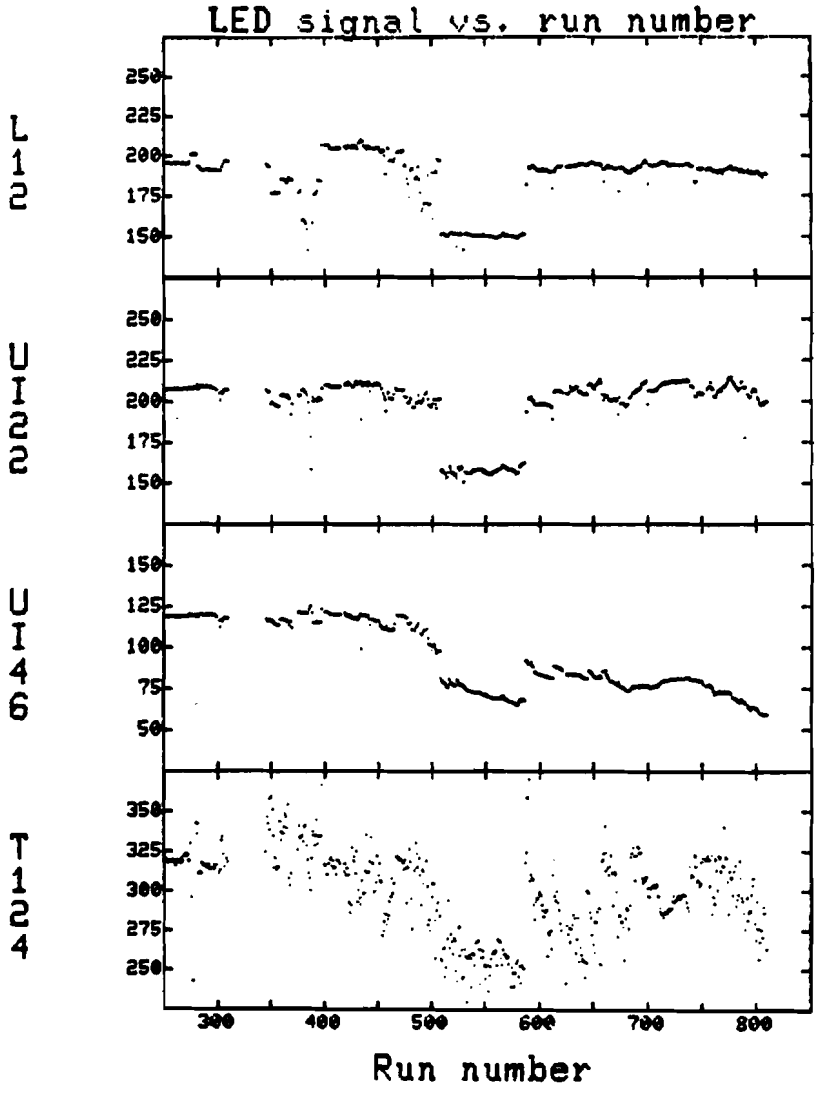

Figure 4-6

Averaged LED signal versus run number

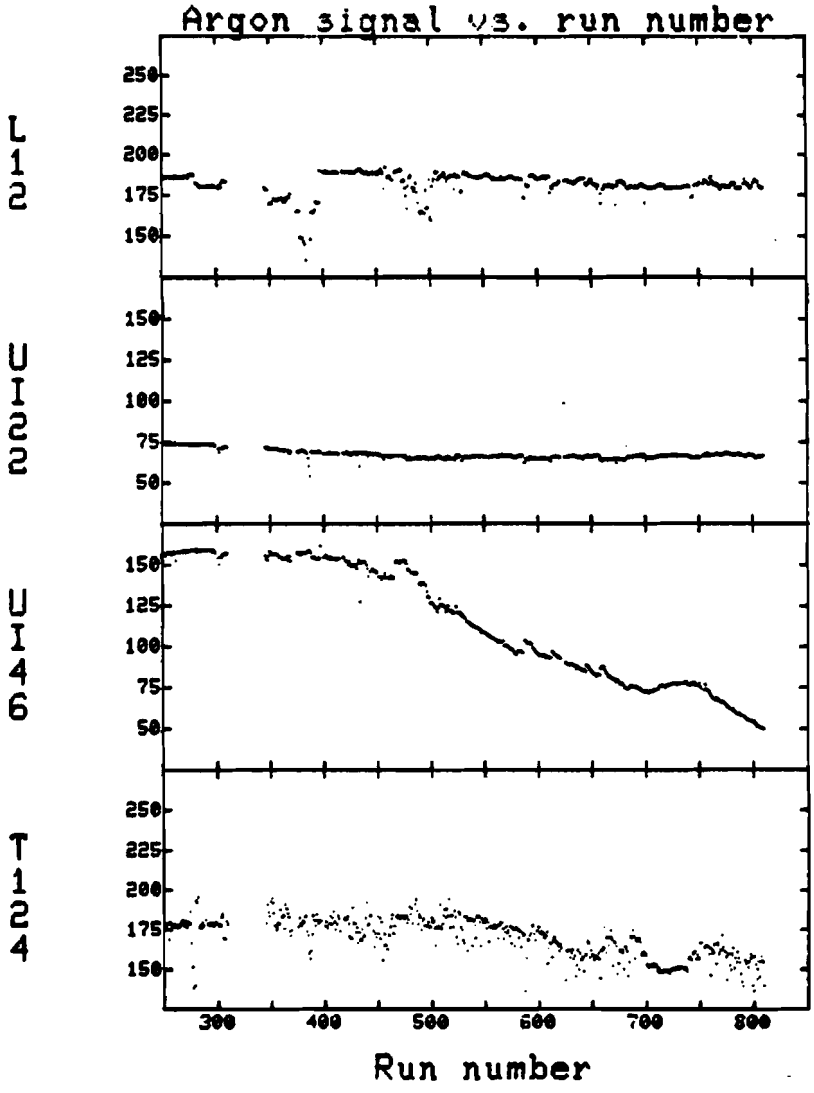

Figure 4-7

Averaged argon flash signal versus run number

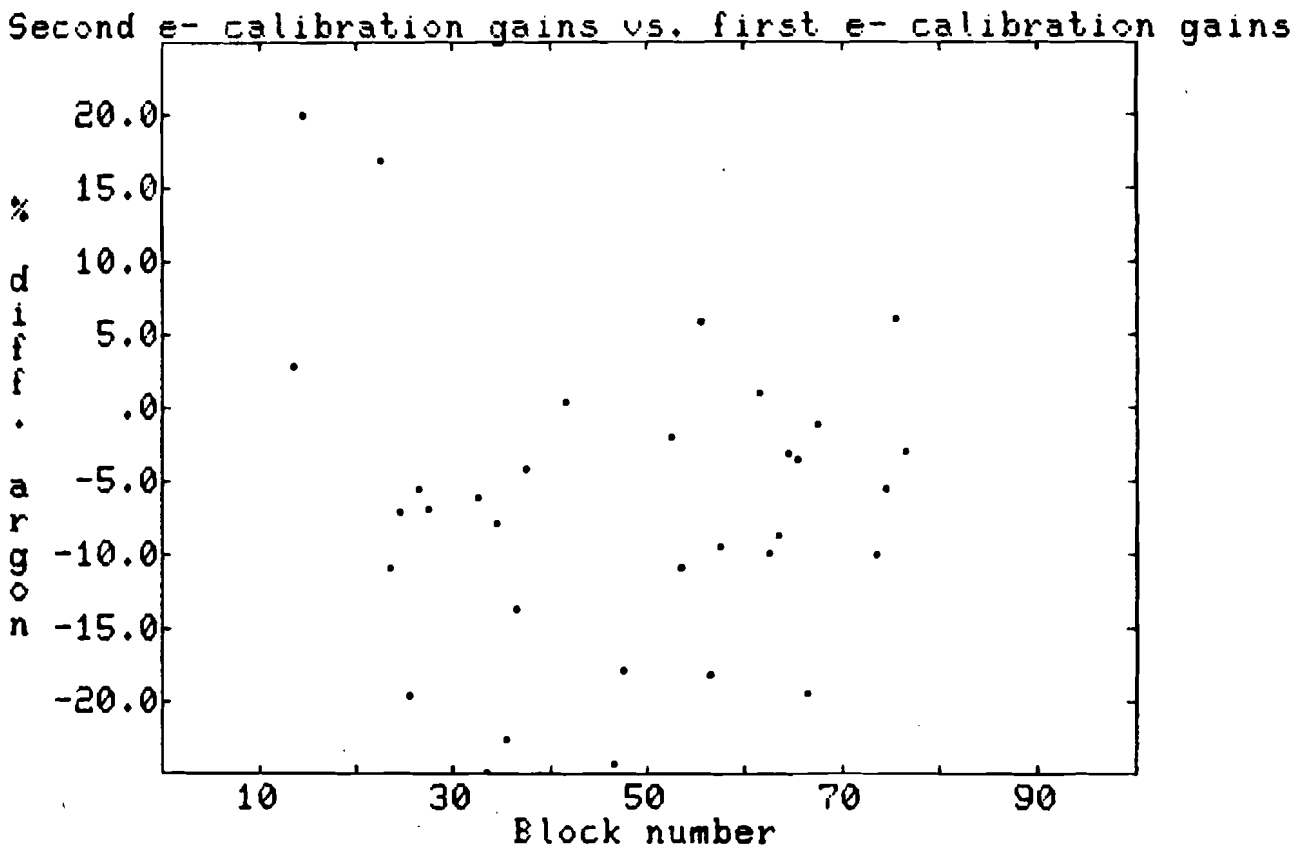

Figure 4-8

Percentage loss of argon flash calibration signal

differences between the actual calibration found in the second electron calibration and the predicted calibration found by tracking forward from the first calibration with either the LED or argon flash lamp are shown.

Another very serious difficulty was the non-linear response of the lead glass to energy. Unfortunately, data at several electron energies was available in only a few blocks, and data at all four energies (5, 10, 15, and 25 GeV—see Figure 3-4) was available in only two blocks—the two University of Illinois blocks immediately to the left and right of the beam box. A least-squares fit to this data indicates that the lead glass energy is not simply the gain times the pulse height but that energy plus an "offset" energy of 0.918 GeV (Figure 4-11). Of course, in actuality, the response of the lead glass at zero energy must be zero, and so we may be only approximating some curve which goes through our data points between 5 and 25 GeV. In fact, the 25 GeV data is not used for this least-squares fit for fear that at that high an energy some of the electromagnetic shower particles will escape out the back of the block. Indeed, the 25 GeV point is too low. One possible explanation of this behavior is the effect of the internal transmittance of the lead glass. A simple model of this effect is given by using a value for the distance of maximum shower energy into the lead glass block as found in electromagnetic shower Monte Carlo studies (Longo 1975):

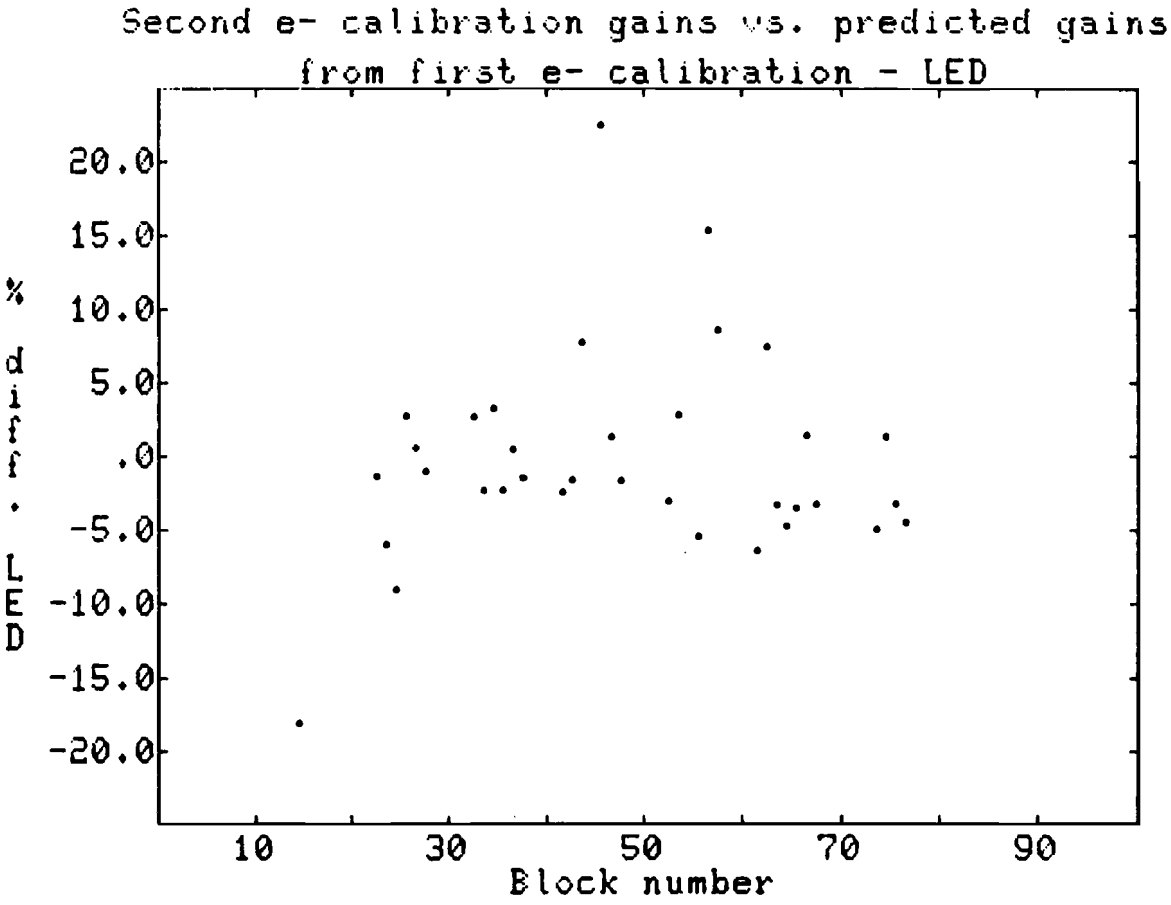

Figure 4-9

Percentage difference between LED calibration corrected gains and second electron calibration gains

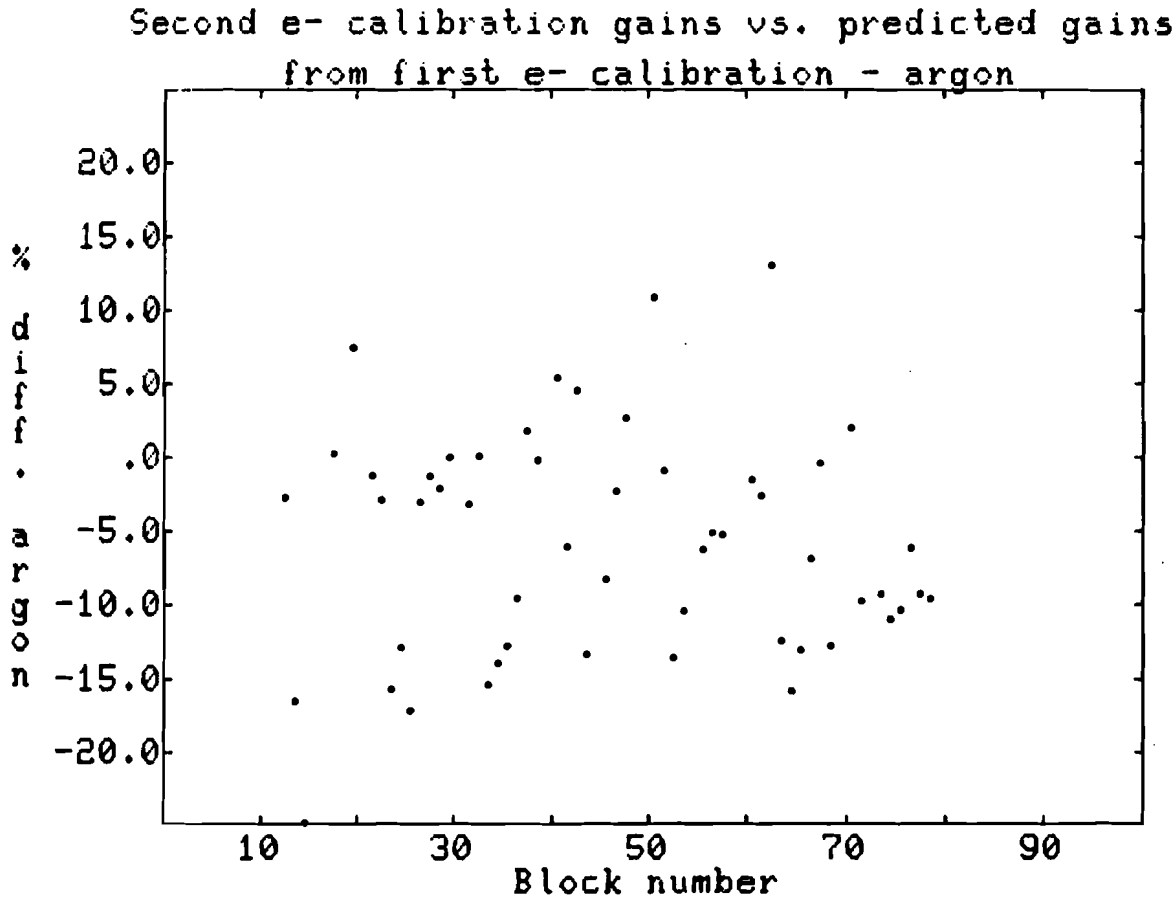

Figure 4-10

Percentage difference between argon flash lamp calibration corrected gains and second electron calibration gains

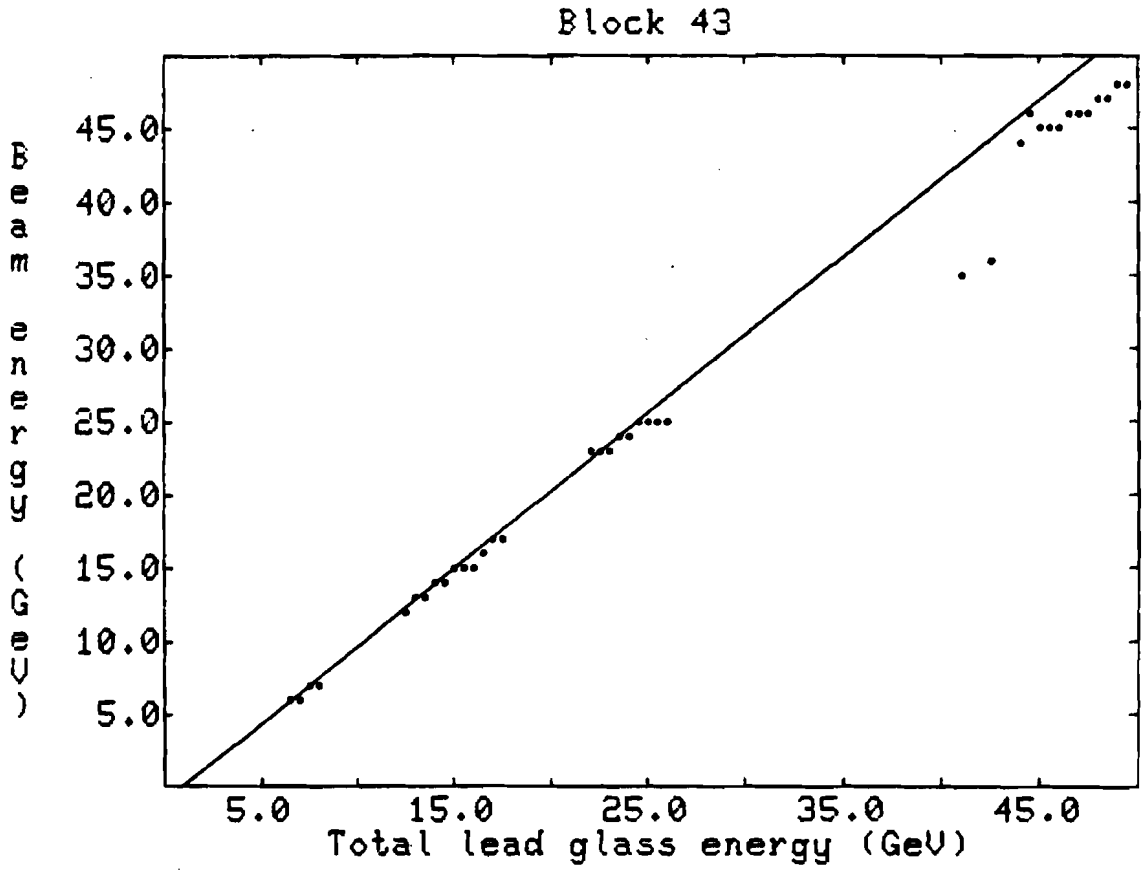

Figure 4-11

Least-squares fit of lead glass energy versus pulse height

$$z = 1.16[\ln(E/E_0)-0.62]X_0 \quad E_0 = 0.0134 \text{ GeV}$$

where X_0 is a radiation length in the lead glass. Now let us make the gross assumption that all the Cerenkov light of the shower is emitted at this point. If the length of the block is L, then the pulse height will be proportional to:

$$\begin{aligned} E \times \exp[-(L-z)/\tau] &= E \times \exp(-L/\tau) \times \exp(z/\tau) \\ &= C \times E \times (E/E_0)^{1.16X_0/\tau} \\ &= C' \times E^{(1+\alpha)} \end{aligned}$$

where C and C' are constants and τ is a transmittance length. Thus, in this case, pulse height would be a power law of energy with the power slightly greater than one. A realistic model would have to take into account the facts that the Cerenkov light is produced throughout the entire shower and that the internal transmittance is a function of wavelength, as is the Cerenkov light distribution and the phototube response. In fact, a Monte Carlo simulation of electromagnetic showers in lead glass taking these factors into account has been done and non-linear energy response is seen (Hanin 1978). However, a fit to the data of this functional form is no better than the straight line with an offset. Another way to investigate the non-linearity of the energy response is to look at the π^0 distribution in different energy bands, but I will postpone that discussion until the next section.

The internal transmittance of the lead glass certainly did affect the light output of the transverse lead glass. The effect is accentuated in this case because the shower is moving through the short dimension of the block. Figure 4-12 shows transverse lead glass energy averaged in each bin where the block's gain has been fixed for one of the longitudinal blocks behind the transverse block. The fit shown contains a factor for the attenuation of light through the glass and another factor for reflection of light from the surface opposite the phototube. As can been seen the fit breaks down at the ends of the transverse block where the shower is either entering the lead glass cookie or entering the end opposite the phototube. This correction factor was used in the energy calculation in the gamma finder. Again, sufficient data was only available across a single block, and so the same attenuation factor was used for every transverse block.

There was also a loss of energy associated with being near the "crack" between two longitudinal blocks. Presumably, energy is absorbed in the material between the blocks. In the electron data, this effect was seen very clearly (Figure 4-13). The fraction of energy lost could be parameterized as a function of the distance of the shower centroid from the crack, but it was found to fit even better as a function of the fraction of the total energy contained in the blocks on the other side of the crack from where the shower

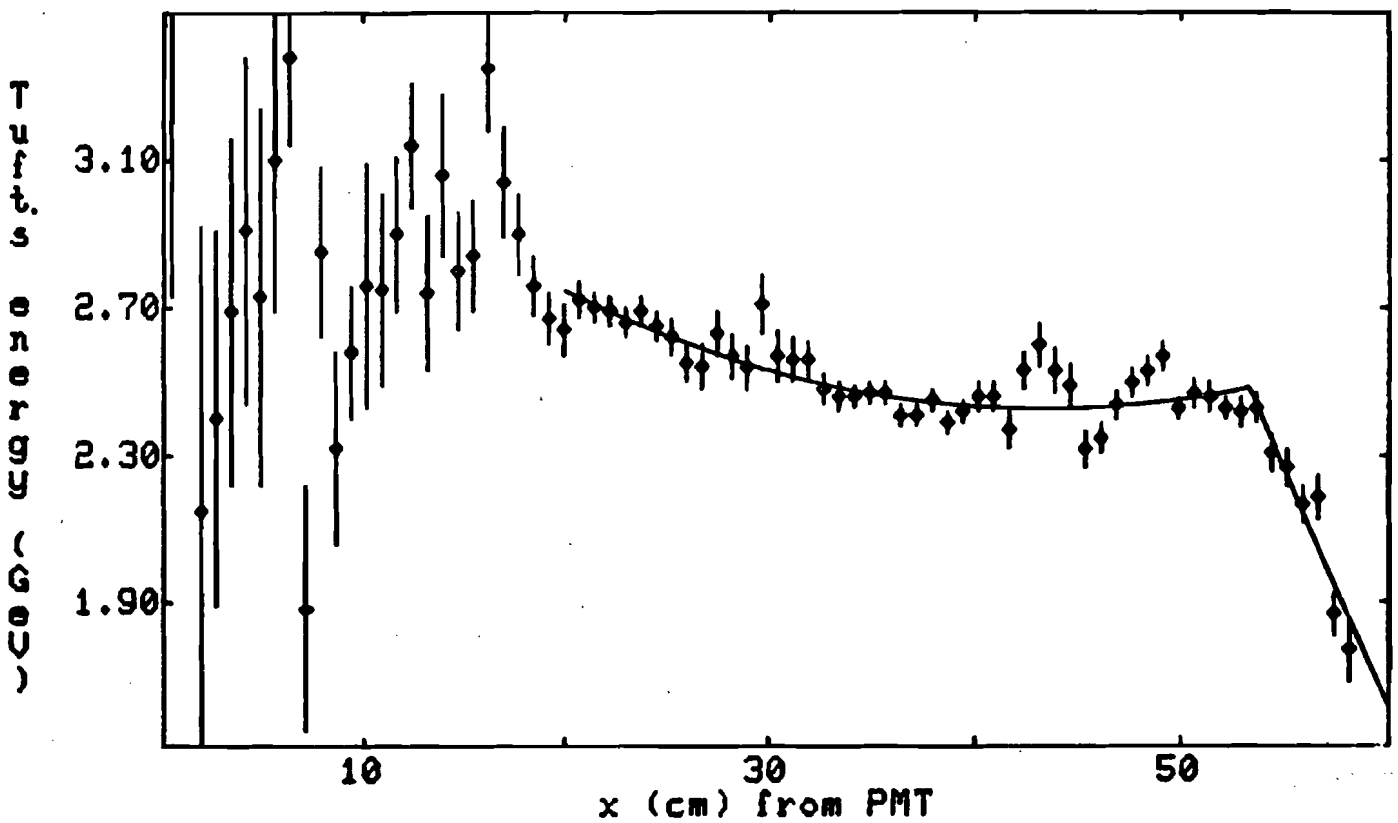

Figure 4-12

Energy attenuation in a transverse lead glass block

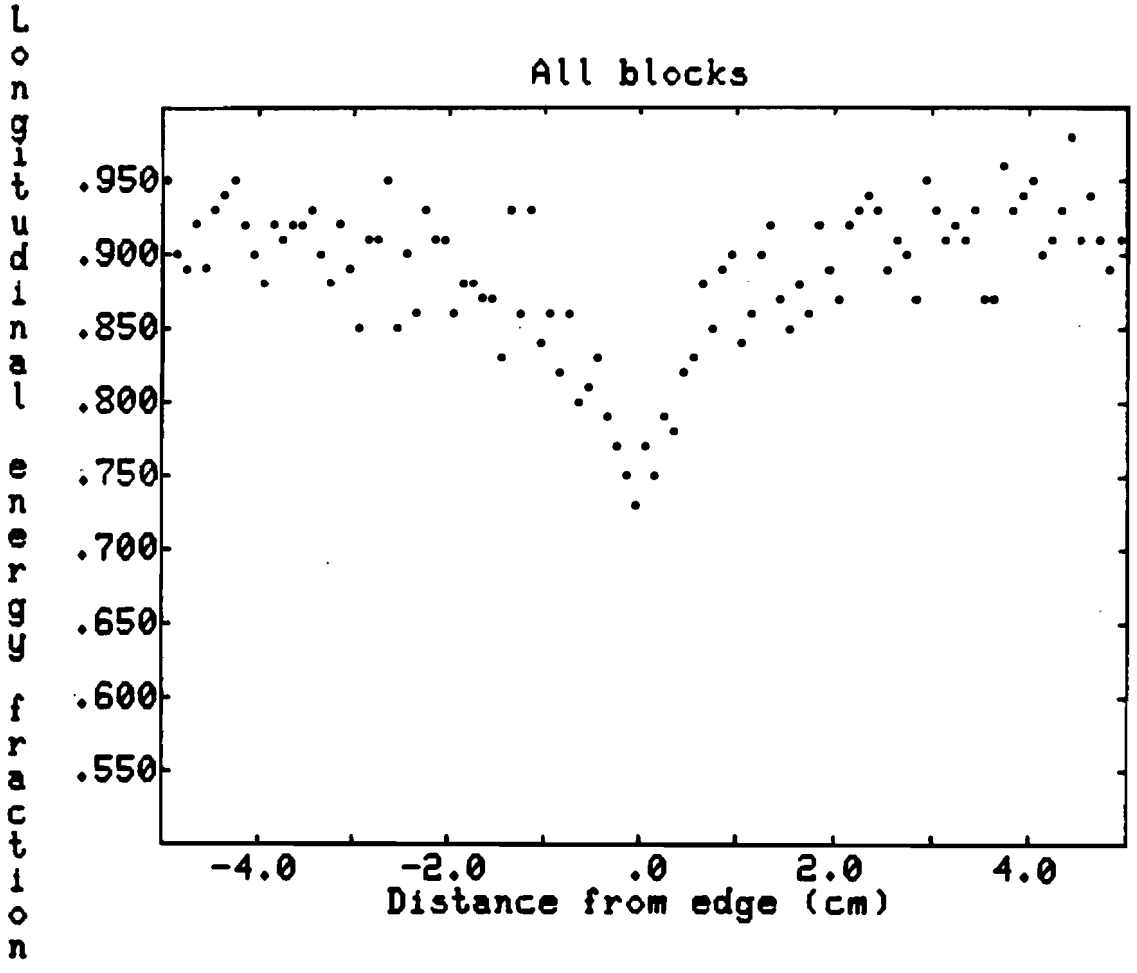

Figure 4-13

Energy loss in a longitudinal lead glass block as a function of distance from the edge for electron calibration data

centroid was. However, when these corrections were applied to showers during normal running restricted to a narrow energy band, no clear benefit was seen, and sometimes the correction appeared to be too large (Figure 4-14). Thus, this correction was not used for normal data running.

4.4 Reconstruction of Neutral Pions

After showers were found in the lead glass array and their four-momentum calculated, it was a simple matter to combine two showers' four-momenta to find the invariant mass of the pair. Our best distribution of such "digamma" masses over the entire data sample is shown in Figure 4-15, with a peak at 135 MeV with FWHM of 20 MeV. However, this distribution was only obtained after recalculating the gains on the basis of the π^0 peak itself. As we have seen, the gains were not tracked very well by the calibration systems. Furthermore, the scarcity of data on some blocks even during the electron calibrations meant these blocks were never well calibrated. Another illustration of this problem is that the π^0 peak found just after the first electron calibration or in a nearby run to the second electron calibration are narrower than the peak found in runs midway between the two calibrations.

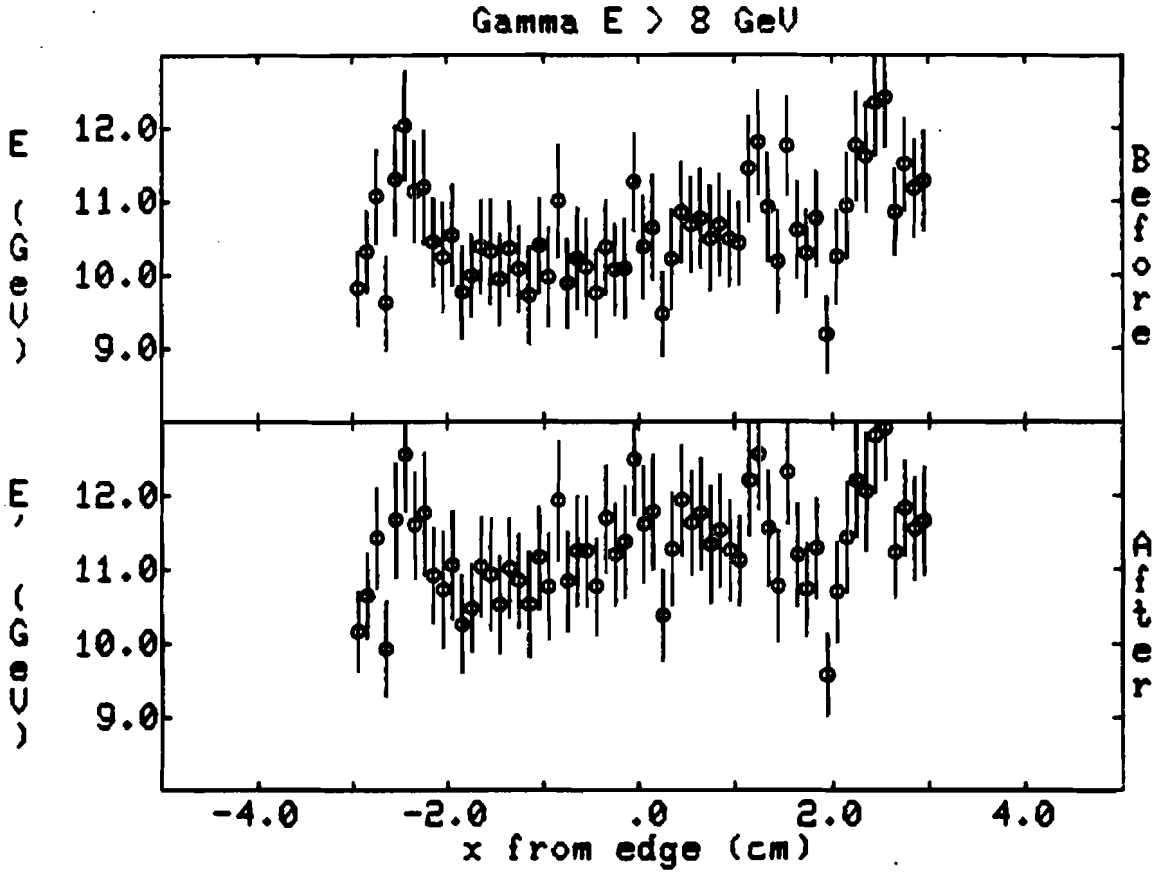

Figure 4-14

Average binwise lead glass energy before and after longitudinal lead glass edge correction for dimuon data

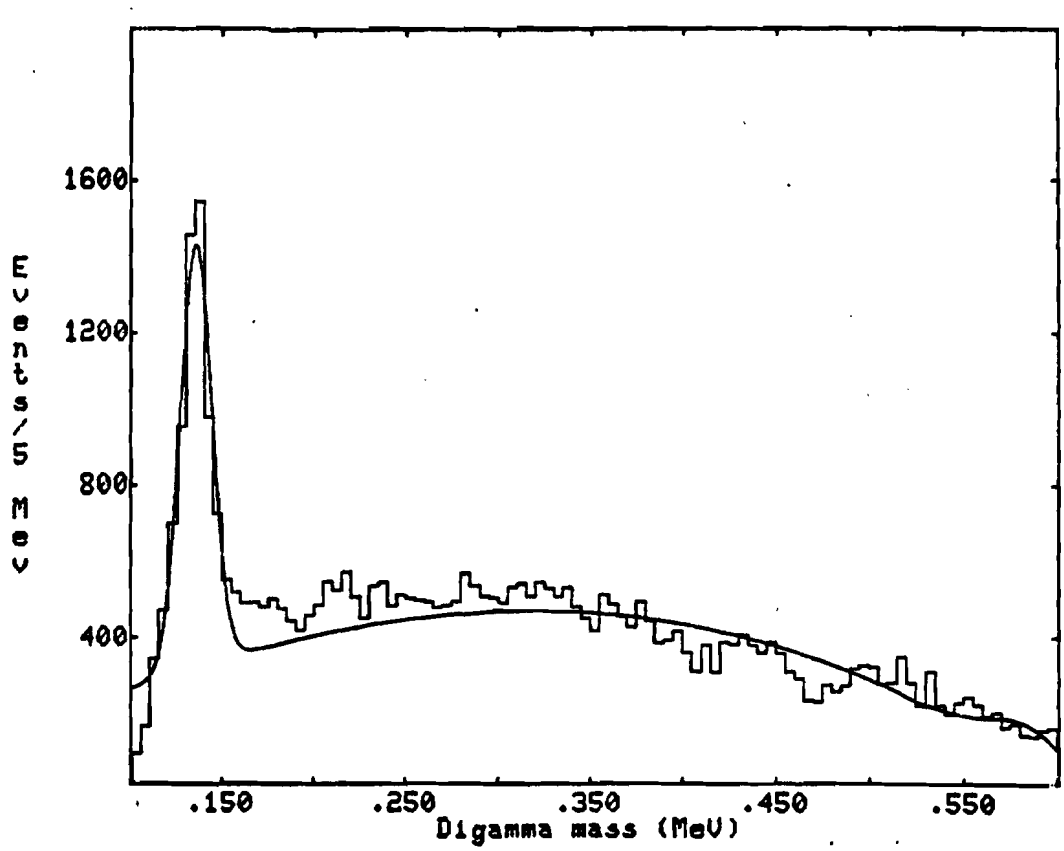

Figure 4-15

Two shower invariant mass distribution over entire data sample after recalibration

The non-linear energy response of the shower detector could be seen even right after the first electron calibration when calibration errors should have been smallest. Figure 4-16 plots the invariant mass and FWHM of two-gamma pairs split up into bands of similar momentum versus the momentum. Since the number of events where both photons fell in a band of energy was restricted, the data sample for these plot consists of about 5 tapes or 110,000 events. As can be seen, as the energies of the photons increases, so does the invariant mass of the calculated π^o. As will be shown in the next chapter, the photons associated with the χ mesons have large momenta. Thus, we restricted the energies of the photons used to the range 5 to 30 GeV, so as to use the most linear region of the energy response curve. All the following discussion is taken with this restriction on the shower energy.

A data base of all lead glass array information for all events with 2 to 6 gammas detected was stored after passing through the entire data sample. For each run, an estimate of the number of π^os and the width and peak value of the π^o was found using a fit of a Guassian plus a quartic background curve. Figure 4-17 shows the original π^o peak for all such showers with energies between 5 and 30 GeV, with a mass of 141 MeV with a FWHM of 33.9 MeV. The only correction to the calibration was to adjust the gain by the ratio of the argon flash signals as explained in the previous section. Figure

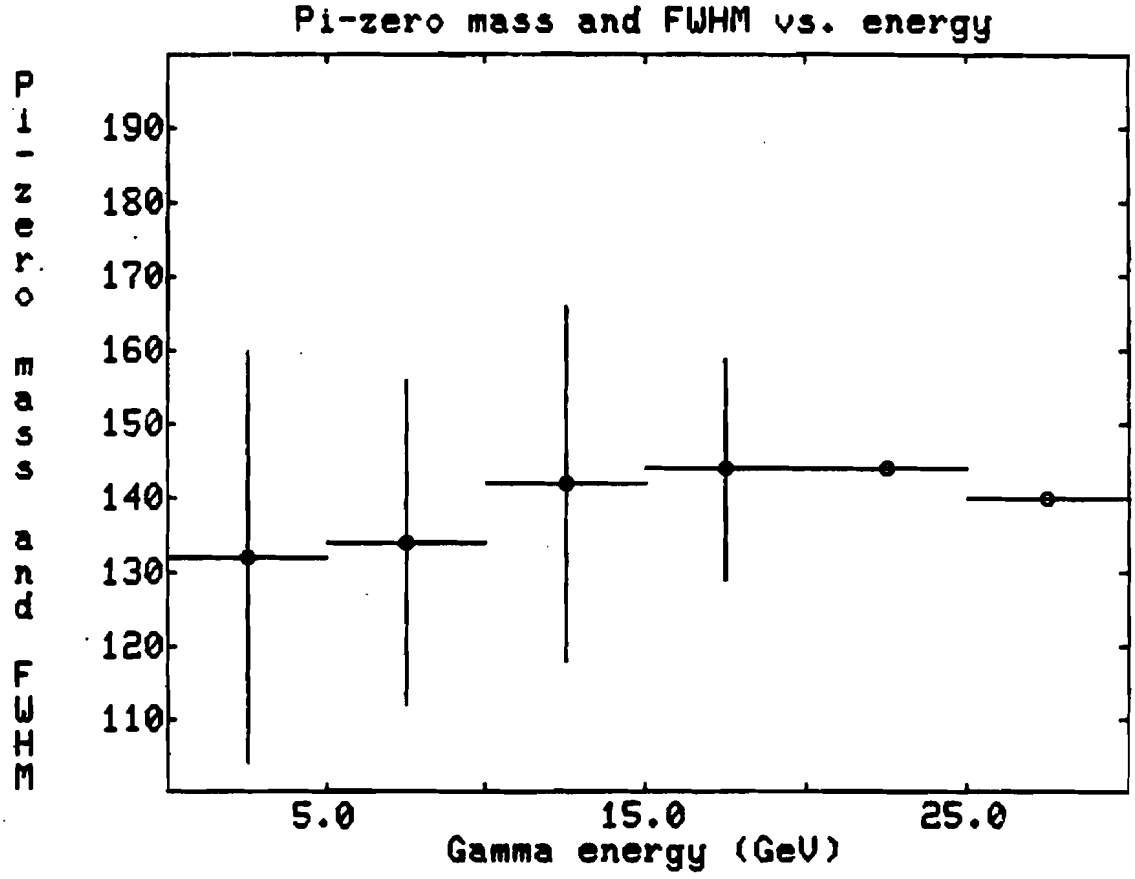

Figure 4-16

Two shower invariant mass and FWHM versus

shower momentum (for both showers)

(FWHM indicated by vertical error bar)

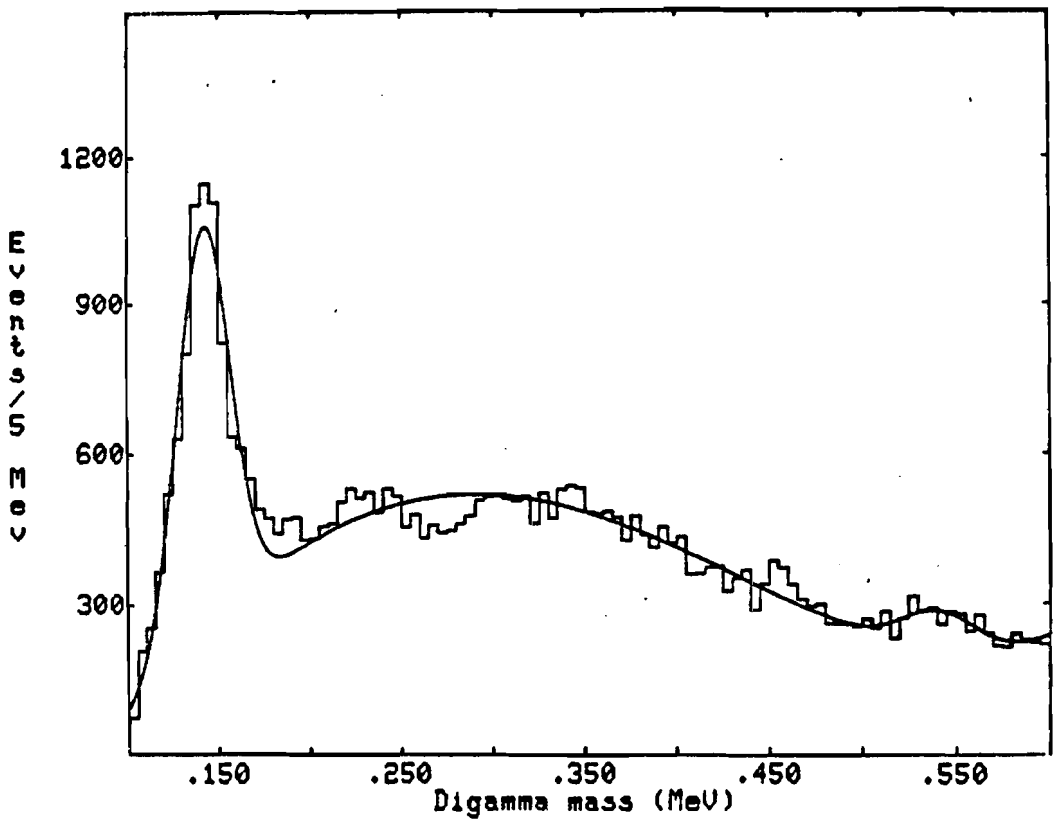

Figure 4-17

Two shower invariant mass distribution over

entire data sample before recalibration

4-18 shows the run-by-run variation in the mass of the calculated π^0; the error bars represent a measure of the statistical error of the mean—i.e., the FWHM of the peak divided by the square root of the number of events in the peak. The apparent π^0 mass varies from 120 to 140 MeV, and the FWHM of the peak generally was about 30 MeV, although it became broader as the blocks became more yellowed (Figure 4-19). If we could adjust all the π^0 peaks to the correct mass, we could lower the overall width of the π^0 peak. Actually, our course was more ambitious than this. Instead, we changed the gains of each block such that the π^0 peak formed of all shower pairs where one of the showers was in that block was at the correct π^0 mass. Since the invariant mass of a digamma pair is just $M^2 = 2E_1E_2(1 - \cos\theta)$ and the angle between the two photons remains the same before and after the gain change, we find that the ratio of the new gain to the old gain, which is just the ratio of the new energy for this photon to the old energy, goes as the square of the ratio of the correct π^0 mass to the apparent π^0 mass. This does not take into account that all the other gains will also change during this procedure. To take account of that fact, only a fraction of the total gain change:

$$\Delta G = G' - G = G[(M'/M)^2 - 1]$$

was applied. The procedure was than reiterated several times, each time changing the gain of every longitudinal block. With sufficient statistics, the procedure was found to converge within three

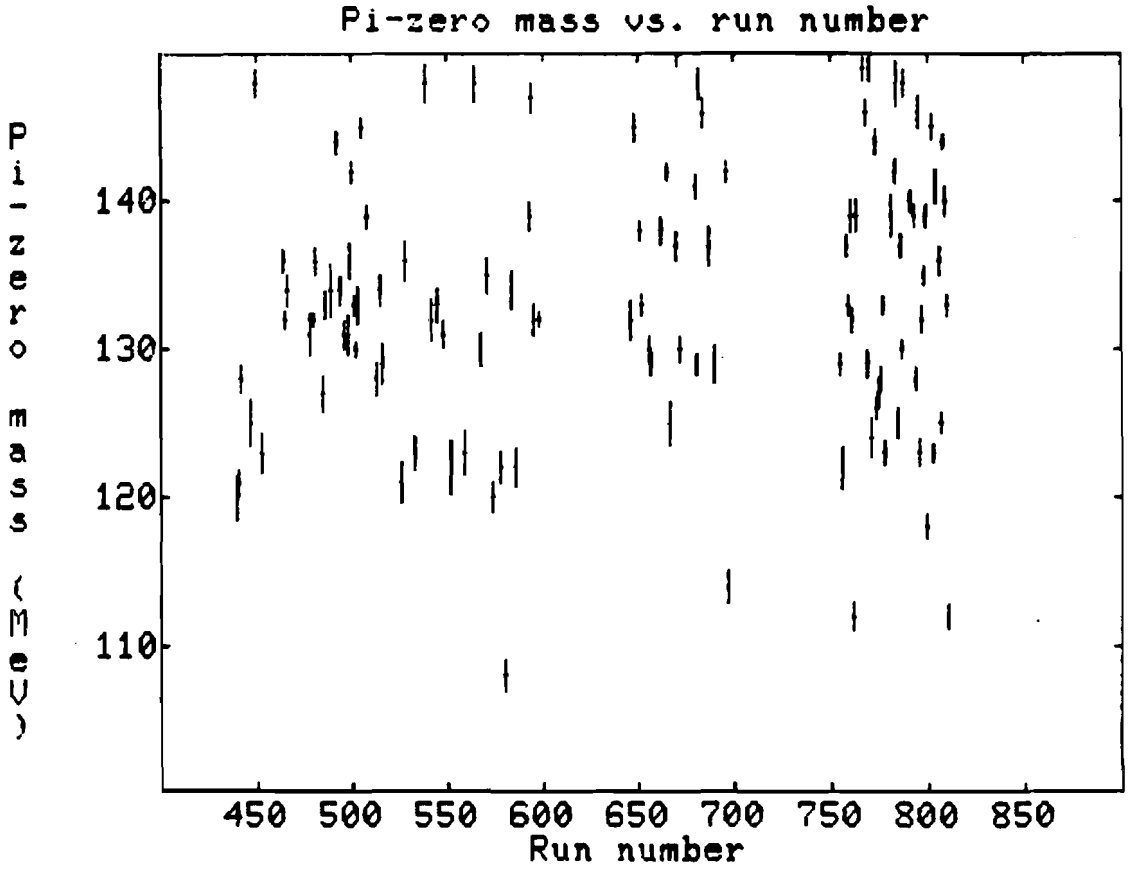

Figure 4-18

Apparent π^0 peak value versus run number

before recalibration

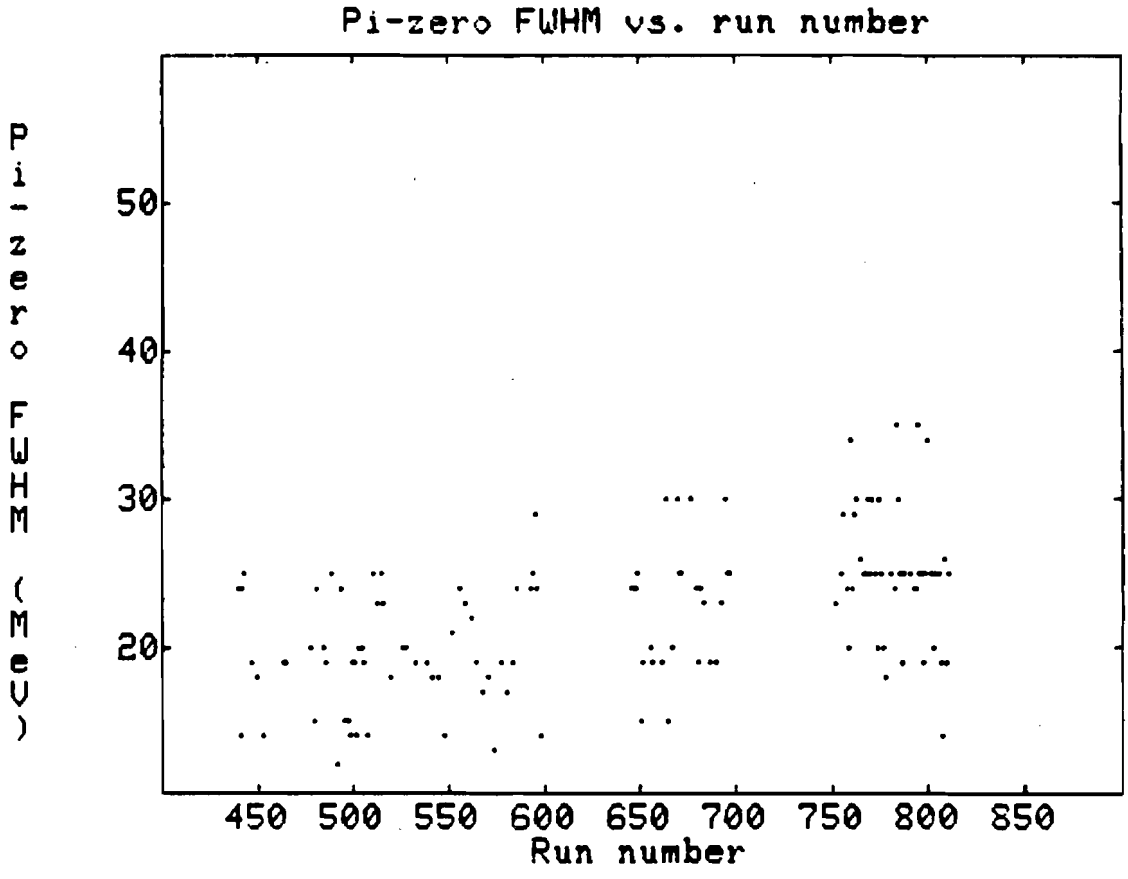

Figure 4-19

FWHM of apparent π^0 versus run number

before recalibration

iterations if the fraction of gain change applied was 0.7 for the first iteration, 0.8 for the second, and 0.9 for the third. A fourth iteration at this point was found to make no more than a 0.2% difference in the apparent π^o mass with the fraction of gain change at 1.0.

The most painful part of this exercise was getting sufficient statistics in each block to permit a successful gain change. Originally, the gains were changed on a run-by-run basis, and a minimum of 20 π^os in a single block after a quick background subtraction of a flat background in the region 110 to 150 MeV divided into 5 MeV bins was used. The result of this set of gain changes is shown in Figure 4-20 in the same kind of plot as Figure 4-17. Two problems became evident while looking at the π^o peaks in individual blocks: first, 20 events was often not sufficient to seperate the signal from the background, and, second, almost none of the Lederman blocks had even enough events to meet this loose cut. Instead, we decided to bite the bullet and simply say that we did not believe the gains of the blocks varied quickly even over the course of several runs. Then we divided the experiment up into blocks of data with no major differences occurring during the runs in that block of data; these blocks generally consisted of about 10 tapes or 270,000 events. With these increased statistics, we changed the gain changing procedure to demand at least 50 events signal above background, and to

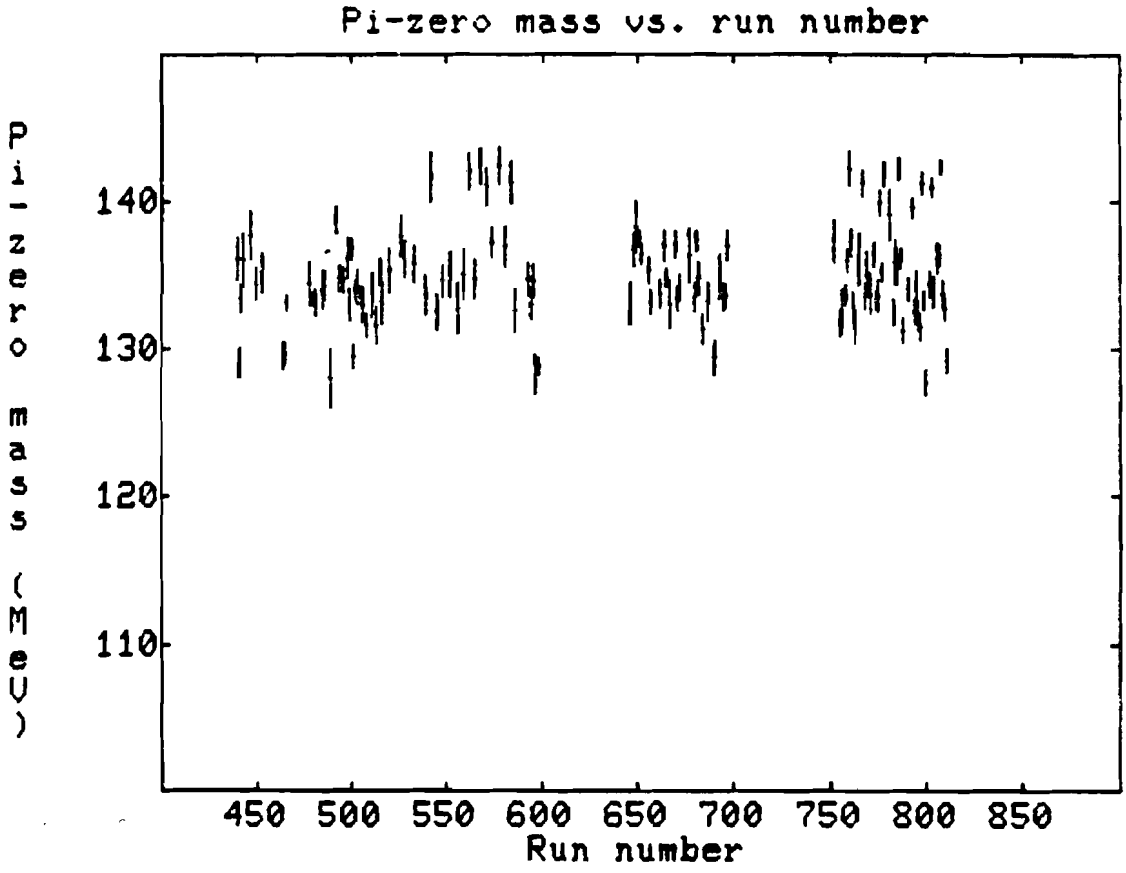

Figure 4-20

Apparent π^0 peak versus run number

after recalibration on a run-by-run basis

search for the single block π^0 peak in 2 MeV bins. The result of this calculation is shown in Figure 4-21. Finally, a final small correction was made to all the gains so as to give exactly the correct π^0 mass.

The result is shown in Figure 4-15 for all events and Figure 4-22 for two shower events only, in which case the FWHM of the π^0 peak is 22 MeV. One other indication that this procedure was successful was locating the η in the digamma spectrum. The two shower multiplicity cut allows us to see a clear η signal, with a mass of 546 MeV and FWHM of 50 MeV.

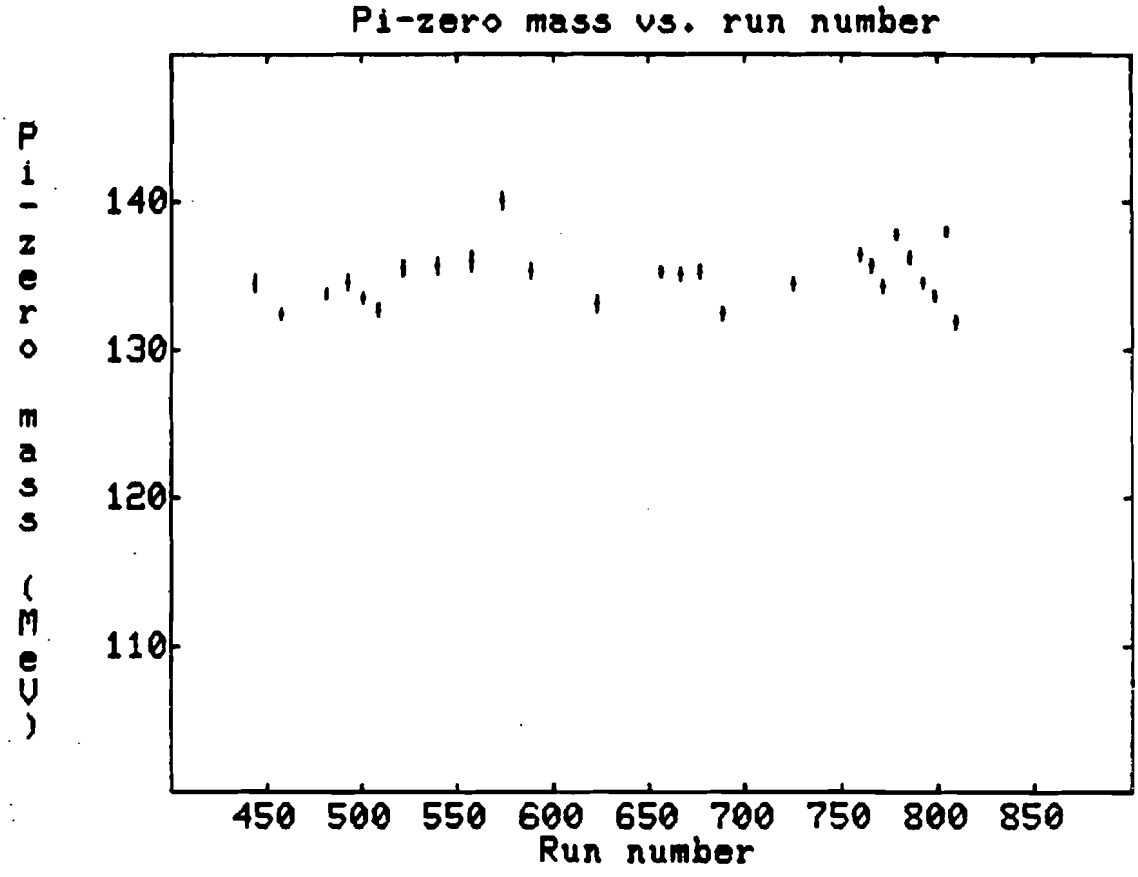

Figure 4-21

Apparent π^0 peak versus run number

after recalibration on a batched run basis

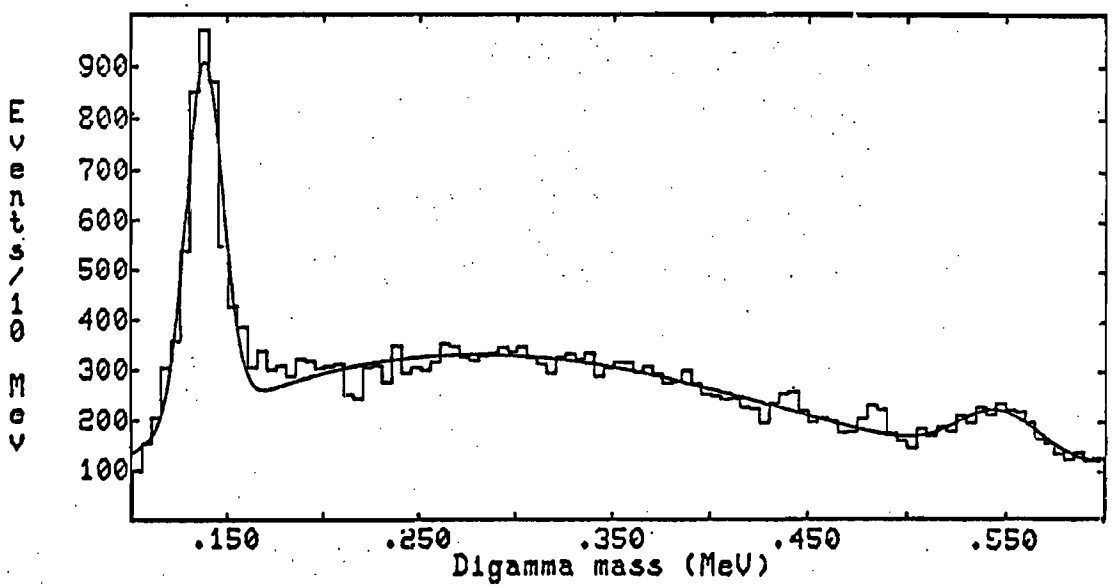

Figure 4-22

Two shower invariant mass spectrum after recalibration

with only two shower events

CHAPTER FIVE

FINAL DATA ANALYSIS

5.1 Final Data Cuts

The dimuon sample with which this analysis is concerned was reduced to a smaller sample of events which contained good dimuon pairs as determined by finding well-defined tracks which passed through the 80 cm and magnet chambers. The predicted projection of these tracks then had to pass through two M hodoscope hits which corresponded to a dimuon trigger. If drift chamber points were present, they were used to tighten up the downstream projection of the tracks. Actually, this procedure was performed twice; once during the spring and summer of 1981 and again in the winter of 1982. From this point on, these two sets of data reductions shall be referred to as the "first pass" and the "second pass".

The results of these passes through the dimuon data set were sets of tapes containing either the larger set of all confirmed dimuon events or the smaller set of tapes containing dimuon pairs with a large mass. At the same time as the events were written to tape, all tracks in the events were analyzed. This made it possible to write data summary tapes containing "data format" information and "tertiary format" information. The "data format" consisted of slightly more

compact data where pedestals were subtracted from ADC signals and the chamber information was contained in the form of coordinates as opposed to wire numbers. The "tertiary format" data consisted of completely analyzed events where tracks were associated with hits in the chambers and given a momentum vector. The form of the track finder used at this point was primitive to keep the computer time per event down, but was sufficient to identify muons and assign a crude dimuon pair invariant mass. For example, the second pass track finder included the drift chamber vernier but not the track fitting or use of the magnetic field map (as explained in Chapter 4). The much smaller sample of high-mass dimuon pairs could then be recalculated using a more sophisticated track finder.

Thus, the dimuon four-momenta could be calculated assuming both particles to actually be muons; then a mass could be derived and the J/ψ searched for. The "data format" information for the lead glass array could then be analyzed with the gamma-finding algorithm. The photons associated with the J/ψ events could then be combined with the J/ψ particles to obtain a $J/\psi-\gamma$ mass spectrum and used to search for the χ states of the charmonium spectrum.

Figure 5-1 through 5-3 show the J/ψ peak after more sophisticated track finding. Figure 5-1 is the events found after the first pass with the old track finder and only using the drift chamber

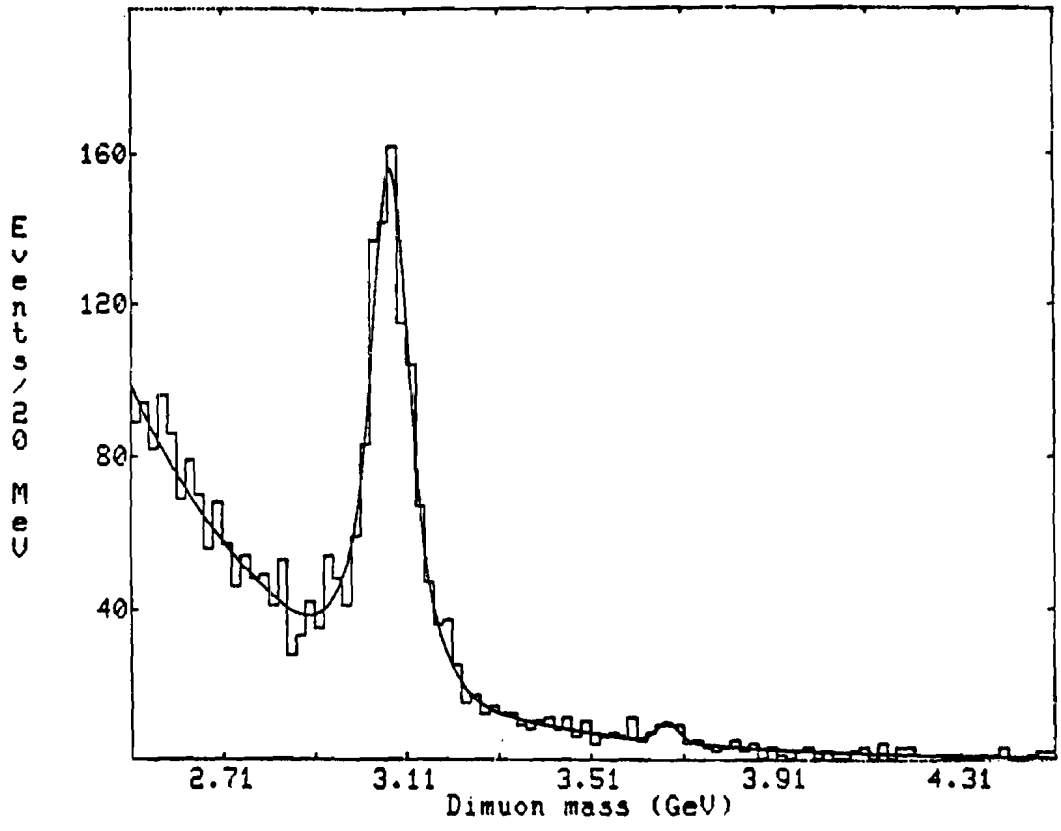

Figure 5-1

Dimuon mass distribution after first pass

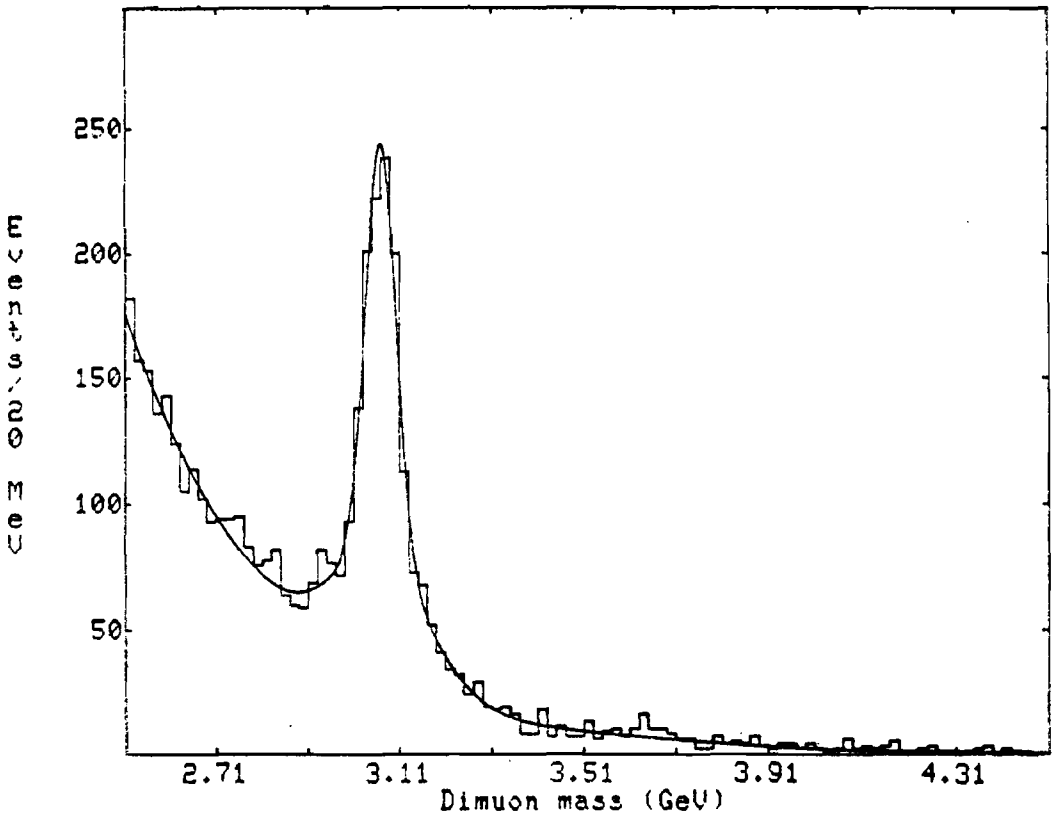

Figure 5-2

Dimuon mass distribution after second pass

using global fit but not swimming each track

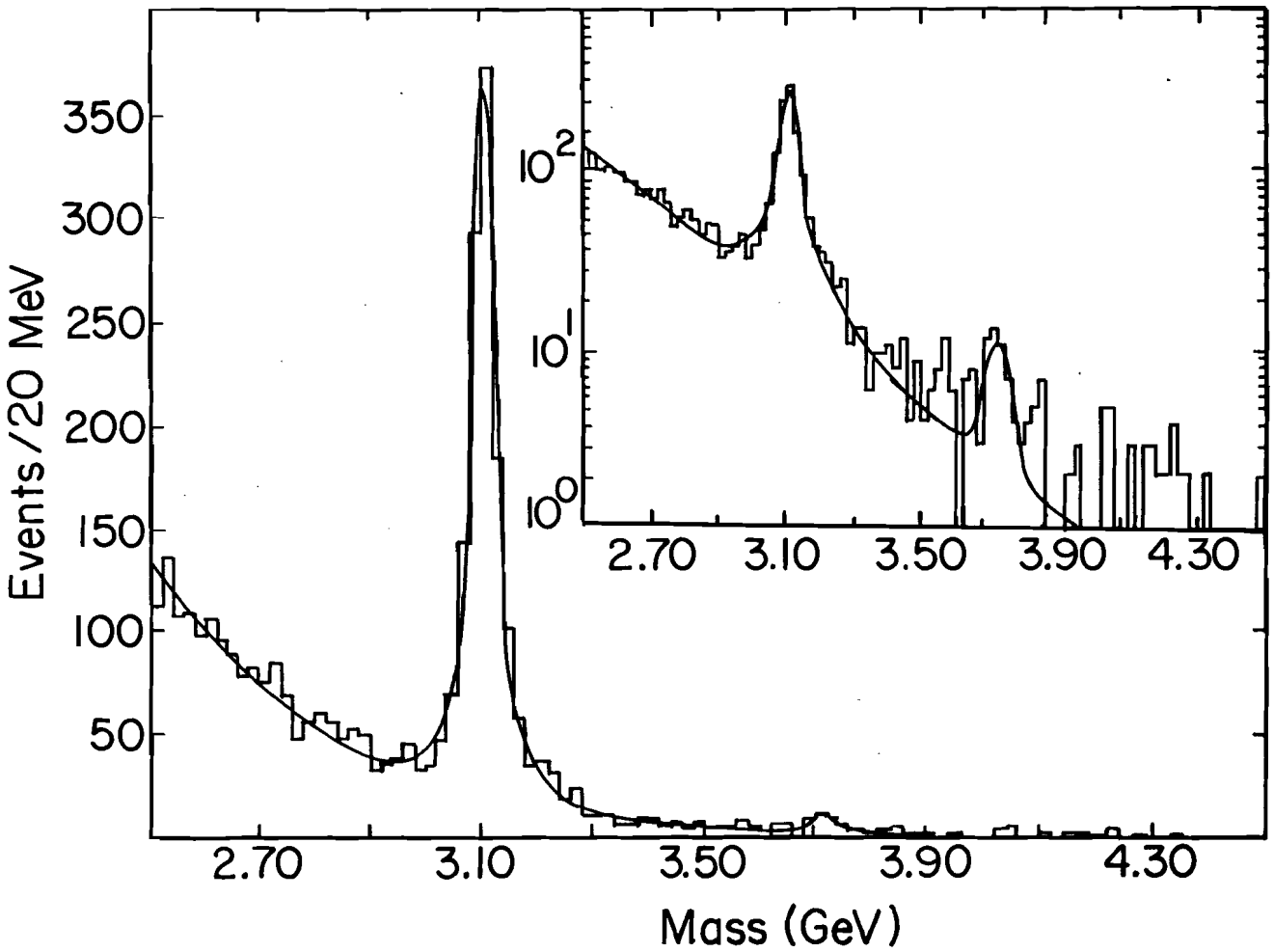

Figure 5-3

Dimuon mass distribution after second pass

using global fit and swimming each track

vernier. The J/ψ peak occurs at 3075 MeV with 819 events above background and a FWHM of 80 MeV (the smaller of two FWHM as explained shortly). Figure 5-2 is the dimuon mass distribution after the second pass (using multiple standard tracks) and including the drift chamber vernier and the global fit to each track without swimming every track through the CCM. The J/ψ peak occurs at 3069 MeV with 1300 events above background and a FWHM of 78 MeV. Finally, Figure 5-3 is the result of swimming every track through the magnet. The peak has been adjusted to the correct J/ψ mass and contains 1264 events above background with a FWHM of 50 MeV. The inset to Figure 5-3 shows a semi-logarithmic plot of the same distribution, which aids one in seeing the small but statistically significant $\psi(3685)$ peak. The J/ψ is fit with two Gaussians at the same mass but with two different widths; the $\psi(3685)$ is fit with a single Gaussian and the background is a falling exponential. The explanation of this fit shall be postponed until section 5.2. The point is that the swimming of the tracks through the magnet does more to improve the resolution of the dimuon spectrum even than using the drift chambers.

Many cuts were tried to enhance the χ meson peak in the $J/\psi-\gamma$ spectrum. Here, I shall only describe the final set of cuts. Originally, the procedure was more complicated than the version described here because the high-mass dimuon sample was divided into two samples: all events and events with one or more drift chamber

hits. However, as we have seen above, the track fitting with the magnetic field is more significant than whether a track has associated drift chamber hits or not, and so the sample is no longer divided in this fashion.

Some cuts consisted of weeding criteria for throwing out tracks which were not real. The associated upstream track must have at least 2 80 cm x plane hits and 5 80 cm and UI chamber y plane hits. There must be at least one matched hit in UI3, UI4, or UI5. A "track efficiency" is defined for each track as the total number of hits in the two tilted 80 cm planes considered as one plane (i.e., or'ed together) plus the number of hits in the UI chamber u- and v-planes divided by the total possible number of hits for the track. This efficiency must be greater than or equal to 80% if there are no drift chamber hits and greater than or equal to 70% if there are drift chamber hits.

Other cuts were directed at the general topology of the event. Among these cuts were the lower and upper limits of the dimuon masses to be considered as J/ψs. This cut was a compromise between making the background as small as possible and having as many J/ψs as we could to look for χ mesons. The range used was 3.05 to 3.15 GeV. In this range the signal-to-noise was 20:1. Dimuon masses to be used in the creation of the $J/\psi - \gamma$ background plots were split into two

control regions, one below and one above the J/ψ signal region, in the intervals 2.90 - 3.00 GeV and 3.20 - 3.30 GeV. The lower and upper limits on shower energies in the shower detector applied to creation of pizeros or $J/\psi - \gamma$ signal or background. As throughout this thesis, the range used was 5 to 30 GeV, as explained in section 5.3. Lower and upper limits were set on the mass of digamma events whose showers were thrown out of consideration for use in $J/\psi - \gamma$ signal or background histograms because they could have been produced in π^0 decay. This excluded range was 110 MeV to 160 MeV. A routine double-checked that the D/S tracks which were identified as muons actually intersected a latched M counter. When these events were written to the input file used by this job, muons were identified with tracks which when projected into the plane of the M hodoscope were found to be within a "window" around a latched M counter. However, the "window" used here is smaller than that used to create the input file, so some events are no longer accepted. The extent of the "window" was (1.0 + 20.0/p) cm wider than the hodoscope element to take into account multiple scattering (p is the total momentum of the particle in GeV/c); during the filtering for the second pass the extent of the "window" was 7.1 cm wider in x and 3.6 cm wider in y. α is the asymmetry of the muon momenta; if the value of $\alpha = (p_1 - p_2)/(p_1 + p_2)$, where p_1 is the total laboratory momentum of the positive muon and p_2 is the total laboratory momentum of the

negative muon, is greater than -0.70, then the dimuon pair is accepted. This served to throw out events where a high momentum punch-through hadron, which was usually negative, triggered the M hodoscope, and reduced the background. A minimum distance was allowed between a shower's centroid and the location of a D/S track projected onto the face of the longitudinal lead glass blocks. Due to the broad radial distribution of hadron showers, this distance was fairly large--10.0 cm. This cut should avoid confusion caused by hadrons showering or depositing their minimum ionization energy in the lead glass. A cut was also imposed on the quality of the lead glass shower as determined by the gamma-finder. This cut corresponded to accepting those showers where two showers are merged or the Tufts blocks were used in conjunction with the P-tubes to locate showers, but not showers with overlapping blocks or those near the beam hole or edge of the array.

Several different calculated backgrounds were developed and corrected during the course of these runs. For each run, a background region in the dimuon spectrum was selected in addition to the signal region. These dimuons in combination with the showers from the same event provided one background for the $J/\psi-\gamma$ mass plot. If the background was chosen to contain as many events as the signal region than a background subtraction could be sensibly performed. The second type of background was created by storing (n + 1) events, and then,

when all these events are accumulated, combining the dimuons from one stored event with the gammas from another. A little thought will reveal that if only events where one dimuon pair or gamma exists are used, a background n times as big as the signal $J/\psi-\gamma$ combinations results. Then subtraction of this background divided by the factor n provides a smooth background to subtract from the signal. The first of these two backgrounds was rejected as not really representative of showers associated with the J/ψ. The second was made more sophisticated as will be explained in the next chapter.

5.2 The J/ψ Signal

In the first pass, approximately 800 J/ψs were found; in the second pass we found almost 1300 without using the magnet map in the track fitter and almost halved the width of the J/ψ peak using the magnet map in the track fitter. Figure 5-1 shows the dimuon spectrum for high masses from the first pass along with appropriate parameters, Figure 5-2 shows the same mass distribution for the second pass without swimming each track through the CCM, and Figure 5-3 shows the same mass distribution for the second pass with the swimming routines. The differences in the techniques used to obtain these two samples are enumerated in Section 4.2. As explained earlier, the last and largest J/ψ sample is obtained by fitting the J/ψ with two Gaussians with the same mass but different widths. As can be seen, this does a much

better fit of the data, with 2/3 of the J/ψs in the narrow peak and 1/3 in the wider peak. This could be viewed as two samples of J/ψs, one where the right hits were picked up for both tracks and one where one or more bad hits were incorporated into the global fit.

Before the J/ψ was combined with the γ, a routine which forced a full 1-C fit on the dimuon pair to the J/ψ mass was applied. It used the muon tracks' fitting data as described in section 4.3. The method of fitting is the general solution to a least-squares fit with non-linear constraint equations as found using Lagrange multipliers (Brandt 1970).

The parameters passed to the routine are the fit U/S track parameters, the fit total momentum, and the corresponding error matrix for each of the two muons. The latter has the form:

$$A_{jk} = \sum_i [(\partial x_i^i/\partial T_j)(\partial x_i^i/\partial T_k)+(\partial y_i^i/\partial T_j)(\partial y_i^i/\partial T_k)]$$

using exactly the same definitions as in Chapter 4. The single constraint equation is that the effective mass of the dimuon pair be that of the J/ψ:

$$f(\vec{T}_1,\vec{T}_2) = (p_1+p_2)^2 - M_\psi^2$$

We fix the two tracks' intercepts because they do not enter directly into the constraint equation and the tracks intersect at the interaction vertex. Then we define a new vector $\vec{T}' = (A_{x_1}, q_1, A_{y_1}, A_{x_2}, q_2, A_{y_2})$ such that $f(\vec{T}_1,\vec{T}_2) = f(\vec{T}')$, with a

corresponding error matrix with elements A'_{jk}.

The new estimates of the parameters $\vec{T}'$ are then given by the general solution:

$$T'_i \leftarrow T'_i - \delta T'_i$$

$$\delta T'_i = \frac{\sum_j [A'_{ij} (\partial f/\partial T'_j) f(\vec{T}')]}{\sum_{k,l} [(\partial f/\partial T'_k) A'_{kl} (\partial f/\partial T'_l)]}$$

These then provide the refit muon 4-momenta and, in turn, the J/ψ 4-momentum. The chi-squared is given by the "minimum function":

$$M = \sum_{j,k} \delta T'_j (A'^{-1})_{jk} \delta T'_k$$

Also, one can reiterate the 1-C fit, although we did not find it to be necessary. Figure 5-4 shows the width of the J/ψ after one interation of refit. Figure 5-5 shows the chi-squared distribution for the same sample. Note that this 1-C fit does not use the downstream x- and y-intercepts in either the parameters or the error matrix. We felt that the proper way to include this information was by adding the interaction vertex to the muon track fit (which in turn determines where the upstream and downstream intercepts are).

5.3 Efficiencies of the Detectors

An understanding of the efficiencies of the apparatus was essential to derive meaningful results from acceptance calculations.

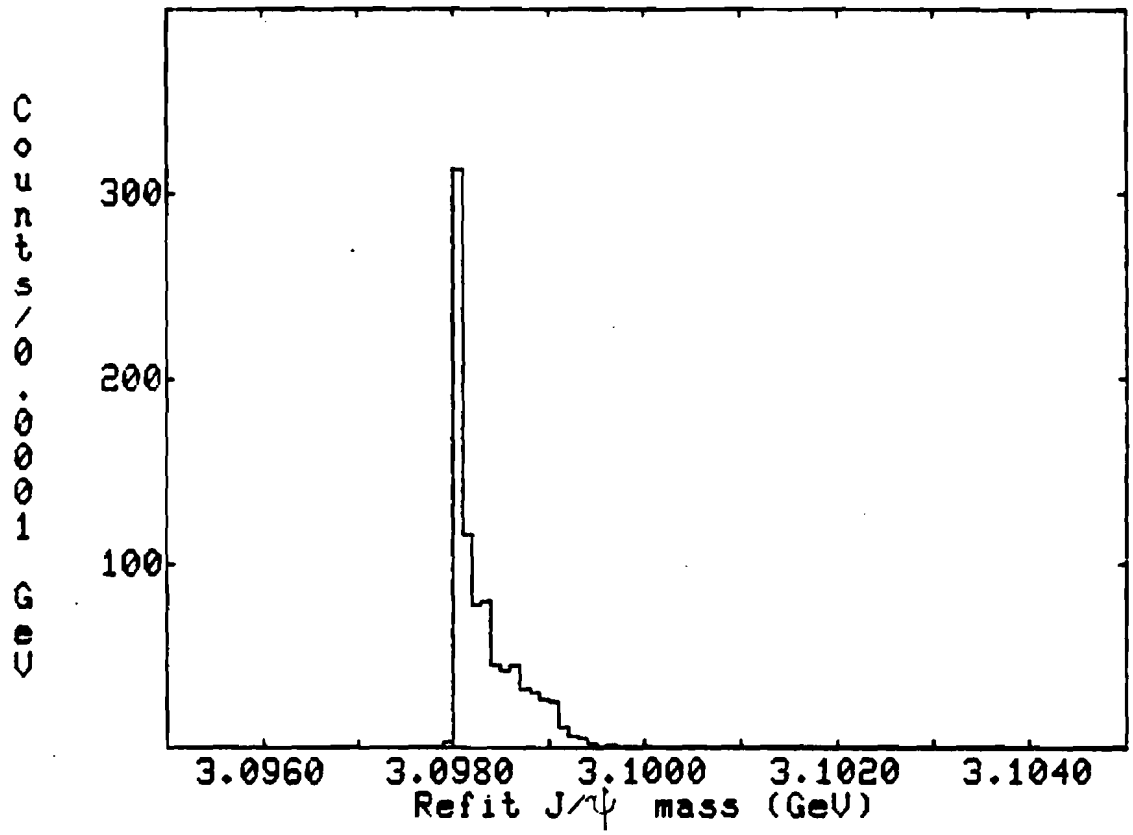

Figure 5-4

Dimuon mass distribution after 1-C fit for events in J/ψ region

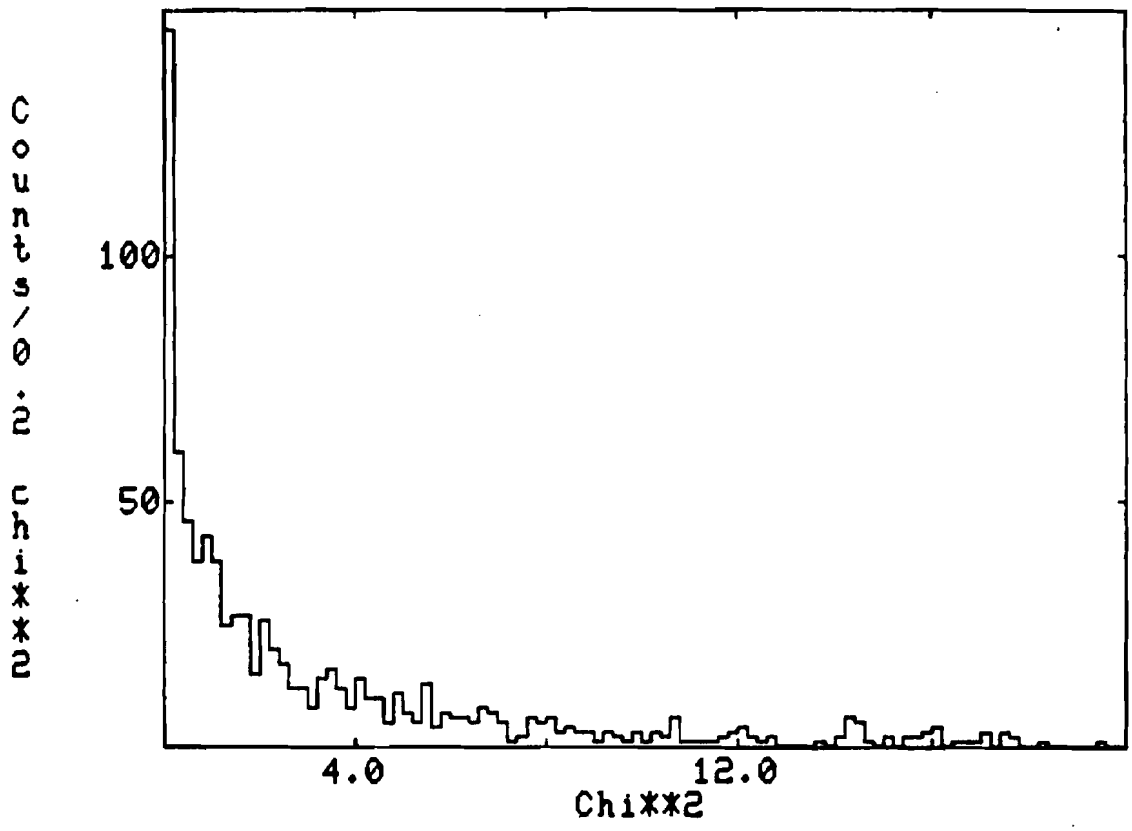

Figure 5-5

Chi-squared distribution for J/ψ events

Thus, the efficiency for finding a hit in a chamber given a track through the chamber and the accuracy with which its position was measured both had to be found and taken into account. Likewise, efficiencies for the hodoscopes had to be determined. The position resolution of the lead glass array for showers amounted to the spatial resolution of the P-tube array; but of equal importance is the energy resolution of the lead glass. The relationship between efficiencies and track topology further complicated the situation. A similar complication occured in the lead glass array for nearby showers.

The efficiencies and position resolution of the MWPC's are discussed in the thesis of H. Budd (Budd 1983), while those of the drift chambers are discussed in the thesis of P. Schoessow (1983). In both cases, straight tracks from UHI runs were used to find well-defined tracks with many hits, and then the resolution and efficiencies were found in each detector plane. The University of Illinois chambers were further divided into three sections because these chambers were found to have a lower efficiency in the middle region due to higher fluxes. The actual chamber efficiencies are tabulated in the thesis of H. Budd, and were used in the calculations in section 5.4.

The efficiency of the shower detector for photons was a more difficult problem to address because there was no independent detector to confirm the presence of the particle. Instead, showers from one set of events with well known shower parameters were implanted into normal dimuon data for the shower detector, and then the gamma finder attempted to retrieve the correct postion and energy of the implanted shower. As a by-product of this process, we can see what changes to the gamma finder result in a better efficiency for finding showers. The well-defined showers used were electrons from electron runs with energies between 10 and 20 GeV, more than 66% of the energy of the shower deposited into one block, and only a single shower in an event to rule out the possibility of bremsstrahlung.

The procedure then used was as follows: evaluate the electron data alone with the gamma-finder, skip further analysis if not only one shower found, save any relevant variables, then analyze the merged dimuon data which has the same electron imbedded in it and compare the results. Table 5-1 tabulates the efficiency of the old (Hossain 1981) gamma finder versus an old version of the current gamma finder and versus the current gamma finder, which contains the following improvements over the older version: 1) correcting for the attenuation in the transverse blocks, 2) allowing a lower minimum energy in a block adjacent to the longitudinal block which contains the centroid of the shower at which the energy in the adjacent block

will be added into the shower, and 3) allowing centroids to be located with only two P-tube planes in those regions of the detector only covered by two P-tube planes. The numbers tabulated are the efficiency percentages of finding the implanted shower within a given energy of the implanted shower's energy (listed on the left) and of finding the implanted shower's location no more than a given distance (0.5 or 1.0 cm, listed on top).

Figures 5-6 and 5-7 show projections of the energy difference vs. shower separation for the merged dimuon shower closest to the electron shower's location. One point to note is the constant energy offset in the energy differences -- this is due to the electrons being added into a dimuon run with a different gain and, thus, a different argon lamp recalibration. Taking the ratio of the argons for the two runs gives an energy offset of (1.000-0.9225)*15 GeV = 1.16 GeV. In this case, the beam was steered into block 33 for this electron run so this is a measure of the efficiency in just this region. A large number of the electron showers merged into the dimuon data were not found: 26% for the old gamma finder, and 23% for the current gamma finder. By looking at individual events and seeing how some showers were not recovered, the merged electron showers also served as a method to test improvements in the gamma finder. Figure 5-8 and 5-9 illustrate the major cause of shower finding inefficiencies--the confusion caused by overlapping of either P-tube clusters or energy in

1) Old gamma finder:

E (GeV)	l (cm)	
	0.0 - 0.5	0.0 - 1.0
1.1-1.2 (±0.05)	121/1056=11.5%	135/1056=12.8%
1.0-1.3 (±0.15)	276/1056=26.1%	313/1056=29.6%
0.9-1.4 (±0.25)	350/1056=33.1%	395/1056=37.4%
0.6-1.6 (±0.50)	473/1056=44.8%	529/1056=50.1%

2) U of I gamma-finder:

E (GeV)	l (cm)	
	0.0 - 0.5	0.0 - 1.0
1.1-1.2 (±0.05)	118/1048=11.3%	151/1048=14.4%
1.0-1.3 (±0.15)	275/1048=26.2%	351/1048=33.5%
0.9-1.4 (±0.25)	348/1048=33.2%	455/1048=43.4%
0.6-1.6 (±0.50)	427/1048=40.7%	574/1048=54.8%

3) Improved U of I gamma finder:

E (GeV)	l (cm)	
	0.0 - 0.5	0.0 - 1.0
1.1-1.2 (±0.05)	152/1043=14.6%	157/1043=15.1%
1.0-1.3 (±0.15)	442/1043=32.9%	359/1043=34.1%
0.9-1.4 (±0.25)	442/1043=42.4%	460/1043=44.1%
0.6-1.6 (±0.50)	544/1043=52.2%	566/1043=54.3%

Table 5-1

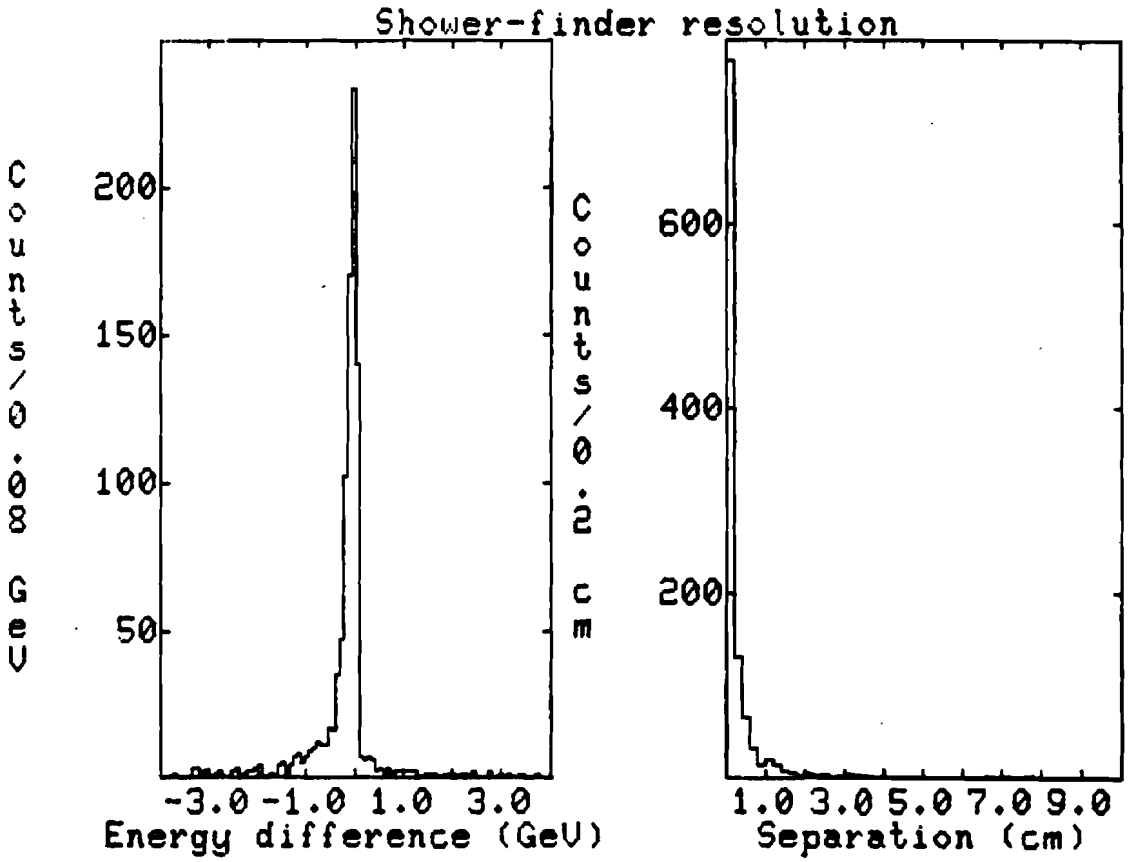

Figure 5-6

Resolution of the gamma finder

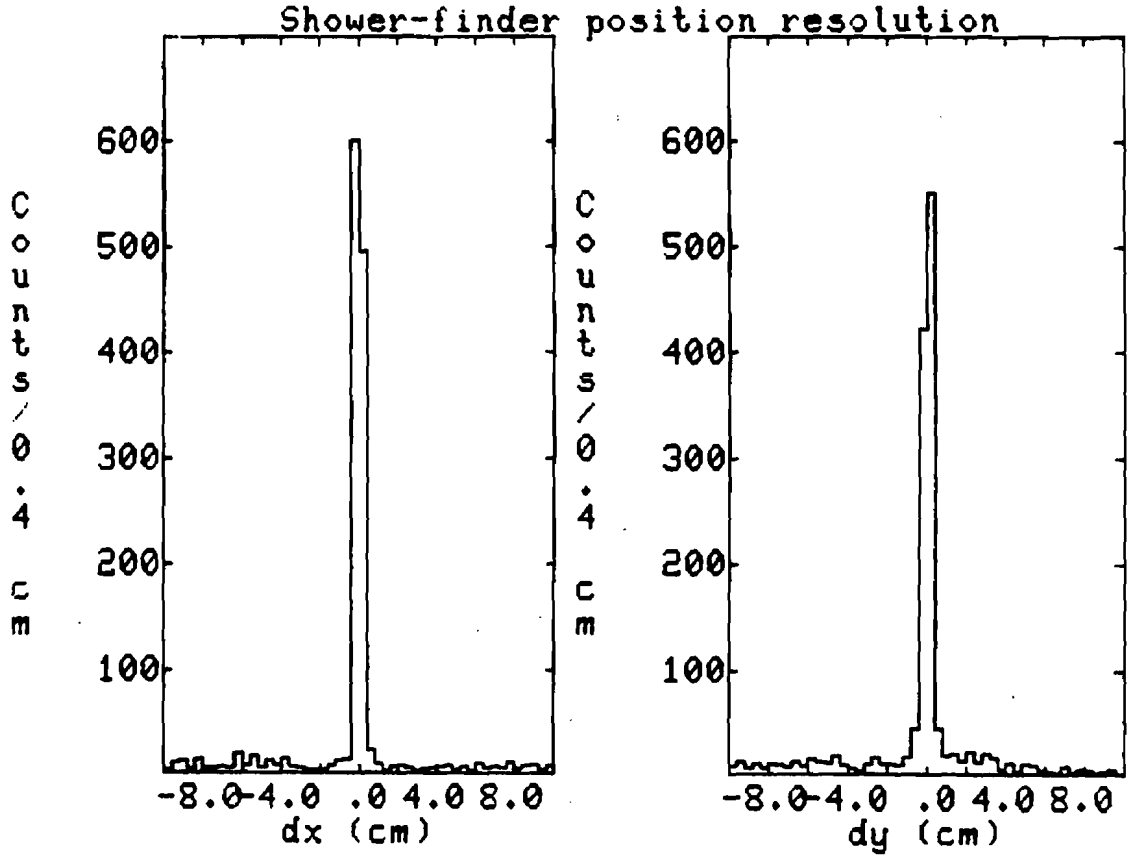

Figure 5-7

Position resolution of the gamma finder

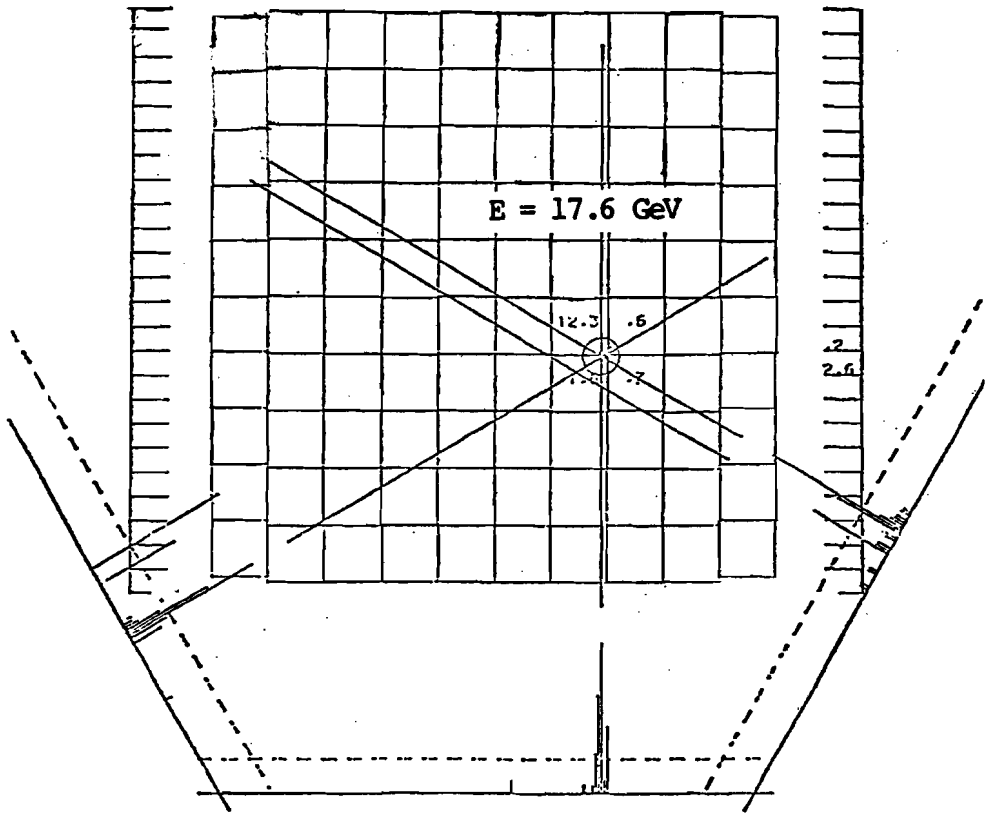

Figure 5-8

An electron calibration event in the lead glass

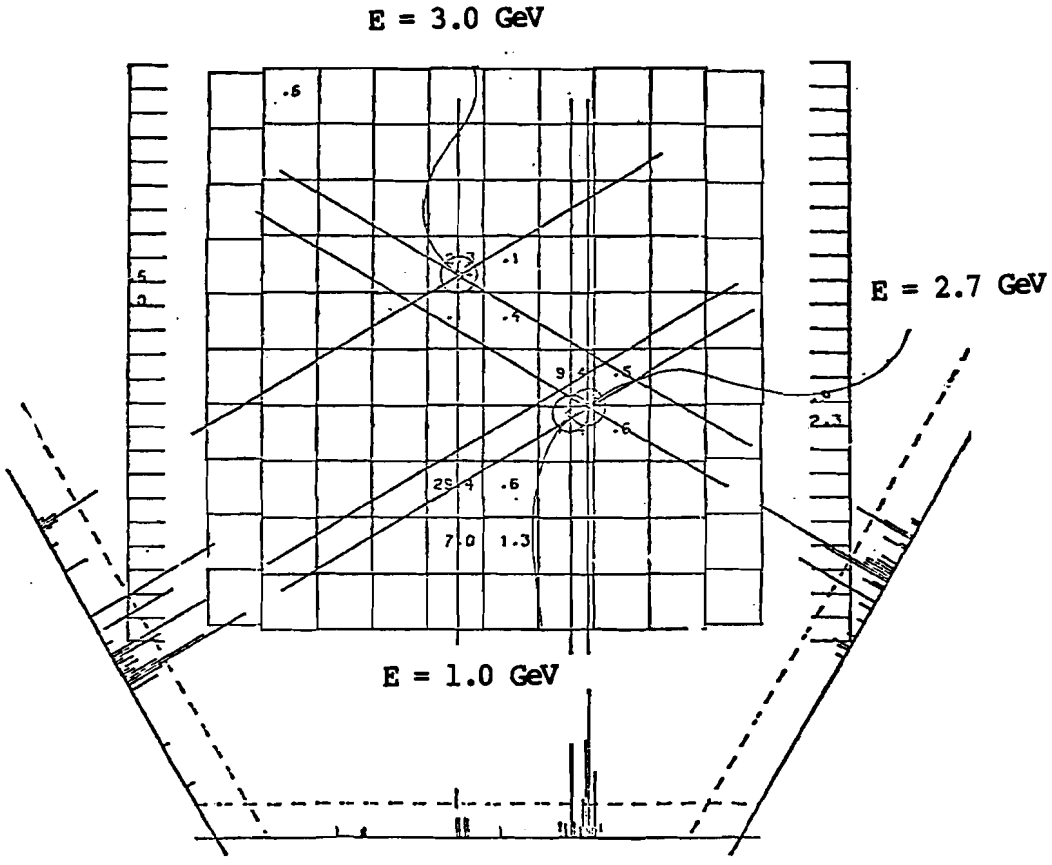

Figure 5-9

Shower of previous figure merged into a dimuon event

the lead glass blocks between different showers. Figure 5-8 shows the electron event in the shower detector where a single shower of 17.6 GeV is found; Figure 5-9 shows the electron event merged in a typical dimuon event in the shower detector. Now P-tube clusters have caused misidentification of the shower position and, subsequently, the shower energy.

The efficiency varies with the amount of confusion between showers, but the possibility of such confusion increases as one approaches the beam box from the outer longitudinal blocks because the distribution of photons from the target is greatest along the beam line. Furthermore, the higher the shower multiplicity of an event, the greater the chance of confusion. Thus, each block will have a different shower efficiency averaged over all photons with their centroid in that block for each multiplicity. For every block with sufficient statistics (>50 events) in the electron calibrations, we calculated the shower efficiency using the method outlined above. Figure 5-10 shows the efficiencies for each such block as a function of the block's distance from the center of the beam box. The efficiency is defined as the fraction of events in which the electron shower is found within 0.5 cm of the correct position and 0.5 GeV of the correct energy. At this point, identical cuts have been imposed on the accepted merged events as in the $J/\psi-\gamma$ events in regard to the quality of the showers: 1) at least 6 cm from the beam hole or

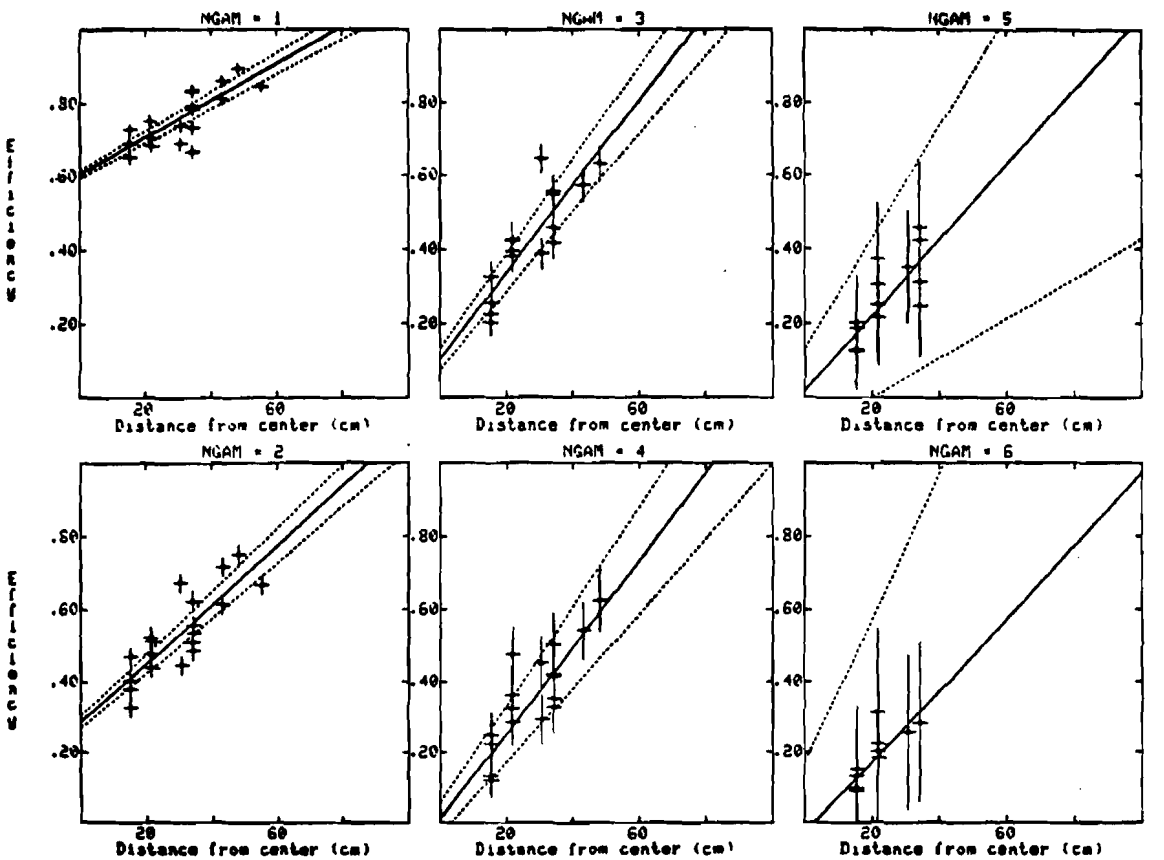

Figure 5-10

Shower efficiencies as a function of distance from the center of the beam box and shower multiplicity with linear fits for extrapolation into non-central blocks

edge of the array, 2) no sharing of shower energy between showers--even to the extent that showers are rejected if two showers share energy into a third non-central block, and 3) 6 or fewer showers which satisfy the previous conditions (otherwise, the event is considered pathological). Since only the central blocks had any significant statistics, the data was extrapolated linearly to any distance from the center of the beam box. These fits are also shown for other blocks in Figure 5-10. The chamber and shower efficiencies are then used in the Monte Carlo calculations discussed in the next section.

5.4 Acceptances of the Detectors

As in most high energy experiments, the acceptance was found by Monte Carlo methods: that is, the experiment was simulated by a computer program and events which the simulation found were detected by the appratus were compared against all events generated in the simulation. The flexibility of this approach allows the acceptance to be calculated as a function of any desired variable. On the con side, the production of the desired reactions requires a model of the mechanisms involved in the reaction; often, these mechanisms are just what you are trying to determine.

Figure 5-11 shows Feynman x distributions for (a) all dimuons which passed the weeding cuts, (b) all events in the J/ψ region (3.05 GeV < M < 3.15 GeV), (c) all events in the background region (2.90 GeV < M < 3.00 GeV and 3.20 GeV < M < 3.30 GeV), and (d) the background subtracted J/ψ sample. This background subtraction was accomplished simply by assuming that the number of background events under the J/ψ signal region was the average of the number of the background events in the two adjacent background regions. One concern was that the Feynman x or transverse momentum distributions might be different for J/ψs associated with χs than for J/ψs not so associated. Thus, Figure 5-12 shows Feynman x distributions for (a) all dimuons which combined with a high-quality photon to form a mass between 3.30 and 3.60 GeV and (b) all J/ψs which passed this criterion. The two distributions appear the same within error bars.

The acceptance of the total detector was calculated as the function of any particular variable (dimuon mass, Feynman x, or transverse momentum) by generating a flat distribution in the variable in question and using experimentally found distributions in the remaining variables. The functional form of these distributions was taken from an earlier experiment in the Muon Laboratory at the same beam momentum (Branson 1977; Anderson 1979). They parameterize the invariant cross section for dimuons created in pion-carbon interactions in the following form:

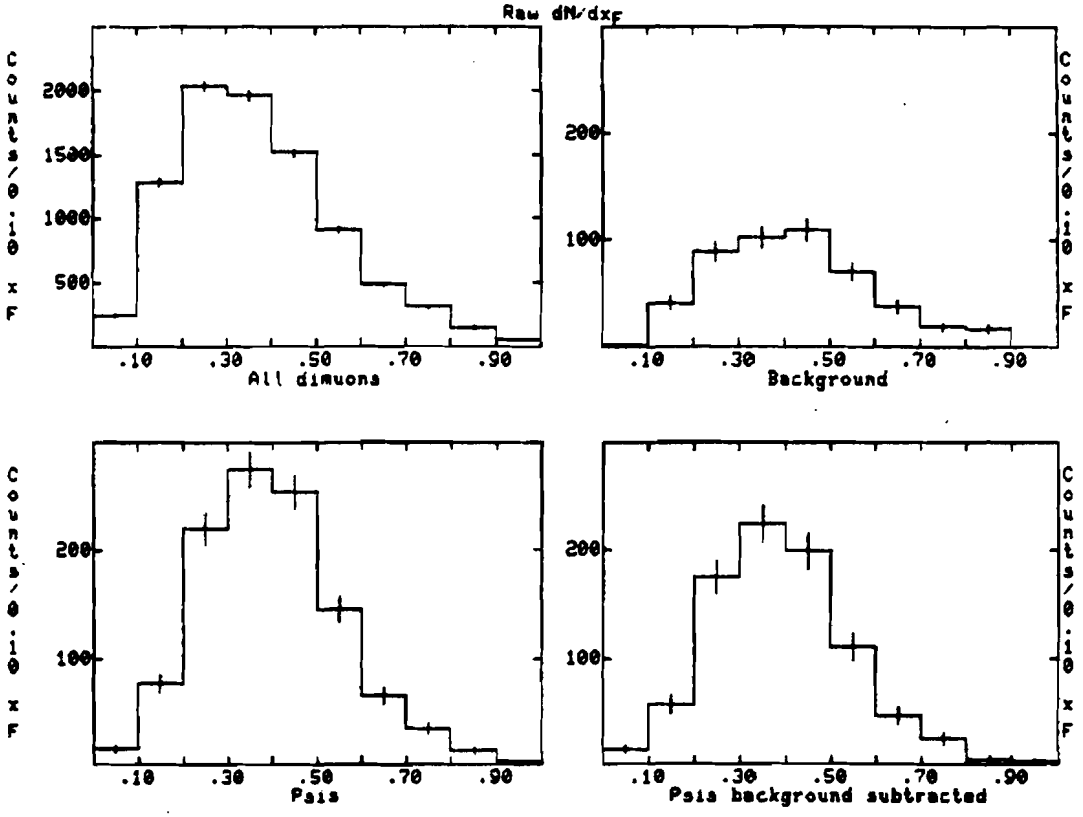

Figure 5-11

Raw Feynman x distributions

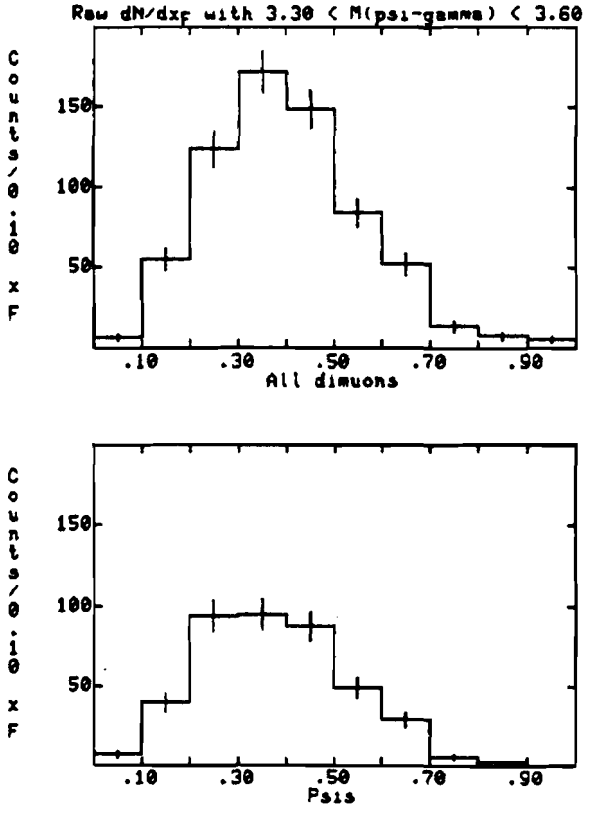

Figure 5-12

Raw Feynman x distributions

$$Ed^3\sigma/dp^3 = C \times \exp(-Bp_T) \times (1-|x_f-x_{fo}|)^A$$

$$B = 1.90\ (GeV/c)^{-1}$$

$$A = 1.65$$

$$x_{fo} = 0.20$$

where the free parameters A and B are tabulated for different mass regions of the dimuon spectrum. The values shown are evaluated at the J/ψ mass. The χs were generated using the above distributions, decayed isotropically in their center of mass frame to $J/\psi-\gamma$, then further into dimuons and the single photon, and then sent through a simulation of the apparatus. This and other experiments have found that using the same x_f and p_T distributions for the χ as the J/ψ produces results which agree well with the data. All geometric acceptances and the efficiencies of the chambers and the shower detector have been taken into account, as discussed in the previous section. The event is assigned a shower multiplicity in the same distribution as actual events with a reconstructable mass in the χ region. The number of detected dimuons divided by the number generated in each bin then gave the acceptance for that variable over the range tested.

Figure 5-13 shows the acceptance as a function of the dimuon mass. Both the J/ψ and the $\psi(3685)$ lie on the plateau of this acceptance curve. Figure 5-14 shows the acceptance correction to the Feynman x distribution, and Figure 5-15 shows the acceptance corrected

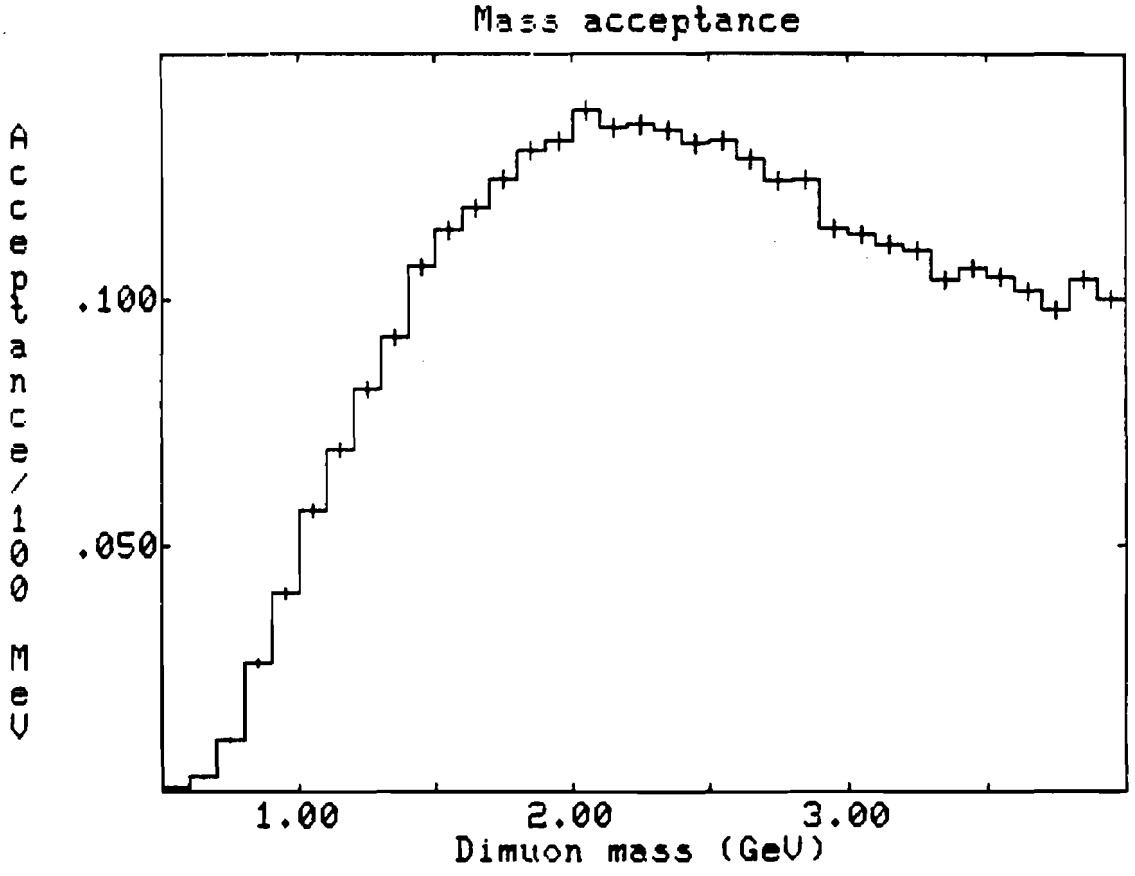

Figure 5-13

Dimuon mass acceptance

Feynman x distribution found by dividing the background subtracted raw Feynman x distribution by the acceptance correction. Figure 5-16 shows the acceptance correction to the transverse momentum distribution, and Figure 5-17 shows the acceptance corrected transverse momentum distribution.

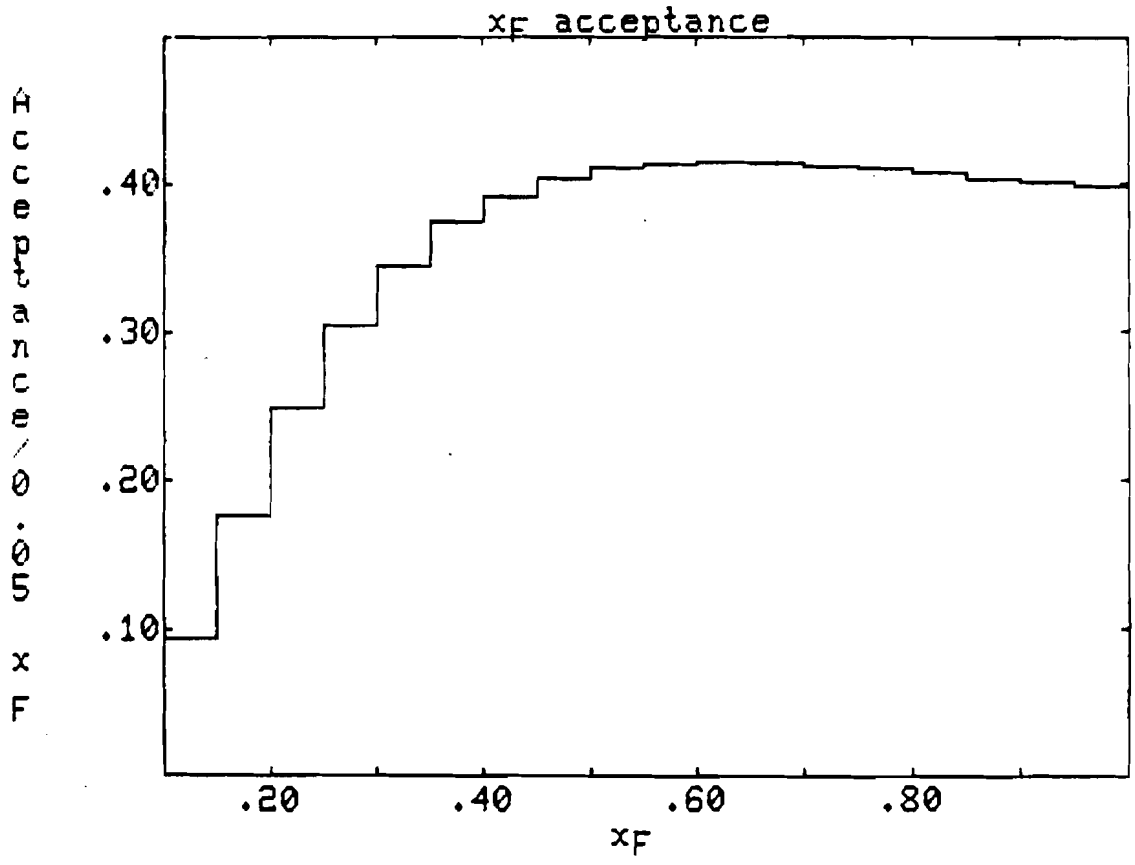

Figure 5-14

Feynman x acceptance for the J/ψ

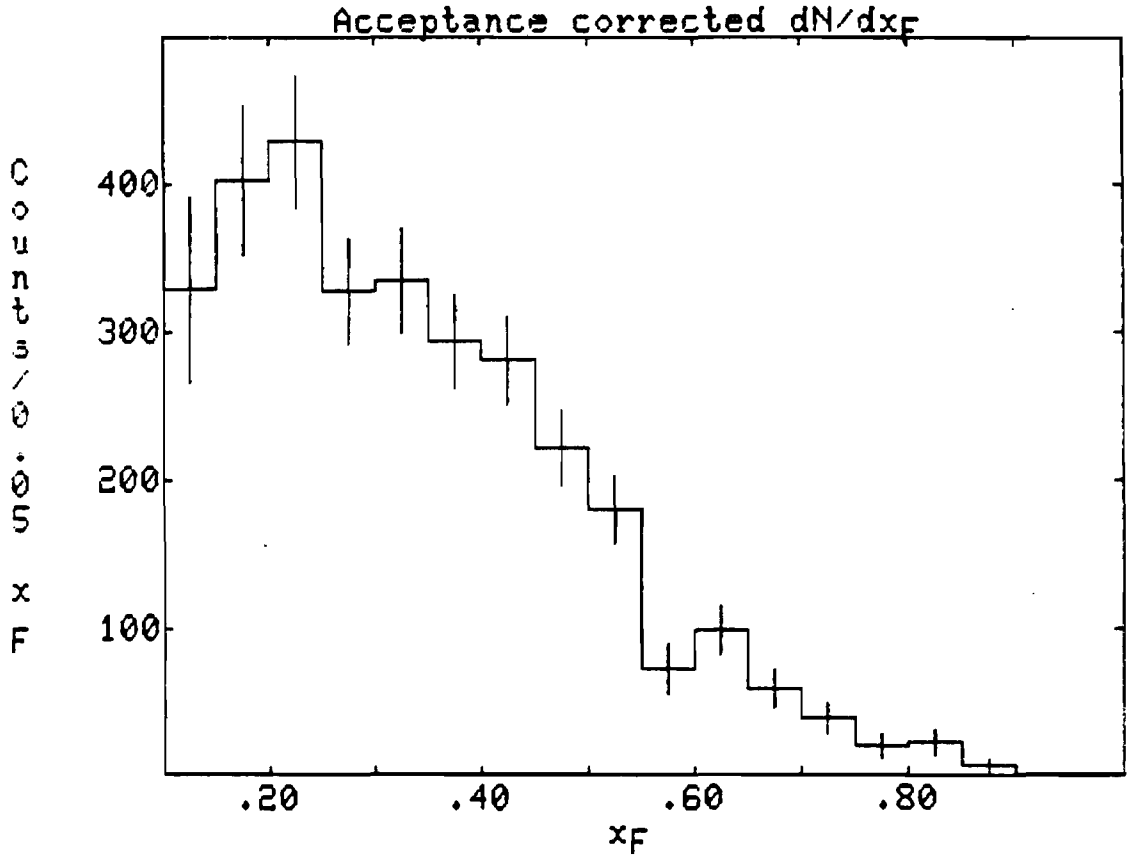

Figure 5-15

Acceptance corrected Feynman x

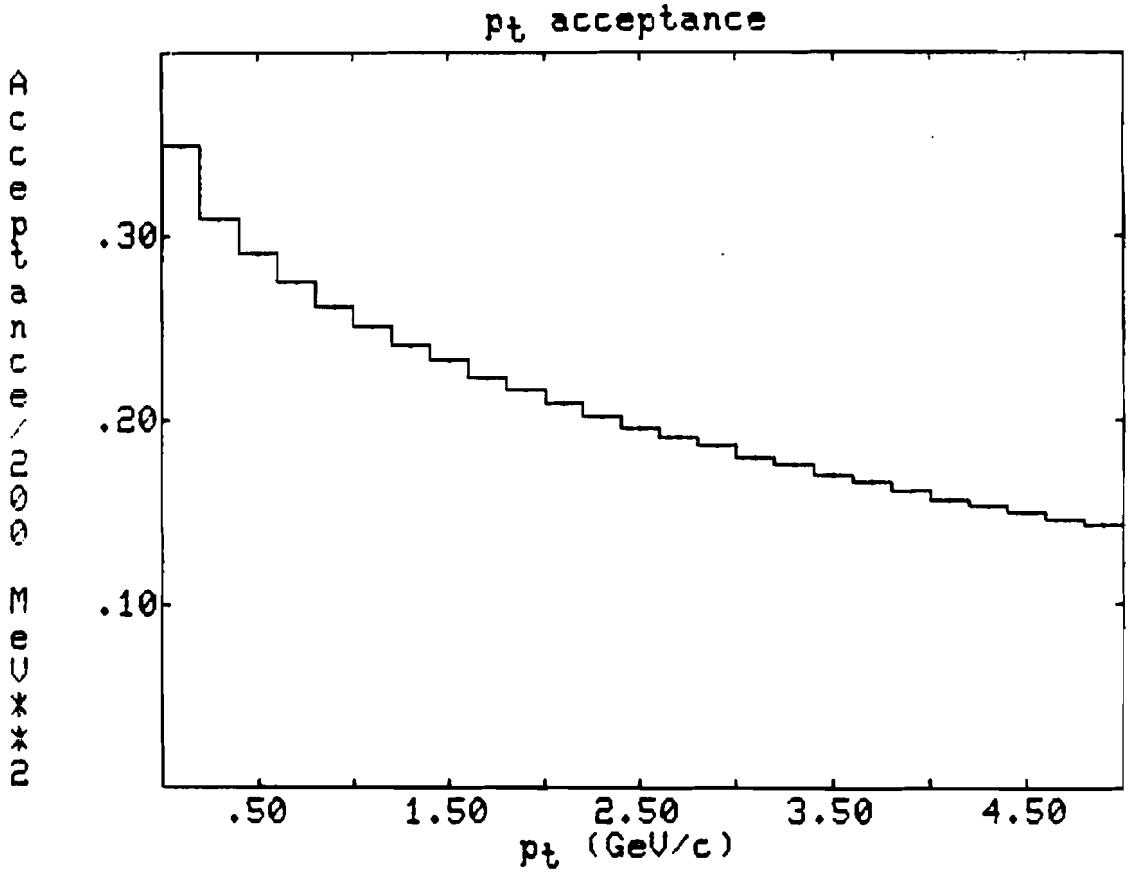

Figure 5-16

Transverse momentum acceptance for the J/ψ

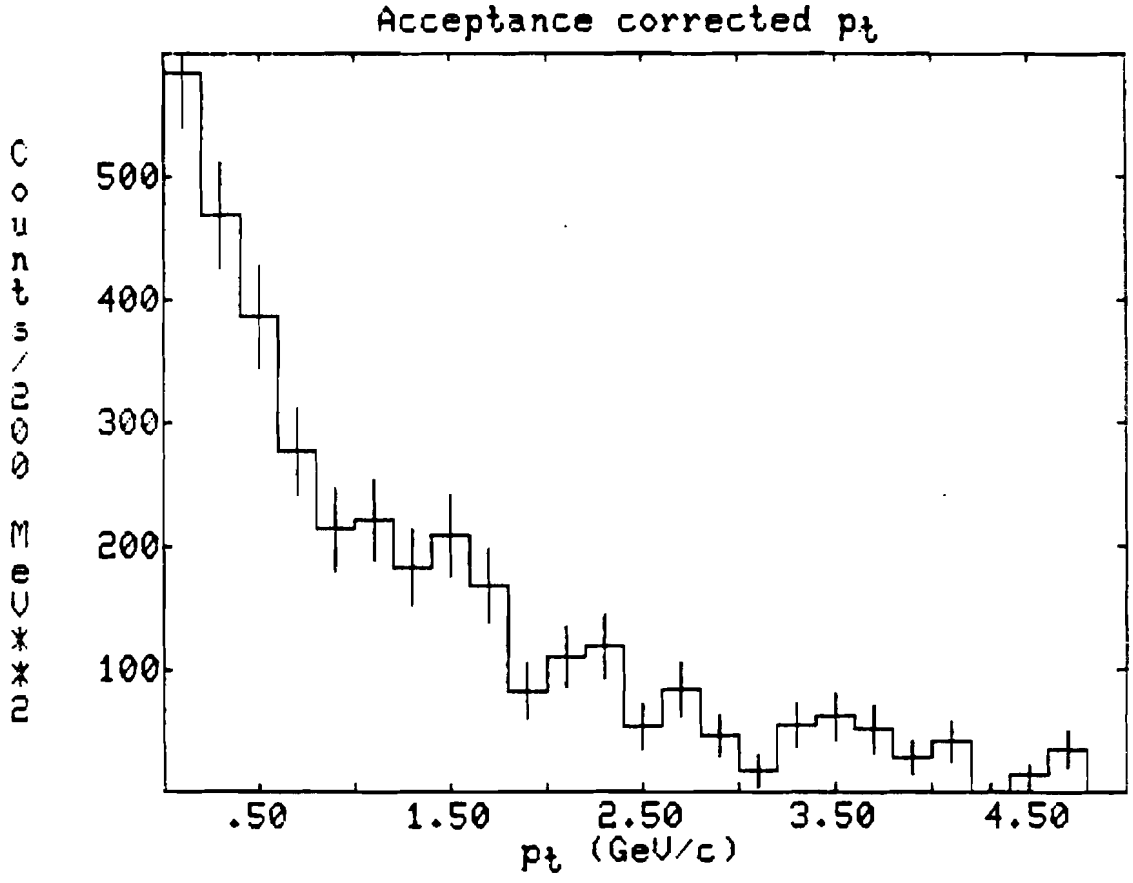

Figure 5-17

Acceptance corrected transverse momentum

CHAPTER SIX

CONCLUSIONS

Two final results will be presented here: first, the fraction of J/ψs produced from ψ(3685)s, the fraction of J/ψs produced from the χ mesons, and the fraction of J/ψs produced directly; second, a determination of the charm suppression factor in meson production.

6.1 J/ψ Production Sources

To determine the sources of J/ψs we must estimate our number of χ mesons and ψ(3685)s. The latter has already been determined in the fit of the dimuon spectrum (Figure 5-4). The solid lined distribution in Figure 6-1 shows the J/ψ-γ invariant mass distribution. An eyeball fit of the background gives an estimate of about 60 χ events in a peak about 90 MeV wide at its base and centered at 3510 MeV. Two independent background curves were developed to find the number of χ mesons produced. The first of these backgrounds was produced by combining the J/ψ from each event with the showers from ten other events. The second background was the result of a Monte Carlo simulation using inclusive photon data from an earlier experiment combined with real J/ψs.

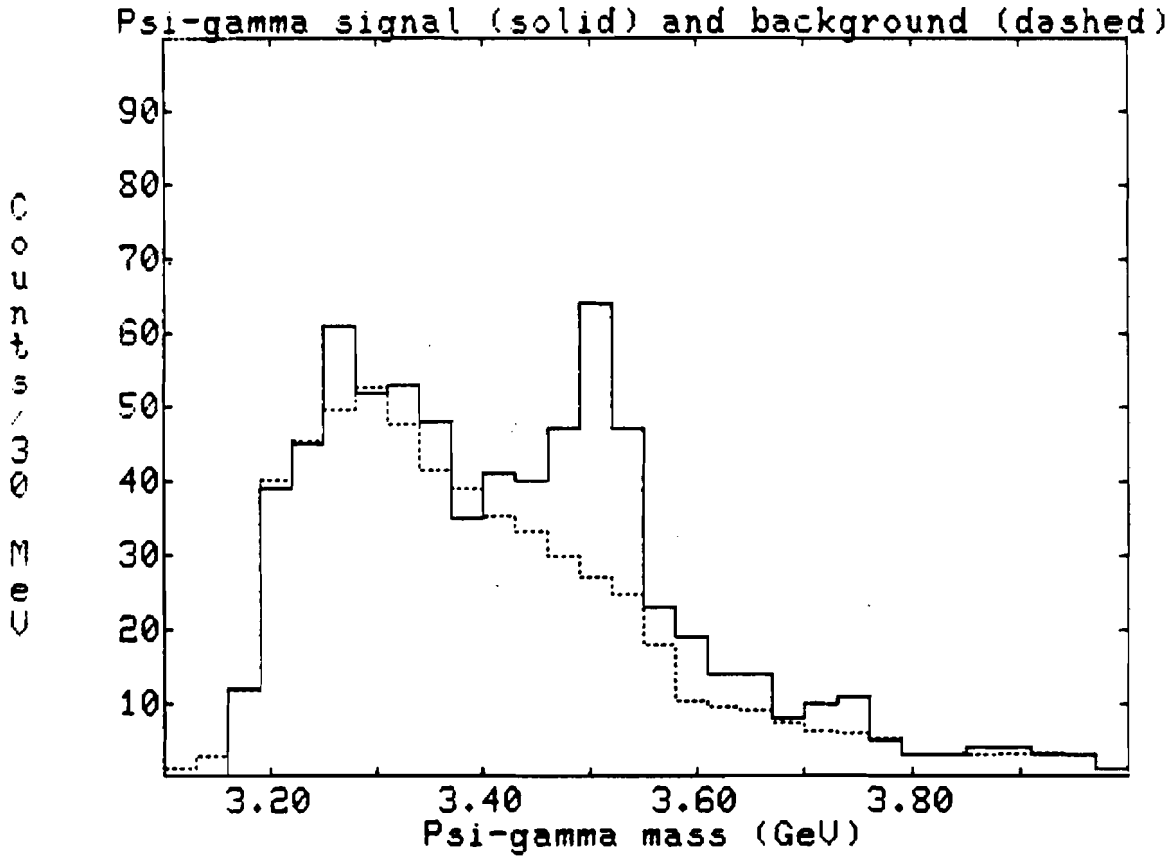

Figure 6-1

$J/\psi-\gamma$ signal and "mixed event" background mass distributions

The first of these two methods involved storing each set of eleven dimuon events. Then each J/ψ is used to create an invariant mass along with the photons from the ten other events. This creates a background with ten times as many events as the $J/\psi-\gamma$ mass plot, in which there are included ten times the true number of photons from χ mesons. Because these photons are generally of higher momentum than the photons in the background, they contribute to a broad "kinematic bump" atop the background in the area of the χ mesons. By using a Monte Carlo simulation of background photons produced by decays of π^{o}s from the target, and combining these photons with real dimuon pairs at the J/ψ mass, we can recreate and subtract this "kinematic bump" from the background curve. The remainder of the background curve just contains ten times the number of events in the background of the $J/\psi-\gamma$ mass spectrum. So, dividing the background by ten and subtracting it from the original mass spectrum should just give the χ meson signal. The number of χ mesons found can be plugged back into the procedure at the point where the "kinematic bump" is being subtracted so that the procedure can be reiterated. Figure 6-1 shows the background curve superimposed on the real curve; Figure 6-2 shows the signal curve less the background. In this case, the procedure had been iterated four times. Adding the three 30 MeV bins about the peak at 3510 MeV, and taking into account the error bars gives 72.1 ± 14.1 events.

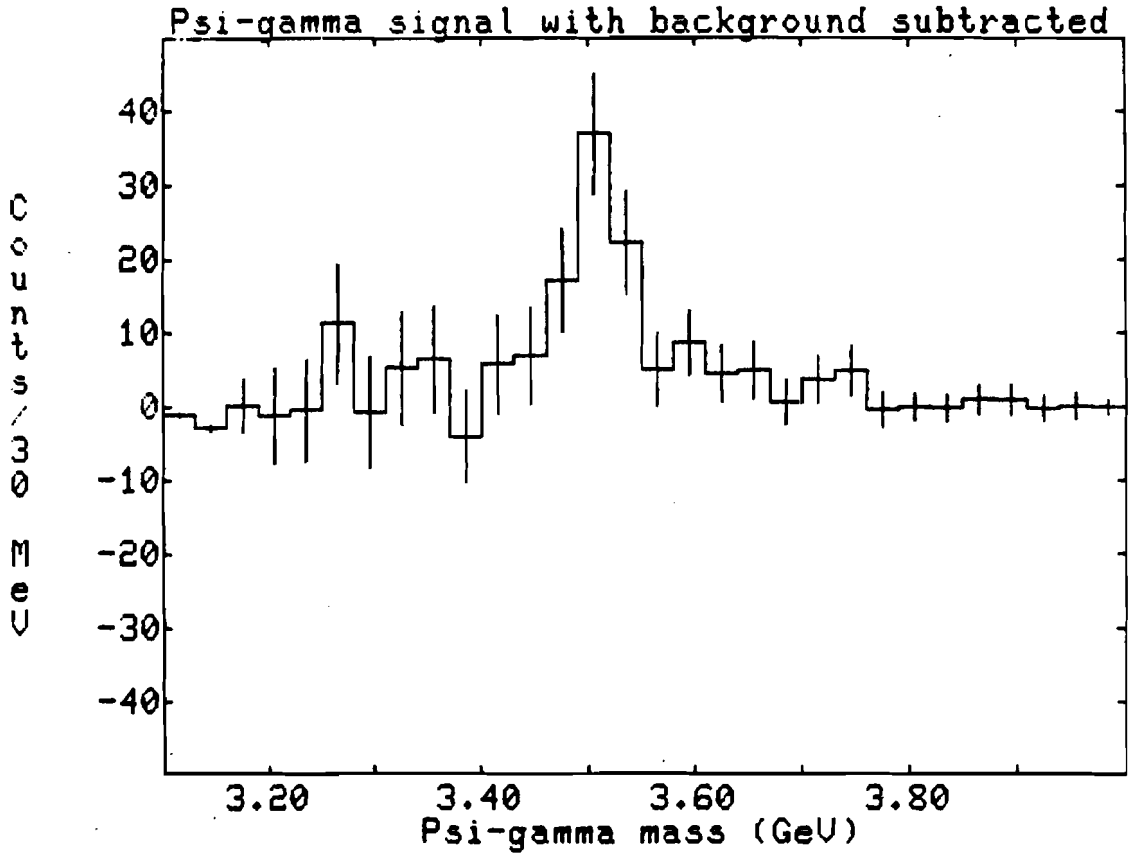

Figure 6-2

$J/\psi - \gamma$ signal with "mixed event"

background subtracted

As a confirmation of this calculation of the number of χs, an independent method of creating a background was employed. This method generated background events from the inclusive photon distribution found with a 200 GeV pion beam in a bubble chamber experiment (Biswas 1980). Figures 6-3 and 6-4 show the Feynman x and transverse momentum distributions for their experiment at this beam energy; superimposed on the data points are fits we used in the Monte Carlo simulation. Thus, totally independent simulated photons and real J/ψs were combined to form a background curve. This curve was then normalized to the number of background events in the actual $J/\psi-\gamma$ plot. This, in turn, gave a new value for the number of χ mesons which redetermines the normalization of the background curve. In this way, this procedure too can be iterated. Figures 6-5 and 6-6 show the result after four iterations: first, the signal with the background superimposed, and then the signal less the normalized background curve. In this case, we obtain for the number of χ mesons in the three 30 MeV bins centered on 3510 MeV, 68.9 ± 13.3. Note that this fit does not work nearly as well as the other, perhaps because photons in association with J/ψs do not have the same kinematic distributions as the inclusive photon spectrum. The two fits are in essential agreement as to the number of χs and the location of the peak.

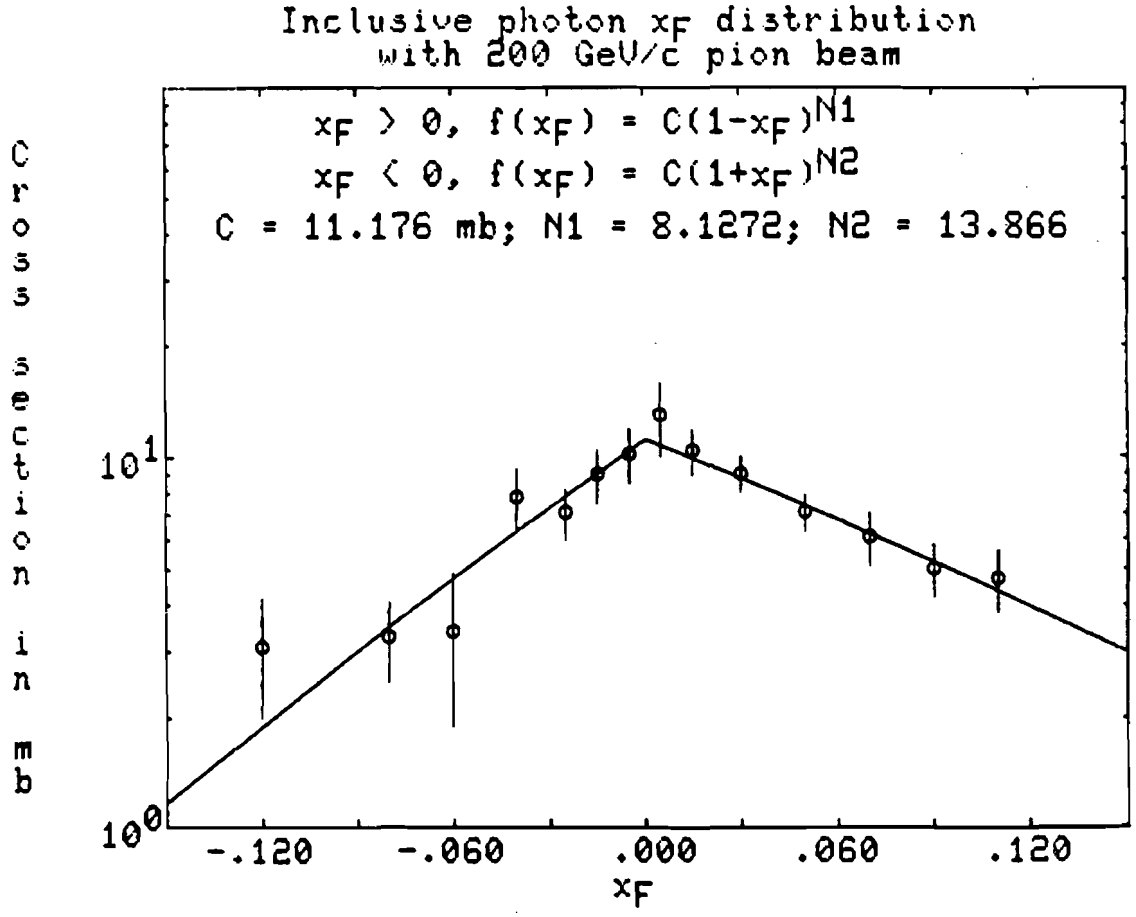

Figure 6-3

Inclusive photon Feynman x distribution

with 200 GeV/c pion beam

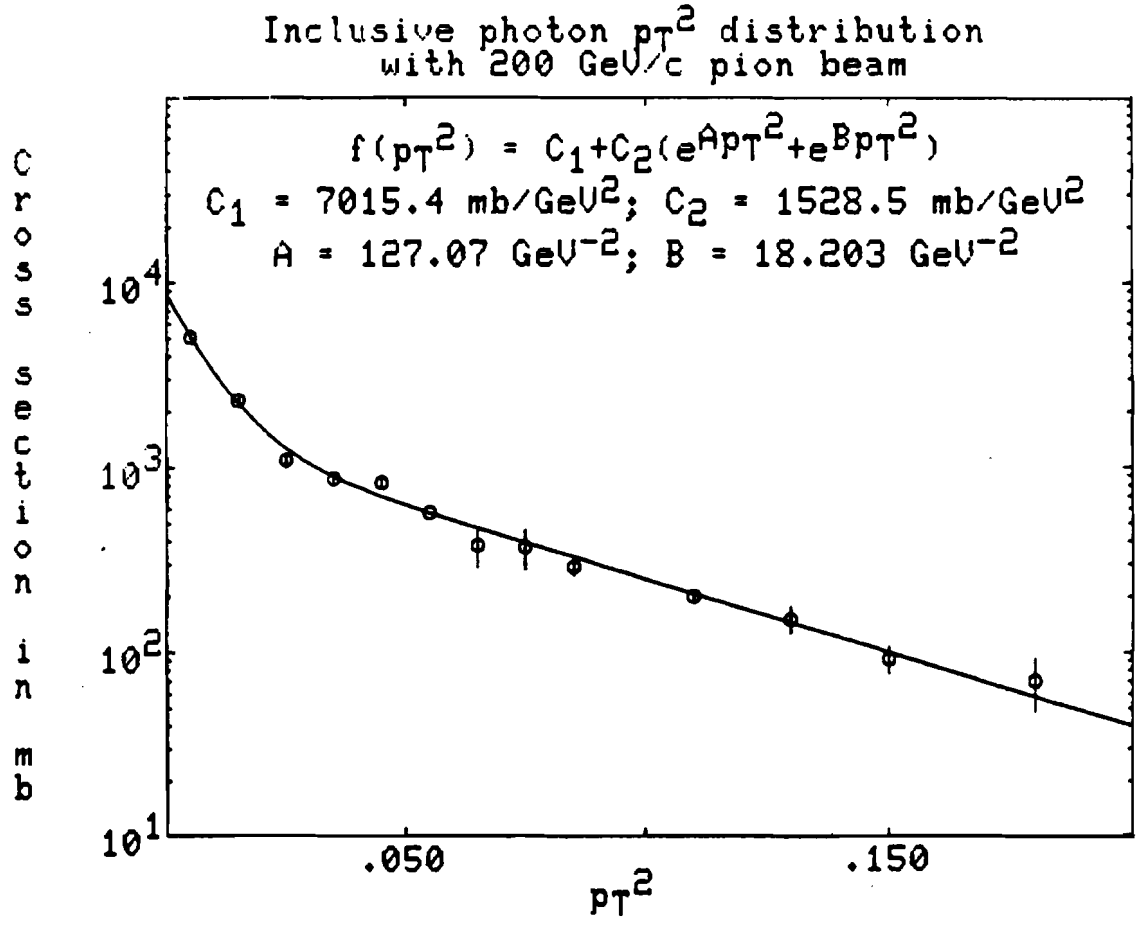

Figure 6-4

Inclusive photon transverse momentum distribution

with 200 GeV/c pion beam

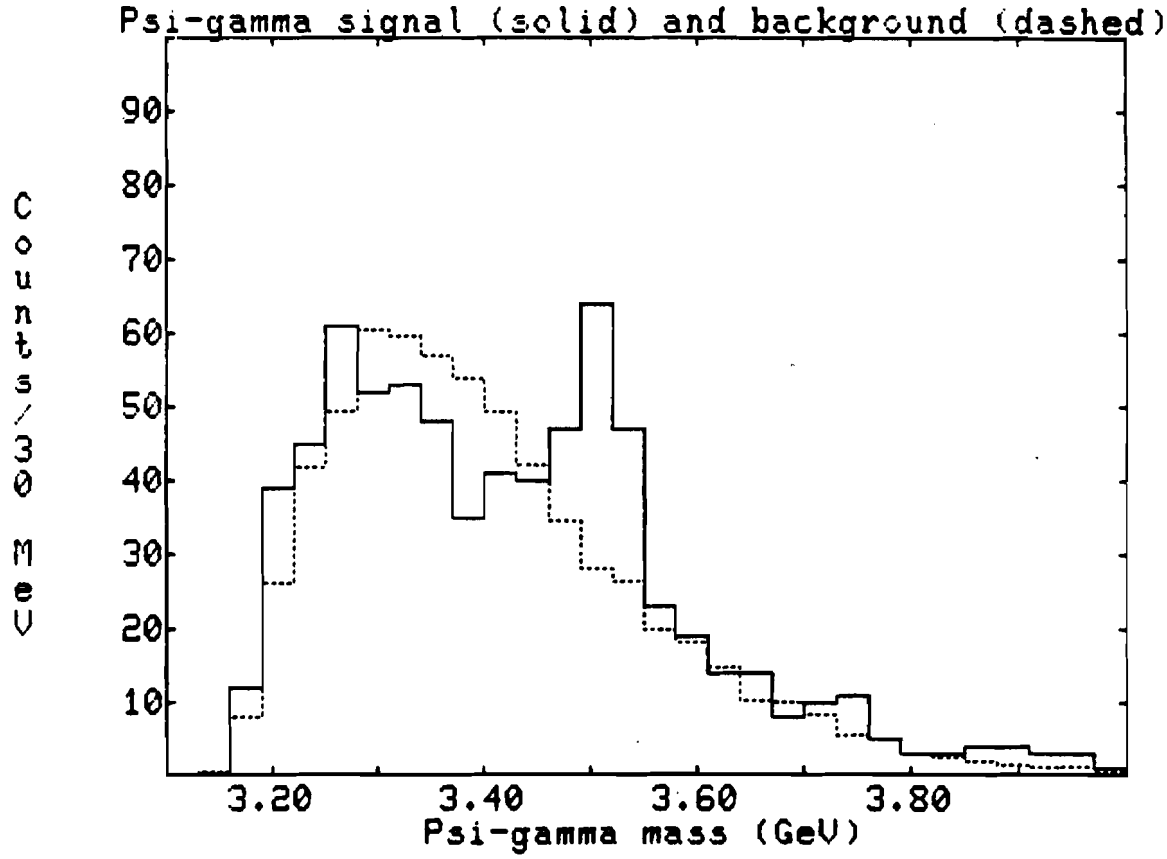

Figure 6-5

$J/\psi-\gamma$ signal and "inclusive photon" background mass distributions

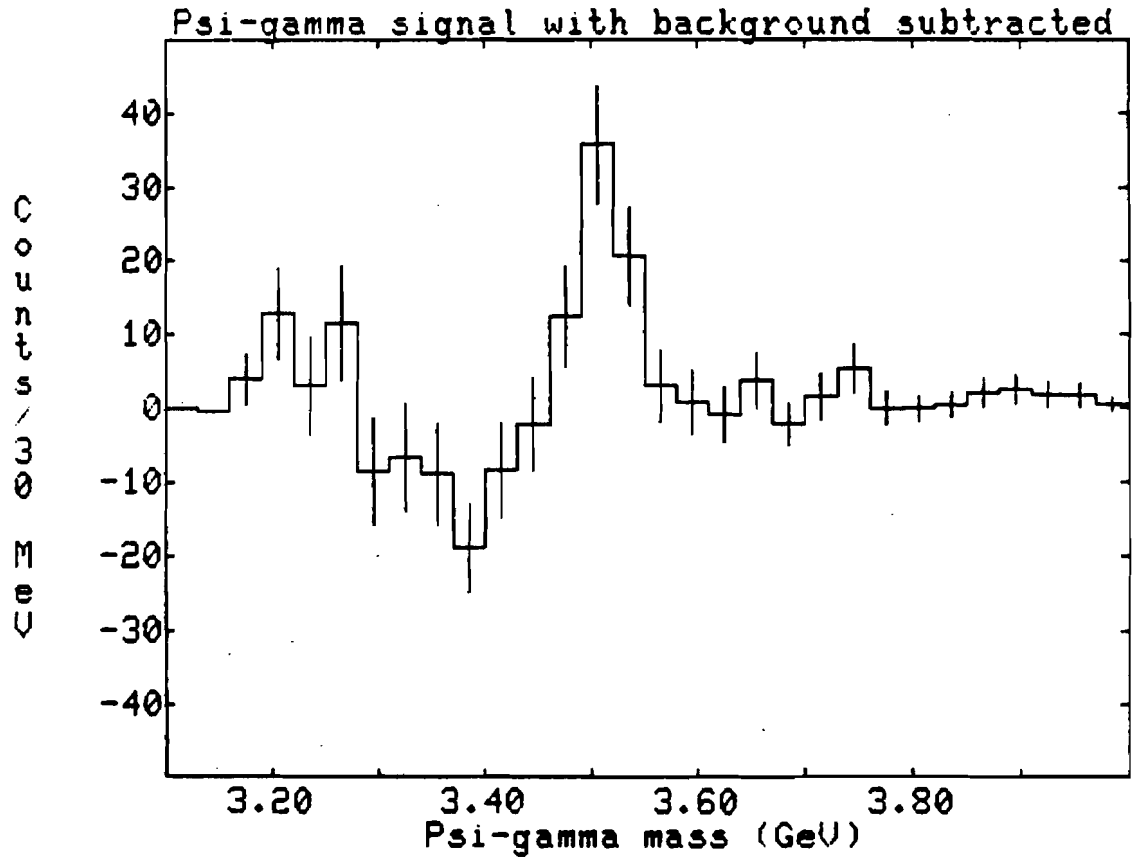

Figure 6-6

$J/\psi-\gamma$ signal with "inclusive photon"

background subtracted

Using the first (and perhaps less biased) fit, we obtain a value for the fraction of J/ψs produced from χs:

$$F_{\psi\chi} = [N(\chi)/\text{Acceptance}(\gamma)]/N(J/\psi)$$
$$= [(72.1 \pm 14.1)/(0.25 \pm 0.04)]/(948.2 \pm 32.2)$$
$$= 0.304 \pm 0.077$$

where the number of J/ψs is only in the bins used to construct J/ψ - γ invariant masses (3.05 GeV < M < 3.15 GeV). The shower acceptance was dependent on the data because, for each event in the three 30 MeV signal bins centered on 3510 MeV, the location of the shower and the shower multiplicity of the event was used to weight the event by its shower efficiency. No attempt was made to alter the efficiency for the background events in these bins. The geometric acceptance for showers is known from Monte Carlo simulations of χ decays (in this case using only the 1^{++} state with a width which reproduces our result). Thus, the factor above for shower acceptance is actually derived from the acceptances summed over all the events. The simple geometric acceptance of the shower detector for photons associated with χ decay is 0.51 $\pm$ 0.06 where the error arises from allowing a 1.0 cm error in the position of the detector. This error is folded in with the original error for shower acceptance (0.25 $\pm$ 0.03) to give the error shown above. The error of 0.03 was calculated by changing all the shower efficiency fits by one standard deviation in their slopes and intercepts (i.e., using the dashed lines

in Figure 5-10 instead of the data points for central blocks and the solid line fits for non-central blocks). Dividing the shower acceptance by the geometric acceptance, we obtain the average efficiency of the shower detector for photons from χ decays, 0.49 ± 0.06.

For the fraction of J/ψs produced from the hadronic decays of the $\psi(3685)$, we take the ratio:

$$F_{\psi\psi'} = (\text{total } N(\psi(3685))/(\text{total } N(J/\psi)) \times B(\psi(3685) \to J/\psi + X)$$

$$\text{total } N(\psi(3685)) = N(\psi(3685))/[B(\psi(3685) \to \mu^+\mu^-) \times \text{Acceptance}]$$

$$= (29.8 \pm 7.1)/[(0.008 \pm 0.002)(0.105 \pm 0.006)]$$

$$\text{total } N(J/\psi) = N(J/\psi)/[B(J/\psi \to \mu^+\mu^-) \times \text{Acceptance}]$$

$$= (1264 \pm 44)/[(0.074 \pm 0.012)(0.104 \pm 0.006)]$$

$$BR(\psi(3685) \to J/\psi + \pi^+\pi^-, \pi^0\pi^0, \eta, \pi^0) = (0.33 \pm 0.02) +$$

$$(0.17 \pm 0.02) + (0.028 \pm 0.006) + (0.001 \pm 0.0003)$$

$$= 0.53 \pm 0.03$$

$$F_{\chi\psi'} = 0.114 \pm 0.045$$

Thus, assuming these to be the only states decaying to the J/ψ, the total fraction of J/ψs produced directly must be:

$$F(\text{direct}) = 1 - F_{\psi\chi} - F_{\psi\psi'}$$

$$= 0.58 \pm 0.09$$

The predecessor to our experiment in the Muon Laboratory was Experiment 369 (Kirk 1979). With about 200 J/ψs, they saw $F_{\psi\chi} = 0.70 \pm 0.28$ using a negative pion beam at 217 GeV/c on a liquid hydrogen target and a beryllium target. A preliminary analysis of our data (Hossain 1981) gave $F_{\psi\chi} = 0.38 \pm 0.09$. CERN experiment WA11 (Lemoigne 1982) has a sample of 43,000 J/ψs produced with a 185 GeV/c negative pion beam on beryllium. With this many J/ψs they could use photon conversions into electron-positron pairs which could be measured in the track finding apparatus. Figure 6-7 shows their $J/\psi - \gamma$ invariant mass spectrum in the region of the χ states. They clearly see the 1^{++} and 2^{++} states with populations of 113 ± 25 and 71 ± 22, respectively. They see no indication of the 0^{++} state. They find:

$$F_{\psi\chi} = F_{\psi\chi_1} + F_{\psi\chi_2} = 0.177 + 0.128 = 0.305 \pm 0.114$$

which agrees very well with our result.

In conclusion, the substantial fraction of J/ψs produced directly indicates that some process or processes other than simple quark fusion and/or gluon fusion must be involved in hadroproduction of charm. The relative production of the charmonium P-states observed by WA11 is in agreement with the color evaporation theory, which would also allow direct hadroproduction of the J/ψ. Our resolution does not allow us to make any statement as to the ratios of the χs; certainly, we are not in disagreement with WA11.

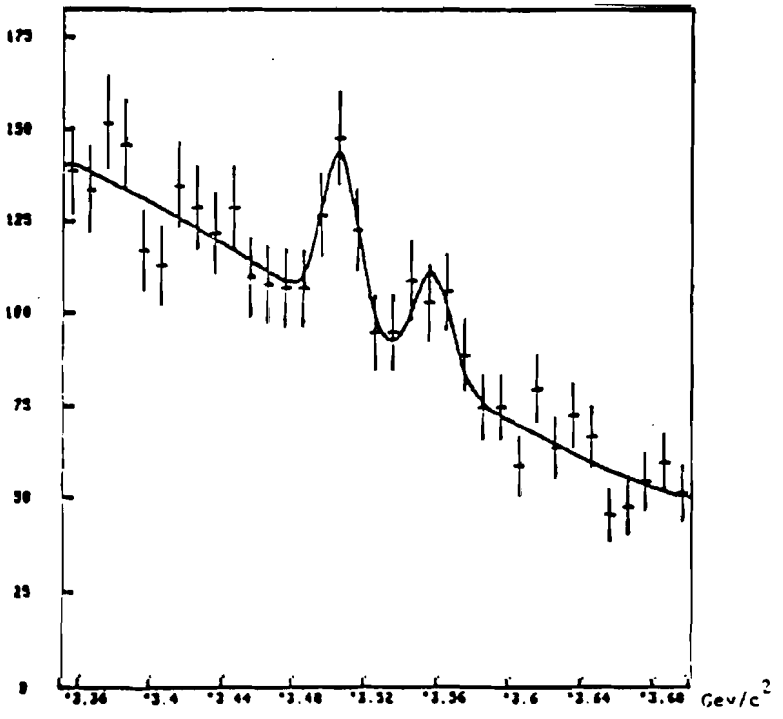

Figure 6-7

WAll J/ψ-γ mass distribution

6.2 The Charm Suppression Factor

Our second result is a determination of the charm suppression factor. Figures 6-8 and 6-9 show background subtracted distributions of the dimuon mass in the regions of the ω and the ϕ. The calculation of these signals and their corresponding backgrounds and acceptances are given in the thesis of P. Schoessow (Schoessow 1983). We can derive the charm suppression factor λ_c in two ratios N_ψ/N_ϕ and N_ψ/N_ω in a restrictive central region of $0.10 < x_F < 0.25$, where the upper limit is chosen to keep the particles centrally produced and the lower limit is set by the acceptance. Correcting for acceptance and branching ratios gives:

$$N_\psi = N_\psi^{\Gamma 2w} F(\text{direct})/[(B(J/\psi \to \mu^+\mu^-)\epsilon_{\mu^+\mu^-}]$$
$$= (162.8+15.2)(0.50+0.10)/[(0.074+0.012)(0.050+0.002)]$$
$$= (2.20\pm0.61) \times 10^4$$

$$N_\omega = N_\omega^{\Gamma 2w}/[(B(\omega \to \mu^+\mu^-)\epsilon_{\mu^+\mu^-}]$$
$$= (1940\pm200)/[((7.2+0.7)\times10^{-5})(0.061+0.008)]$$
$$= (4.42\pm0.85) \times 10^8$$

$$N_\phi = N_\phi^{\Gamma 2w}/[B(\phi \to \mu^+\mu^-)\epsilon_{\mu^+\mu^-}]$$
$$= (820+170)/[((2.5+0.3)\times10^{-4})(0.109+0.011)]$$
$$= (3.01\pm0.78) \times 10^7$$

Using the average value of the strangeness suppression factor $\langle\lambda\rangle = 0.29 \pm 0.02$ and the higher multiplet feed-down factor $\langle\alpha\rangle = 0.13 \pm 0.03$, we can find the charm suppression factor from the

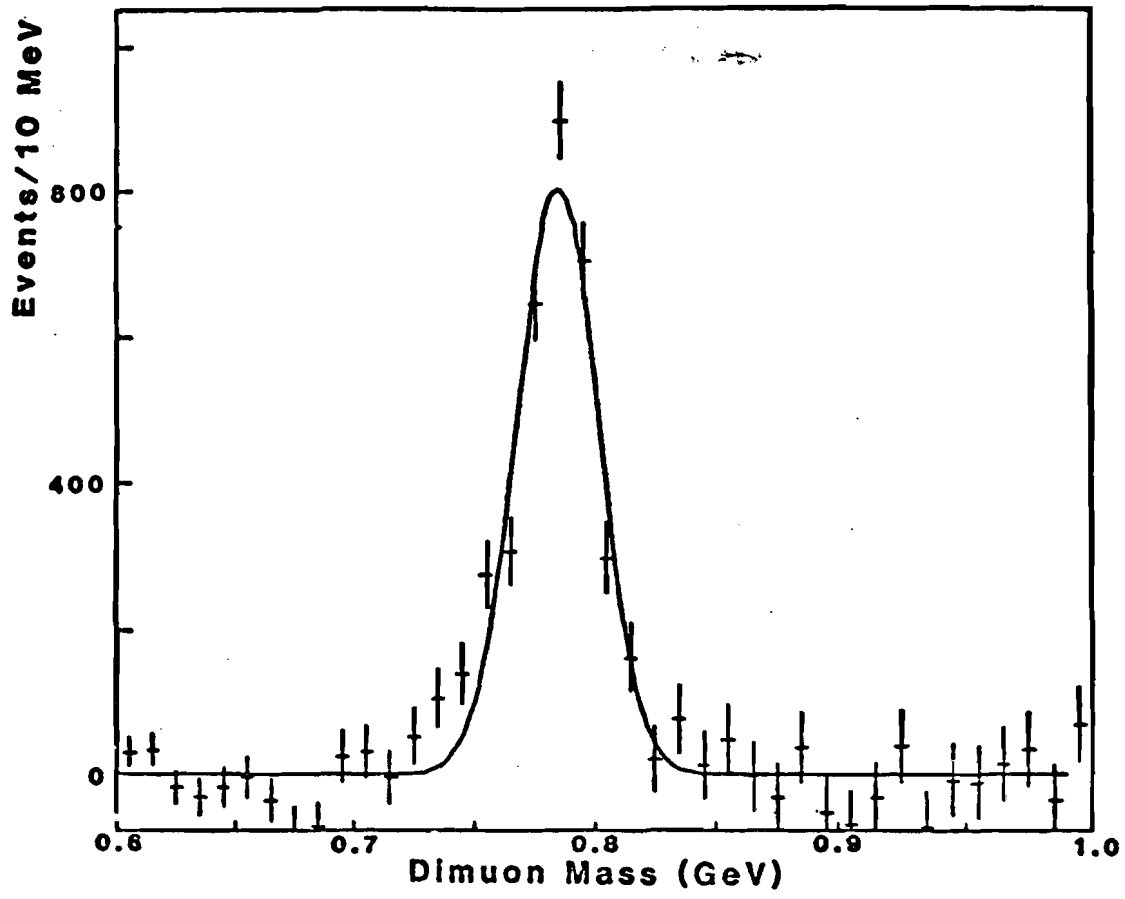

Omega=>Mu+Mu-
M(Omega)=784+/-1 MeV/c**2
FWHM=40+/-2 MeV/c**2
3400+/-240 Events
Background Subtracted

Figure 6-8

Dimuon mass distribution with

background subtracted

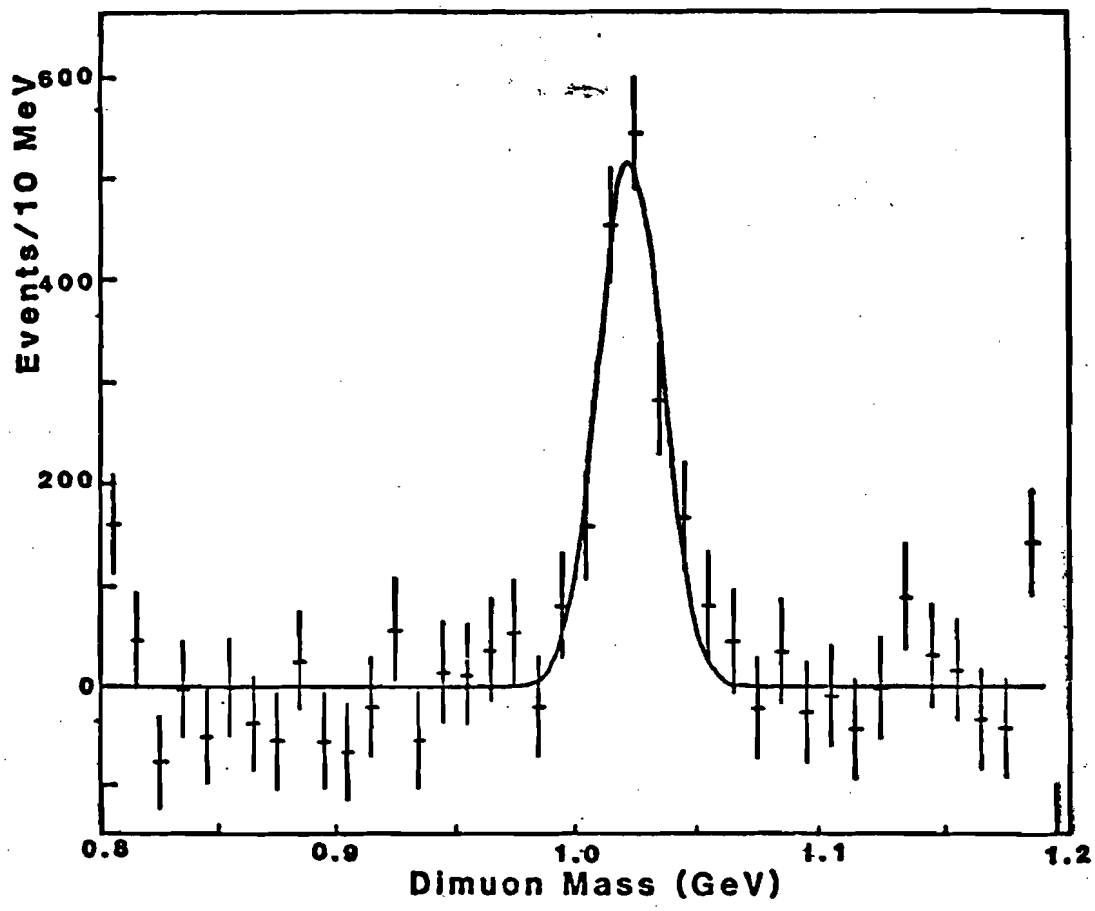

Phi=>Mu+Mu-
M(Phi)=1023+/-1 MeV/c**2
FWHM=30+/-3 MeV/c**2
1700+/-230 Events
Background Subtracted

Figure 6-9

Dimuon mass distribution with

background subtracted

following predictions of the theory:

$$\frac{N_\psi}{N_\phi} = \frac{3\lambda_c^2}{3\lambda^2} \qquad \frac{N_\psi}{N_\omega} = \frac{3\lambda_c^2}{3 + (10.6 + 2.2\lambda)\alpha}$$

These ratios give $\lambda_c = (7.8 \pm 1.6) \times 10^{-3}$ and $\lambda_c = (8.6 \pm 1.5) \times 10^{-3}$, respectively. Using a broader central region of $0.10 < x_f < 0.50$, we obtain $\lambda_c = (6.8 \pm 1.2) \times 10^{-3}$ from the ratio N_ψ/N_ϕ and $(6.8 \pm 1.1) \times 10^{-3}$ from the ratio N_ψ/N_ω. In either case, the two ratios agree very well.

The value of $\lambda_c \cong 8 \times 10^{-3}$ is a factor of at least 100 larger than theoretical models (see section 2.4) would predict. This indicates that the simple additive quark model no longer holds for the heavy quarks. Perhaps the suprising feature of this extremely simple model is that it even works for the strange particles. However, it is interesting to note that the same value is found in two different ratios.

Appendix A

The Lead Glass Shower Detector Construction

Photons were detected with the aid of a large lead glass Cerenkov counter array built by the University of Illinois and Tufts University. This detector was composed of three parts--from upstream to downstream--a passive/active converter section composed of steel sheet, lead sheet, and lead glass blocks with their long axis transverse to the beam direction; a shower detector consisting of three planes of "P-tubes"--long proportional tubes parallel to each other to form an array; and large lead glass blocks with their long axis parallel to the beam axis (Figure 3-14).

The first section, the passive/active converter, was constructed by Tufts University. The major component was 48 "Tufts" lead glass blocks arranged in two side-by-side stacks of 24 blocks each, transverse to the beam axis so that the short dimension was traversed by the electromagnetic shower (Figure 3-16). Each block was 6.35 cm X 6.35 cm X 58.4 cm (Figure A-1). The lead glass was obtained from Schott and was of the SF-2 type with the parameters shown in Table A-1. Each block is coupled to an Amperex XP-2020 photomultiplier tube by a lead glass "cookie" of dimensions 3.2 cm X 3.2 cm X 10.2 cm to facilitate the use of a magnetic shield for the photomultiplier tube.

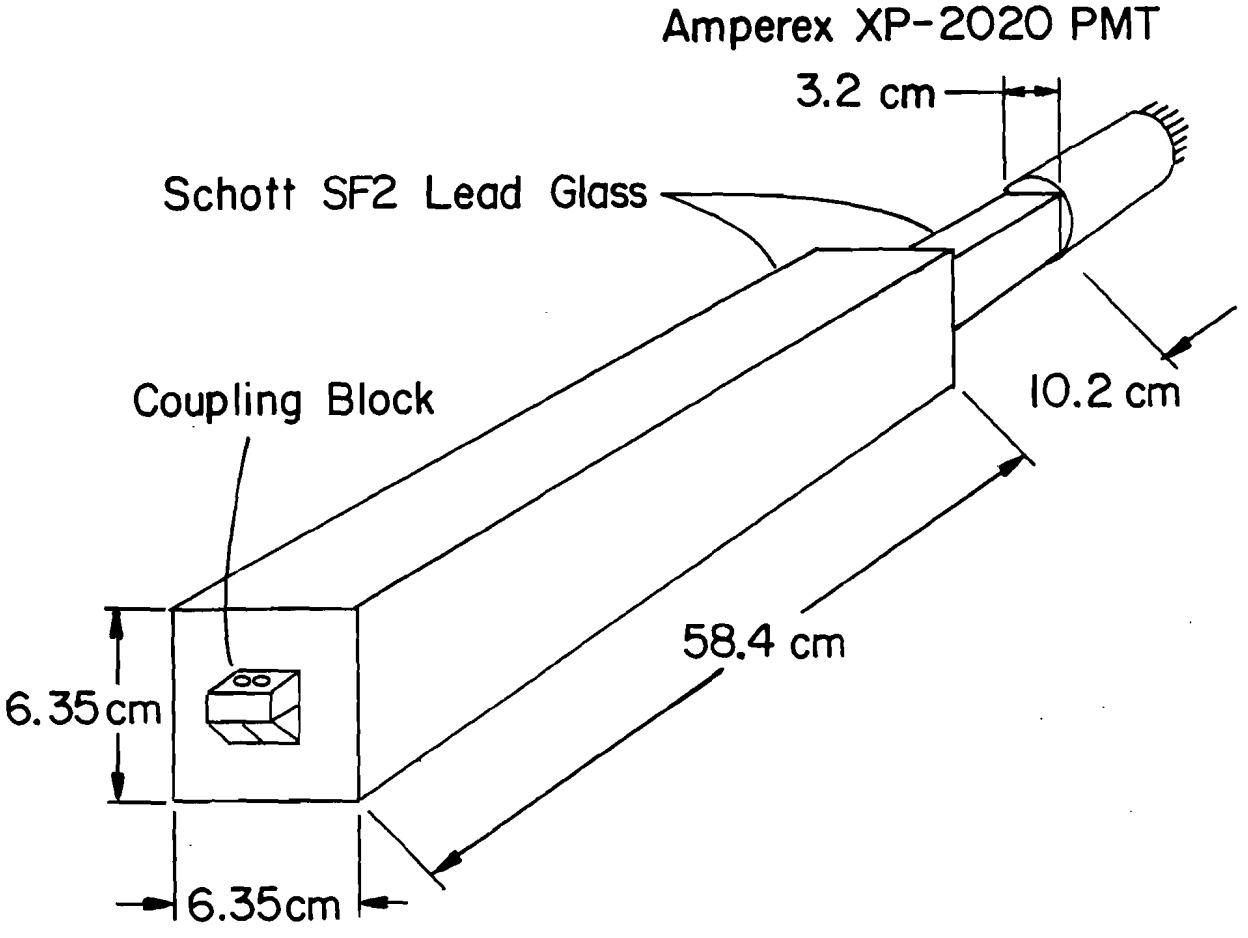

Figure A-1

Transverse lead glass block assembly

Manufacturer: Schott

Glass Type: SF2

Composition: SiO_2 41%

PbO 50%

K_2O 5%

Na_2O 3%

Radiation Length: 2.84 cm

Refractive Index: 1.64769

Specific Gravity: 3.85

Coefficient of Thermal Expansion:

88×10^{-7} (-30° to $+70^{\circ}$ C.)

Internal Transmittance/25 mm

Wavelength (nm)	Transmittance
340	0.15
350	0.47
360	0.708
370	0.837
380	0.894
390	0.940
400	0.968
420	0.981
440	0.985
460	0.988
480	0.992
500	0.994
550	0.995
600	0.995
650	0.995
700	0.995

Table A-1

Transverse lead glass blocks' characteristics

The end opposite had at one time had glued on it a Bakelite plate to hold an LED for calibration; however, this had to be removed because there was not enough space between the two transverse stacks for the LED's to be installed in this fashion. Instead, a "coupling block" was glued to the center of the now bare lead glass at this end on each block.

These blocks had been used in a previous experiment (E369—Bender, 1980) in a longitudinal mode such that they effectively acted as a beam dump. Thus, some of the blocks were yellowed by radiation damage during the course of that experiment. This yellowing was removed by exposing the blocks to direct sunlight over the course of several weeks. Most of the blocks were rewrapped with first a layer of aluminum foil and then a layer of black electrical tape; the first to provide electrostatic shielding and the second to insure light-tightness. This procedure was the same as that used for the longitudinal blocks and will be described in more detail later.

The photomultiplier tubes were shielded from magnetic effects with a Co-netic shield (Perfection Mica Company 1976) which slipped over the cylindrical base and tube and past the tube over the lead glass "cookie". Thus the photocathode front end of the photomultiplier tube had magnetic shielding for 10.2 cm in front of it. The base which contained the electronics neccesary to the

functioning of the photomultiplier is shown schematically in Figure A-2.

Upstream of the transverse blocks was a 1/4" sheet of steel and a 1/8" sheet of lead. This extra amount of passive converter was found, by Monte Carlo calculations, to optimize the total resolution of the photon detector by allowing the shower to start development earlier in the array. This in turn meant that some energy was not detected in the passive converter, but the shower was more developed than it would have been without the passive converter by the time the shower got to the proportional tubes; the gain in position resolution outweighed the loss in energy resolution. Actually, there were two sheets each of steel and lead—one for each stack of lead glass held on by steel straps. Also, the easternmost stack's two central blocks were offset to provide a hole through which the beam could pass, and likewise there were beam holes provided in the corresponding steel and lead sheets.

The entire passive/active converter was held in a steel frame suspended from a dolly which rode in an I-beam so that the converter could be moved aside to provide access to the proportional tubes and the longitudinal lead glass. The steel and lead sheets and the lead glass blocks were held in place by steel straps which encircled an entire stack after passing through slots in the framework. The cables

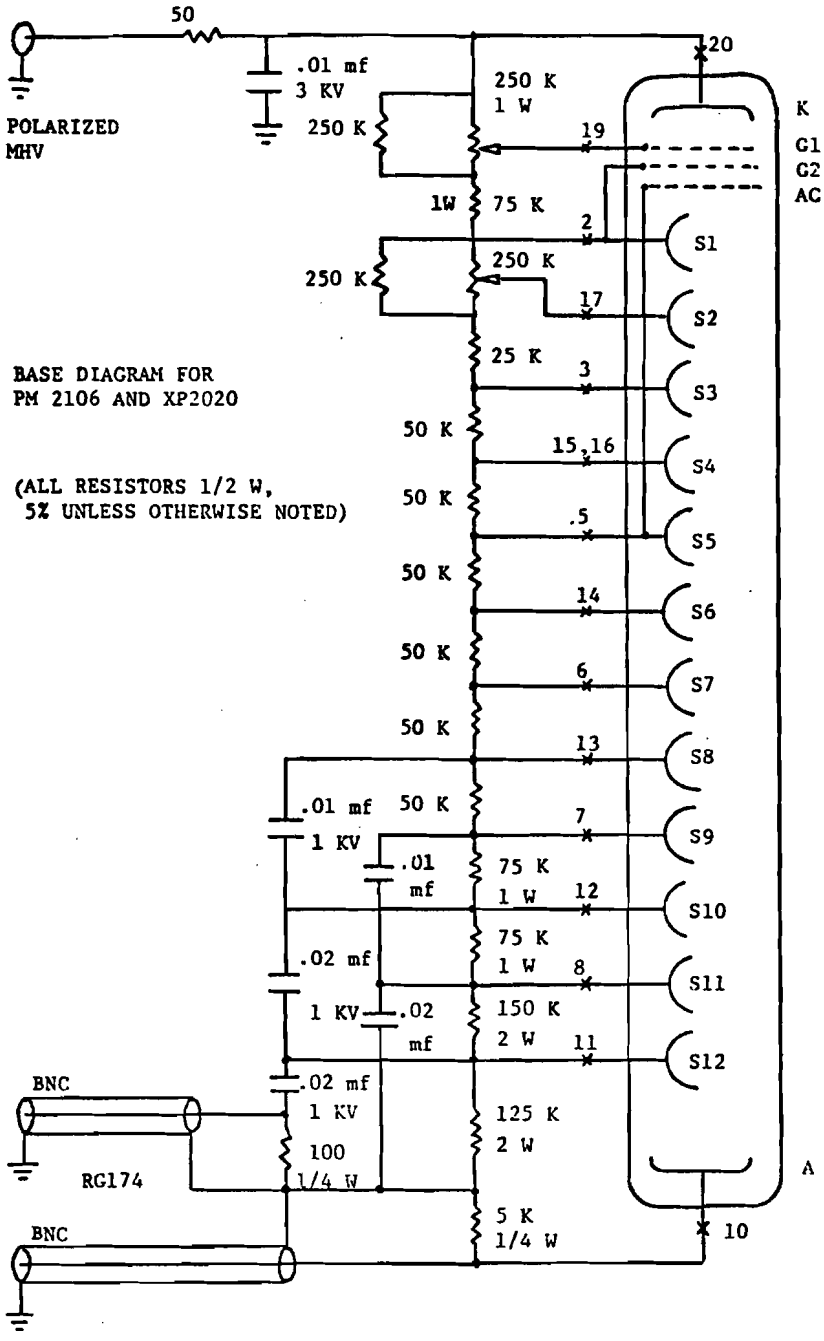

Figure A-2

Transverse lead glass photomultiplier base

(for use with Amperex XP2020 PMT)

for the photomultiplier electronics and the calibration systems were gathered at the top of the frame and then rose to a cable tray above the detector. Riding on top of the Tufts frame were the argon flash lamp system for the transverse lead glass blocks and the cross-calibration photomultiplier (both to be explained later).

Following the passive/active converter were three planes of "P-tubes" built by the University of Illinois. Each plane consists of 194 parallel tubes in a zigzag pattern such that the center wire of each proportional tube is offset 5/16" in the X direction and a little more than 3/8" in the Y directions from its neighbors (Figure A-3). Each tube is 1/2" in outer diameter with a wall thickness of 28 mils. The central wire in each tube is 2 mils in diameter of stainless steel. The tubes are 63" in length with 60" of active wire centered, except for the center 14 tubes of each plane. Here the tubes have been cut in two and a portion removed so no material is present in the beam region; each of the two sections is 29" in length, the central 26" being active. The ends of the P-tubes are embedded in epoxy which also holds the center wire and gas connection for each P-tube. On the upstream side of each plane an aluminum bar attachs the epoxy framework to the large aluminum frame which holds the entire P-tube array (Figure A-4). In turn, this frame was attached to the steel box which contained the longitudinal lead glass blocks by Unistrut constructions. The three planes from upstream to downstream were

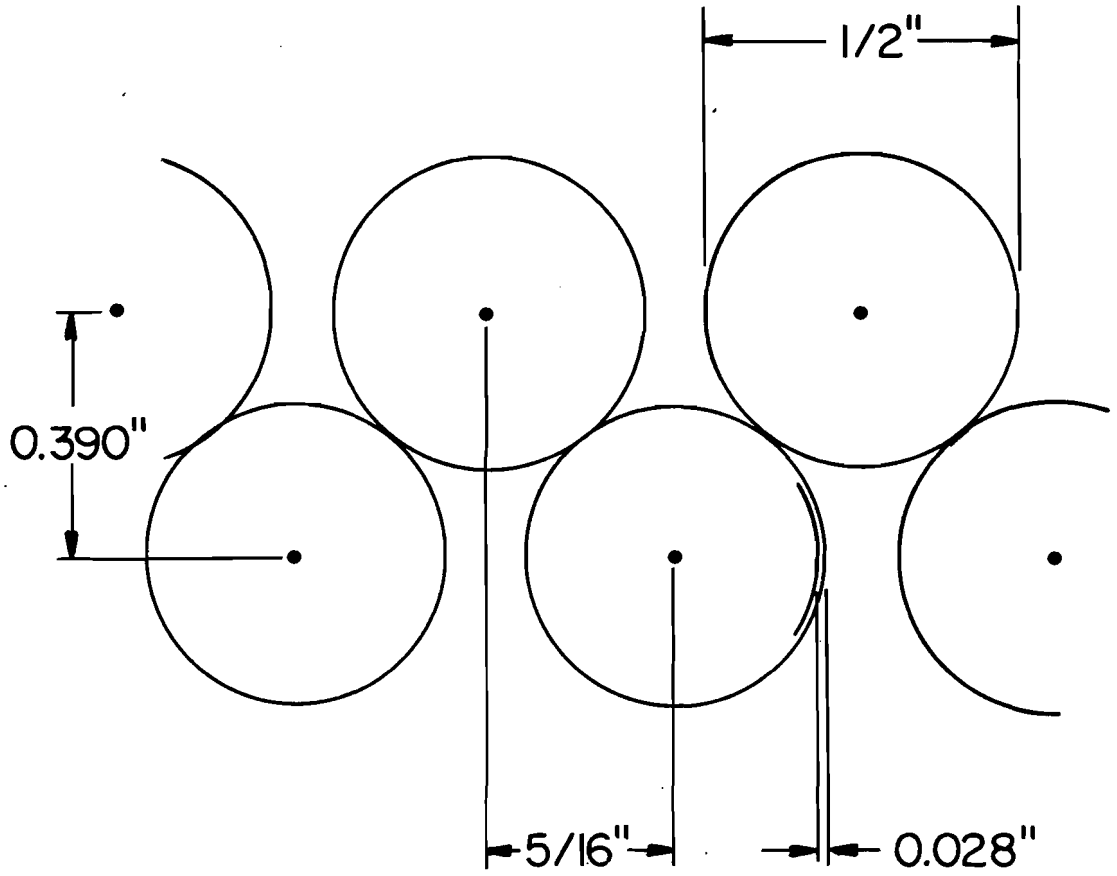

Figure A-3

Details of a P-tube plane

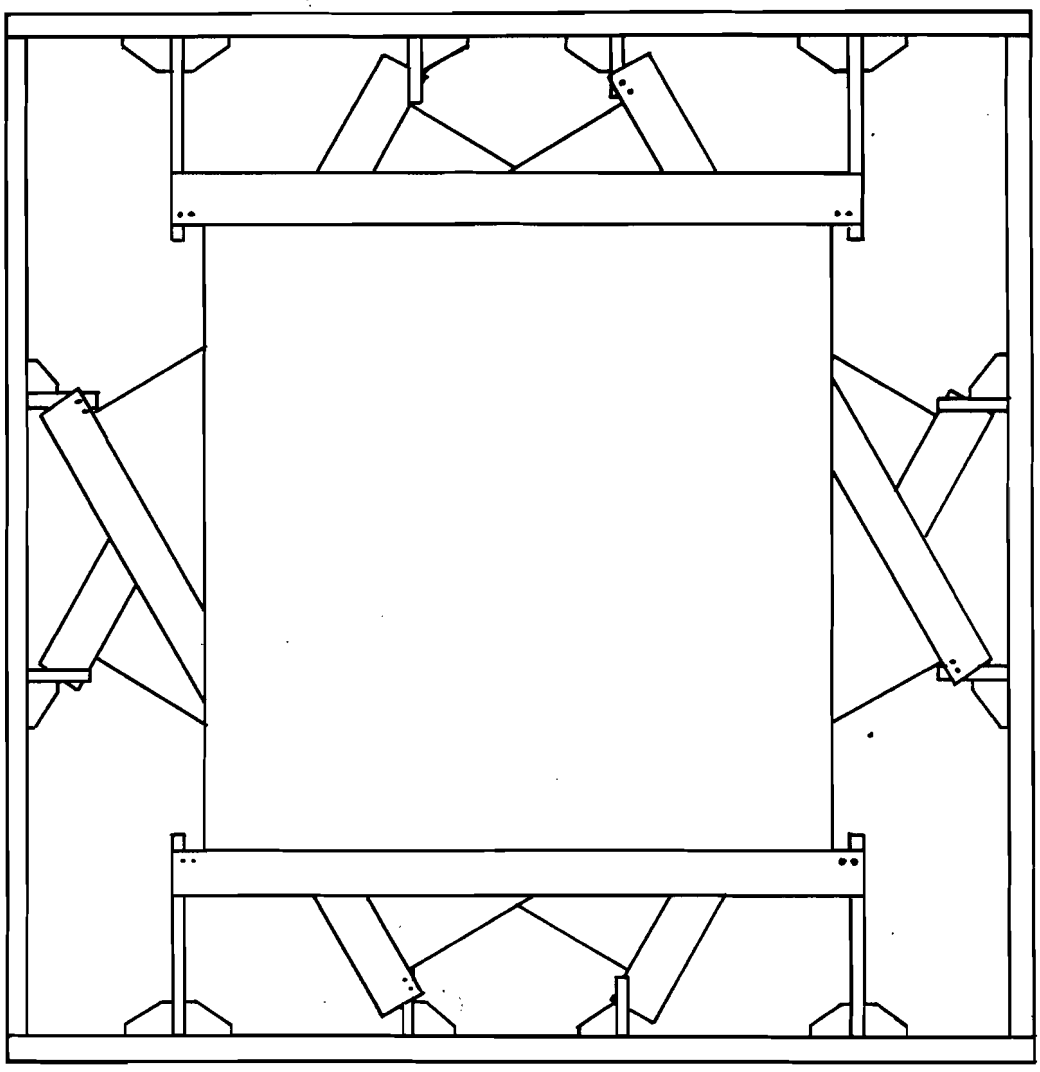

Figure A-4

The P-tube frame

named the X, U, and V planes for the directions which they measured. The U plane was rotated $+60.0^{o}$ from the X axis and the V plane was rotated -60.0^{o} from the X axis taking the definition of positive angle as being from the positive X-axis to the positive Y-axis. The entire P-tube array fit within the 4" thick steel channel which encased it. The associated electronics for the P-tubes (the RIRODAC system, for Read-In, Read-Out Analog-Digital Convertor) was attached to the east side of the steel box and the gas system for the P-tubes was located on top of the steel hadron absorber.

The tubes themselves were constructed of 28 mil thick seamless aluminum and were cleaned extensively before each plane was assembled. The gas mixture used in the tubes was 50% argon, 50% ethane and was provided by a bubbler system for each set of 30 P-tubes. Two calibration systems existed for the P-tubes: an on-line computer-controlled charge injection system to test the P-tube electronics, and an off-line system which consisted of a single short P-tube with a thin spot machined into its side so that gamma rays from a Fe-55 source could penetrate the tube and provide a constant energy spectrum calibration source with which the gas composition and pressure could be monitored, using a pulse height spectrum as shown on a LeCroy Model 3001 qVt multichannel analyzer.

The longitudinal lead glass array and the steel box in which it was enclosed were built by the University of Illinois and Fermilab. The lead glass blocks consisted of a 10 X 10 array of three different types of blocks: 47 blocks purchased by the University of Illinois from Sovirel in France (a subsidiary of Corning Glass) with dimensions of 15.0 cm X 15.0 cm X 46.0 cm (Figure A-5); and 51 blocks on loan to our experiment from an earlier Fermilab experiment (E288—Lederman et. al., 1977) of two different dimensions, 27 dubbed "long Lederman" blocks of 14.7 cm X 14.7 cm X 46.0 cm and 24 dubbed "short Lederman" blocks of 14.7 cm X 14.7 cm X 40.0 cm. The characteristics of the University of Illinois and Lederman blocks are given in Tables A-2 and A-3. Also, there was a hollow aluminum "beam block" though which the beam could pass of outer dimensions 15.0 cm X 15.0 cm X 45.0 cm and inner dimensions 13.7 cm X 13.7 cm X 45.0 cm (Figure A-6). Between every pair of columns and on the sides of the array, a sheet of Co-netic material of dimensions 60.0" X 30.0" X 30 mils (Perfection Mica Company 1976) was inserted to mitigate magnetic effects on the photomultiplier tubes. The entire array was then enclosed in a steel box constructed by the Fermilab shop. This box rode atop a large steel base with four industrial rollers placed in such a way that the array and P-tubes attached to the front could be winched east or west perpendicular to the beam line (Figure A-7).

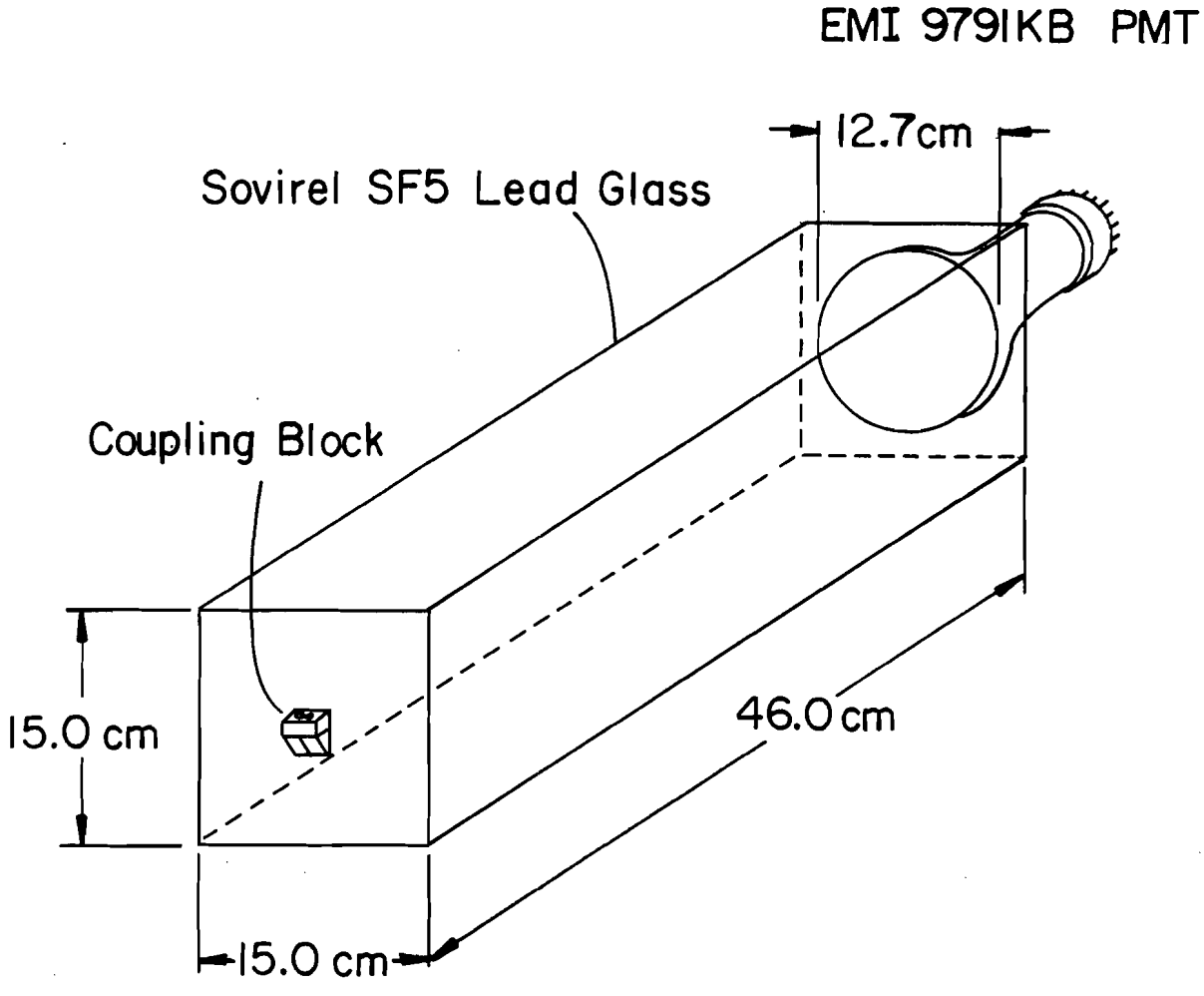

Figure A-5

Longitudinal lead glass block assembly

(some blocks have other dimensions and phototubes

as explained in the text)

Manufacturer: Sovirel (Corning)

Glass Type: SF5 (CEREN25)

Composition: SiO_2 39%

PbO 55%

K_2O 2%

Na_2O 3%

Radiation Length: 2.51 cm

Refractive Index: 1.669

Specific Gravity: 4.06

Coefficient of Thermal Expansion:

74×10^{-7} (-30° to $+70^{\circ}$ C.)

Internal Transmittance/25 mm

Wavelength (nm)	Transmittance
350	0.412
360	0.672
370	0.823
380	0.877
390	0.913
400	0.954
420	0.982
440	0.984
460	0.987
480	0.991
500	0.994

Table A-2

University of Illinois lead glass blocks' characteristics

Manufacturer: Ohara

Glass Type: SF5 (Ohara 673321)

Composition: PbO 55%

SiO_2 38%

K_2O 5%

Na_2O 1%

Radiation Length: 2.36 cm

Refractive Index: 1.67270

Specific Gravity: 4.08

Coefficient of Thermal Expansion:

85×10^{-7} (-30° to $+70^{\circ}$ C.)

Internal Transmittance/25 mm

Wavelength (nm)	Transmittance
340	0.02
350	0.27
360	0.57
370	0.75
380	0.85
390	0.92
400	0.95
420	0.975
440	0.98
500	0.99
700	0.993

Table A-3

Lederman lead glass blocks' characteristics

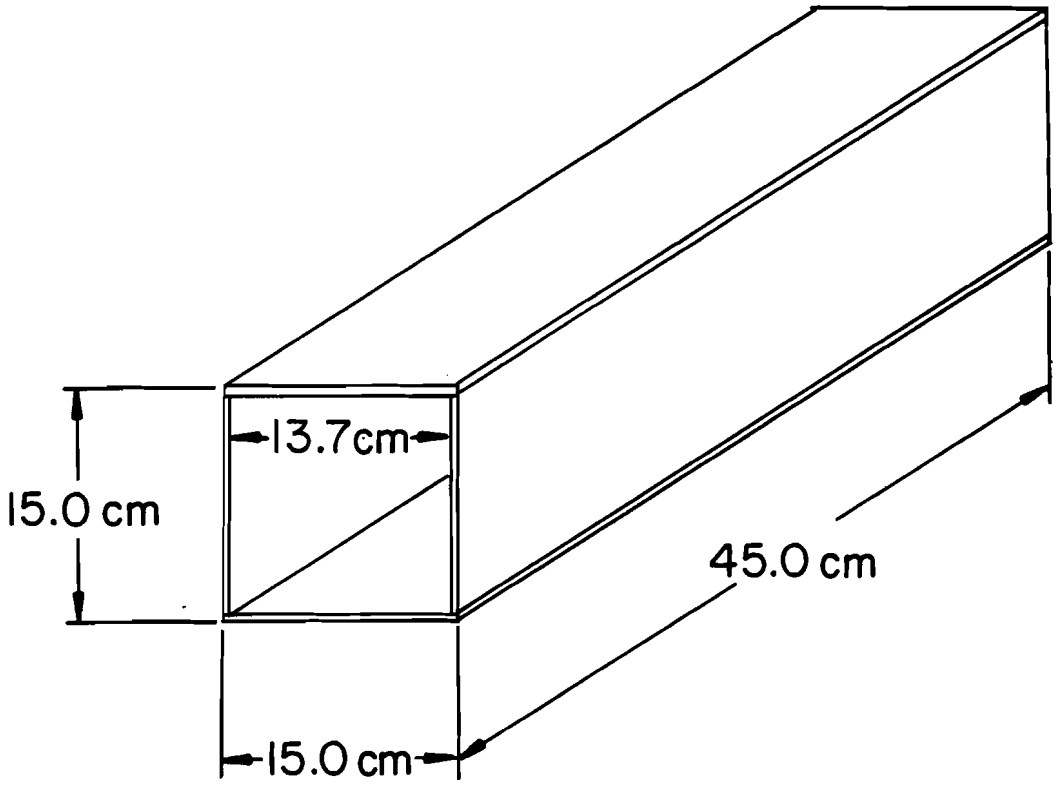

Figure A-6

The beam block

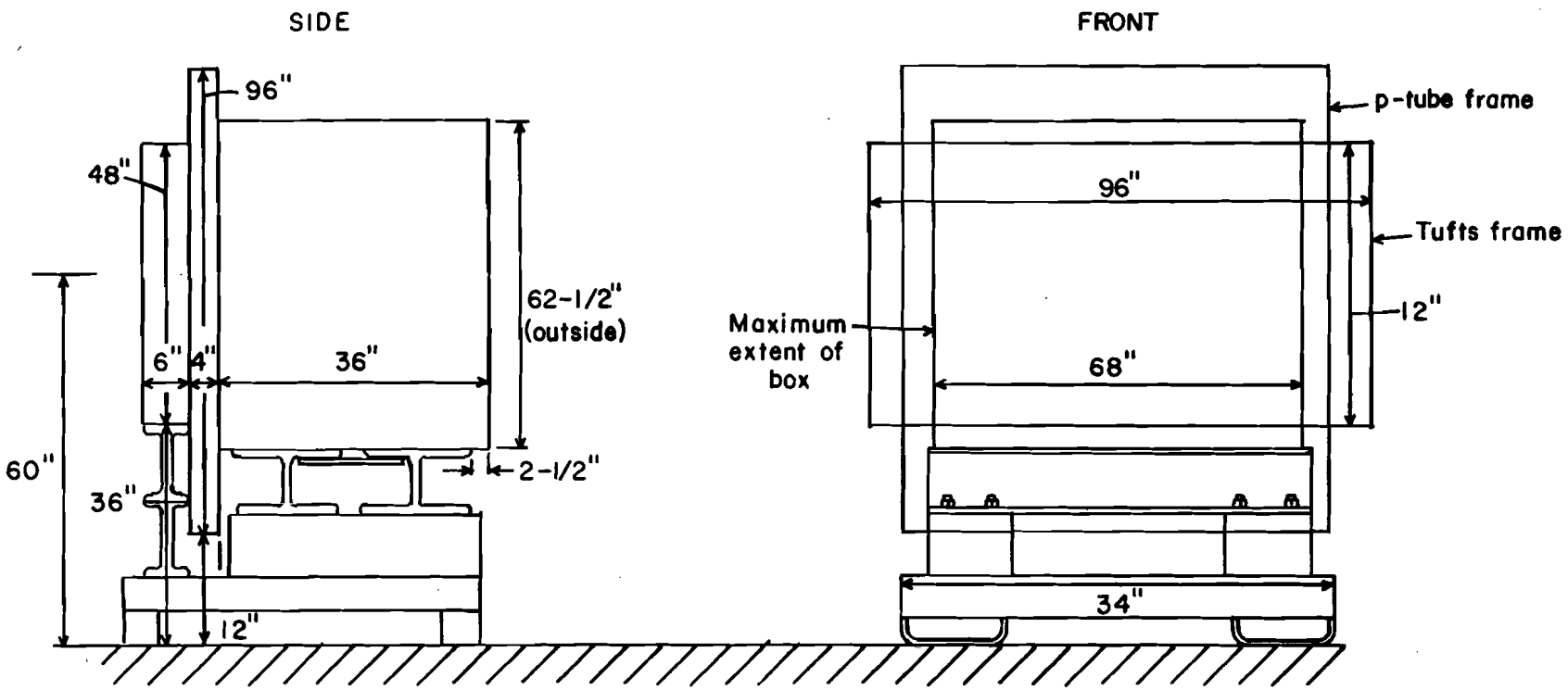

Figure A-7

The lead glass box

The blocks all had more or less the same construction. The "Lederman" blocks arrived already assembled although many of these blocks had to be repaired or rewrapped entirely; the "Illinois" blocks' construction was based on the "Lederman" design. The "Lederman" blocks used RCA 4525 photomultiplier tubes; the "Illinois" blocks used EMI 7971KB photomultiplier tubes. For new assembly Kodak HE-110 optical assembly epoxy was used throughout; this cement had the advantages that it had an index of refraction intermediate between that of the lead glass and the glass face of the photomultiplier tube, it was resilient and thus immune to thermal expansion problems, and it could be removed by carefully cycling a block up to around 200 F for removal of a damaged photomultiplier tube. The new tubes were centered and glued on one end of the new lead glass blocks and the coupling block assembly was centered and glued to the opposite end. 1 mil greaseless aluminum foil was molded around the photomultipler tube and wrapped about the block, followed by a layer of 5 mil clear mylar around the block, and then by a layer of 6 mil black polyethylene; the first to be held at the same negative high voltage as the photocathode for electrostatic shielding, the second as an insulator to prevent any leakage of the high voltage, and the third to keep the block light-tight. The entire assemblage was held together with electrical tape. The aluminum foil was held at the same high voltage as the photocathode through a 3 MΩ, 1/16 W resistor.

Each lead glass block had a coupling block assembly epoxied to the end of the block opposite the phototube (Figure A-8). This consisted of a coupling block and two prisms arranged such that light from the LED and argon flash lamp light fiber could be totally internally reflected at a 45° angle into the lead glass block toward the phototube.

Figures A-9 and A-10 show the designs of the phototube bases for the University of Illinois phototubes and the Lederman phototubes. As with the transverse blocks' phototube base, the resistor chains are "tapered" so that higher voltages are present across the last few dynode stages. This tapering helps prevent signal loss at high rates. The University of Illinois design, in addition, has emitter follower circuits present in the last four stages to clamp the volatges at set values despite large current conditions during high rates. The University of Illinois blocks' phototubes typically run at a high voltage of -1000 V, while the Lederman ran at about -1200 V and the transverse blocks operated at about -1500 V.

A major problem with the lead glass array was reducing the magnetic field. With the CCM on, the field strength in the vicinity of the lead glass box was 14 G. Even the Earth's field of about 0.5 G can cause a 30% reduction in some phototubes in some orientations. In addition to encasing the longitudinal blocks in a box of "cold-rolled"

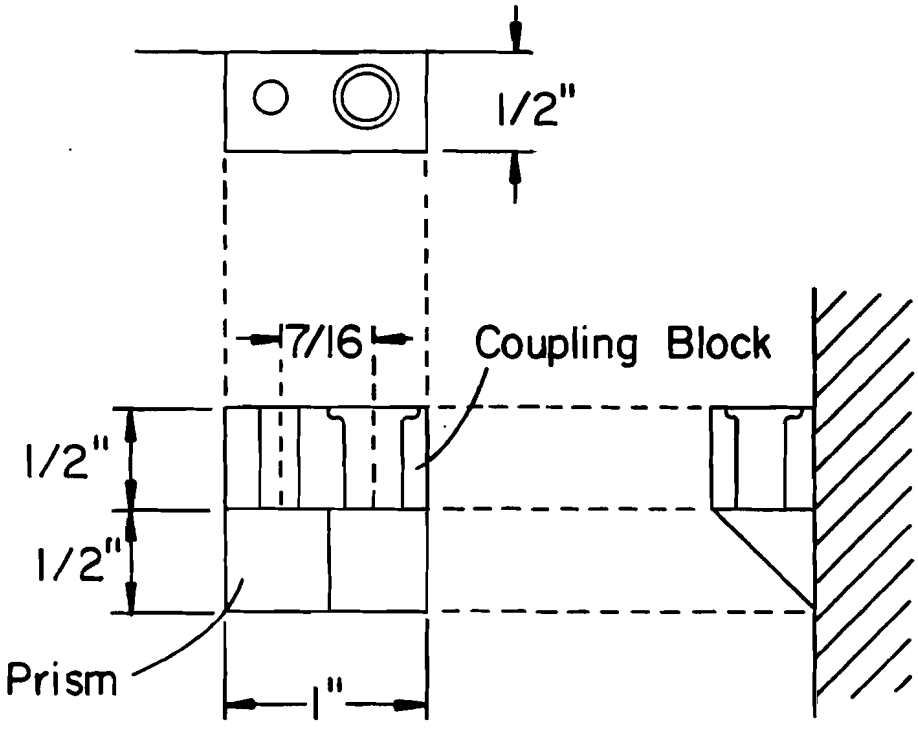

Figure A-8

The coupling block assembly

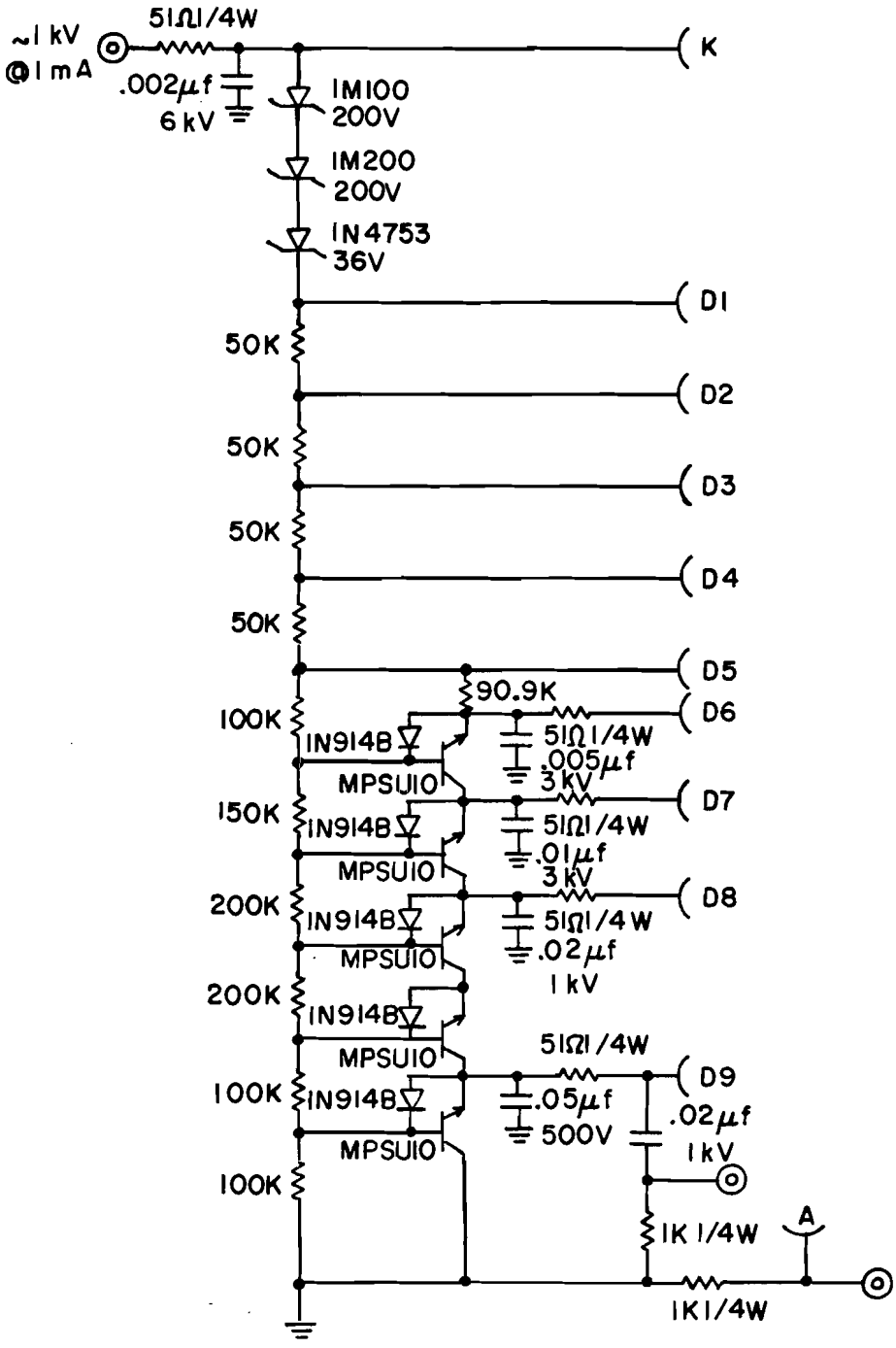

Figure A-9

University of Illinois lead glass photomultiplier base

(for use with EMI 9791KB phototube)

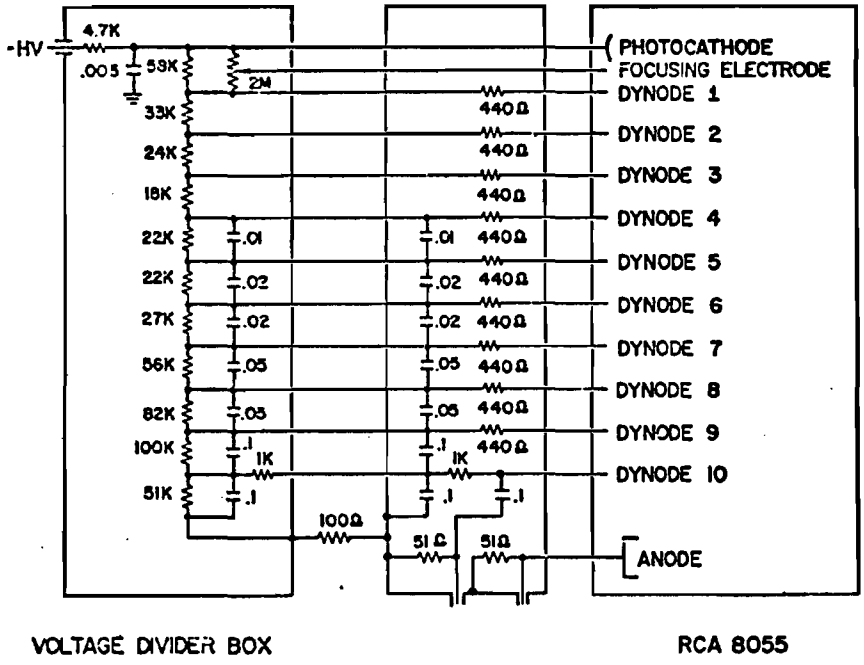

Figure A-10

Lederman lead glass photomultiplier base

(for use with RCA 4525 phototube)

steel with better magnetic susceptibility than normal steel, and the Co-netic sheets between columns mentioned earlier, each block had a Co-netic cylindrical shield which fit over the phototube, and then, to extend the shielding beyond the photocathode, soft Co-netic shielding was wrapped around the block and the cylinder. Even with all these efforts, some blocks were found to have lost 20% of their pulse height between magnetic field on and magnetic field off. A last improvement to the array was built to counteract the magnetic field--a pair of large bucking coils (Figure A-11). This consisted of two rectangular frames of steel channel containing 20 turns of 1/4" square cross section copper wire each. One frame was clamped below the lead glass box and one frame above it. A high current, low voltage power supply was used to provide 30 A of current which produced a field of 14 G opposite in direction to that produced by the CCM at the center of the lead glass array. The effects of the bucking coils on the resolution of the lead glass are discussed in Chapter 4.

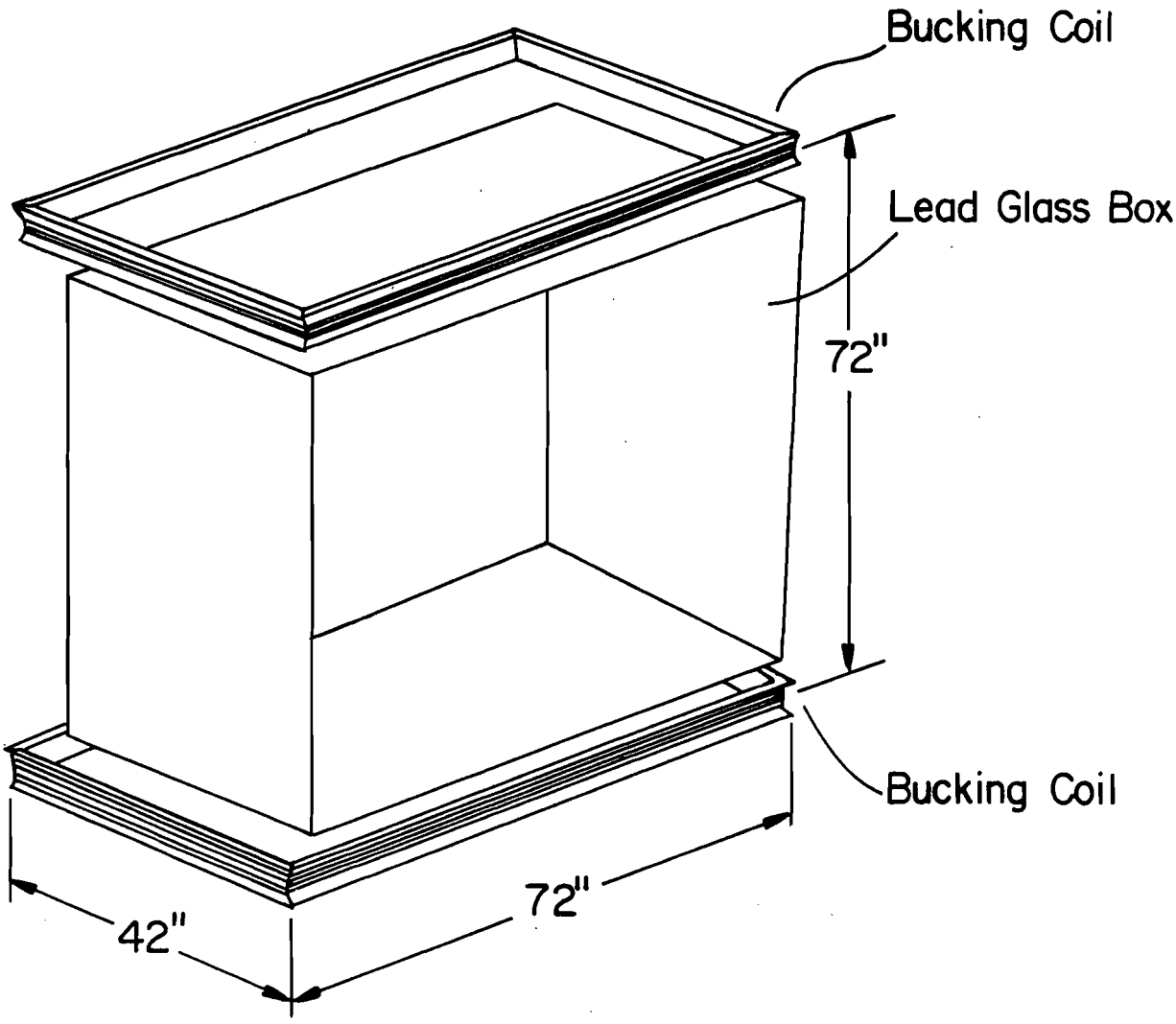

Figure A-11

Lead glass array bucking coils

Appendix B

The On-line Computers and Associated Electronics

The experiment was under the control of two computers: a PDP-11/45 and an LSI-11. The PDP-11/45, using the program RTMULTI, gathered the data directly from the CAMAC crates and from the LSI-11 via a buffered CAMAC-to-CAMAC link; this data was then logged to tape and analyzed on-line during idle time. The LSI-11 gathered the data from the lead glass array; thus, this large volume of data could be transferred in parallel with the data from the other apparatus being piped directly into the PDP-11/45.

RTMULTI is a general-purpose program for gathering and analyzing data in high-energy experimental applications, written first at the California Institute of Technology and then improved by the Fermilab staff (Fermilab 1978,1980). The structure of the tape records and the order of data acquisition are list-driven; this makes changes possible without rewritting the program itself. The user can, via interactive commands at the keyboard or indirect command files, define calculated quantities, histograms, plots, and quantities to be watched, so that if the quantity falls outside set limits an alarm (usually, a beep at the keyboard) is raised. Logging the events to tape is always accorded the highest priority, so only those events

which can be handled during the time the computer is idle are analyzed with regard to whatever the user has defined.

The computer was triggered by interrupts to the Bison Box (HN-25; HN-3?)—a customized Fermilab unit for use by experimenters. This box consisted of two interrupt inputs designated Interrupt A and Interrupt B, an input register and output register to the computer, and indicative LED's so the user could see the current state of the Bison Box. In our case, Interrupt A was used to indicate a begin-run event or an actual event, Interrupt B was used to indicate a between-spill event, and the output register was used to indicate to the logic what the current state of the trigger was. This is explained in detail in Appendix C.

In addition to the above, specialized routines were written for inclusion in RTMULTI. These provided event displays of the apparatus: plan views in x or y of the entire or selected portions of the apparatus; and views along the z-axis of the lead glass array or any hodoscope. These views showed pulse heights and hits, as well as the outlines of the detectors displayed. The raw contents of a single event could be dumped in its entirety or only selected portions. Most importantly, statistics over an entire tape or a selected portion of a tape could be accumulated in the so-called EPIC report. This report included the accumulated scaler statistics and multiplicity

distributions into every hodoscope element (including the Cerenkov counter and lead glass array) and every MWPC chamber wire and drift chamber cell. Thus, at a glance, dead wires or elements could be recognized.

As stated before, RTMULTI is a list-driven program. This means changes to the behavior of the program can be made without changing the program itself, but instead changing the contents of the files the program accesses. The most inportant such list is the file CAMAC.DEF which contains the procedure for data acquisition from the CAMAC crates used in the experiment. The details of how this list is used are contained in the Fermilab MULTI User's Guide (Fermilab, 1978). As an introduction to the internal workings of RTMULTI and an explanation of how our experiment used the PDP-11/45 to read in the data, we list our CAMAC.DEF file in Table B-1. This list also demonstrates the tape record format of our raw data tapes because the buffer from which the tape records were written was filled exactly in the order in which the CAMAC.DEF file directed.

Lines beginning with an exclamation mark are comments and are ignored by RTMULTI. The first three executable lines of the CAMAC list define parameters important to RTMULTI: the "BUFFERS" statement defines a maximum buffer size of 4095 words (16 bits/word on the PDP-11/45) with no buffers in regular memory and 16 buffers in dynamic

```
! CAMAC FILE FOR E610
      BUFFERS 4095,0,16        !DEFINE BUFFERS
      CRATES  1,2,3,4,5,6      !DEFINE CRATES
      LAMLAT  1,1              !DEFINE LAM-LATCH
!
! INTERRUPT "A" LIST:
      BEGIN   2495,,(1,2,3,4,5) !DEFAULT FL1-5 ON
      CALL    DAUSR1           !FILL IN 5 EVENT INFO WORDS
!
      BCOUNT                   !START OF FIXDAT #1 GROUP
      IF      FLG EQ 0,100,(1) !SKIP IF FL1 OFF
      FIND    145,REL          !SKIP 145 WORDS (FILL IN LATER)
! READ PB GLASS ADC'S (156) + CERENKOV ADC'S (24)
      TRANS   2,2,1,0,174,,,,XR,QR,XQ,EL
      TRANS   2,2,17,0,6,,,,XR,QR,XQ,EL
      FCNA    9,2,26,0,XR      !CLEAR WHOLE ADC CRATE
      WRITE   17,1,2,0,"2,QR   !PULSE BIT 1 OF ND027 TO FLASH LED'S
      FIND    0,OLD            !GO BACK TO POSITION AT LAST "FIND"
```

Table B-1

CAMAC.DEF list driver

```
! READ SCALERS (32, OR 64 WORDS)
      TRANS   0,4,1,0,32,,,,XR,QR,XQ,EL,LW
! READ LATCHES (9) AND TDC'S (72)
      TRANS   2,3,1,0,81,,,,XR,QR,XR,EL
      FIND    0,OLD           !POSITION TO END OF EVENT
! READ PB GLASS ADC'S (156) + CERENKOV ADC'S (24)
      TRANS   2,2,1,0,174,,,,XR,QR,XQ,EL
      TRANS   2,2,17,0,6,,,,XR,QR,XQ,EL
100   ECOUNT                  !END OF FIXDAT #1 GROUP
!
      BCOUNT                  !START OF FIXDAT #2 GROUP
      IF      FLG EQ 0,200,(2) !SKIP IF FL2 OFF
      FIND    603,REL         !SKIP 603 WORDS (FILL IN LATER)
200   ECOUNT                  !END OF FIXDAT #2 GROUP
!
      BCOUNT                  !START OF NANOMAKER DATA
      IF      FLG EQ 0,300,(3) !SKIP IF FL3 OFF
! READ NANOMAKER DATA FOR 6 MODULES
```

Table B-1 (continued)

CAMAC.DEF list driver

```
      TRANS   2,5,12,0,390,,,,CO,BB,XQ
300   ECOUNT                    !END OF NANOMAKER DATA
!
      BCOUNT                    !START OF UI DATA
      IF      FLG EQ 0,400,(4)  !SKIP IF FL4 OFF
      FCNA    4,5,2,0,XR        !PREPARE FOR UI READ-OUT
! READ U OF I DATA FOR 15 PLANES
      TRANS   2,5,2,0,4095,,,,BB,BM,XR,TR
400   ECOUNT                    !END OF UI DATA
!
      SET     Z=0               !COUNT OF MUTES DMA'S
      IF      FLG EQ 0,500,(5)  !SKIP IF FL5 OFF
450   FCNA    14,6,26,0,XR      !"SRO" COMMAND TO ALL STATIONS
      BCOUNT                    !START OF MUTES DMA GROUP
! READ MUTES DATA GROUPS FROM 8 MODULES
      TRANS   2,6,4,0,264,,,,BB,XQ,CO,LW,TR
      ECOUNT                    !END OF MUTES DMA GROUP
      IF      BCT EQ 0,500      !IF NO DATA READ LAST TIME, DONE
```

Table B-1 (continued)

CAMAC.DEF list driver

```
        SET     Z=Z,1           !COUNT ANOTHER DMA
        IF      BCT GT 32,450   !LOOP UNTIL 8 OR LESS 24-BIT WDS READ
!
500     IF      FLG EQ 0,600,(2) !SKIP IF FL2 OFF
        SET     X=10000         !LSI TIME OUT
510     FCNA    1,1,3,0,XR,QR,XQ !TEST LSI READY
        IF      DLO NE 0,520    !READY NOW
        SET     X=X,-1          !COUNT DOWN
        IF      X GT 0,510      !LOOP UNTIL UNDERFLOW
        SET     ERR=ERR,1       !FLAG ERROR
        GOTO    600
520     FIND    0,OLD           !POSITION TO LAST "FIND"
! READ LSI--600 PTUBE, 3 TRAILERS
        TRANS   2,1,3,0,603,,,,XR,QR,XQ,BB,BM,EL
        FIND    0,OLD           !POSITION TO END OF EVENT
        FCNA    14,1,3,0,XR     !CLEAR LSI READY BIT
!
600     FIND    10              !POSITION TO WORD 10
```

Table B-1 (continued)

CAMAC.DEF list driver

```
      PUT     Z                 !WRITE OUT MUTES DMA COUNT THERE
      FIND    0,OLD             !GO BACK TO END OF EVENT
      FCNA    26,2356,28,9,XR   !DATAWAY C ON CRATES 2-3-5-6
      WRITE   17,1,2,0,"5,QR    !PULSE BIT 0 AND 2 OF NIM DRIVER
      END                       !END OF LIST "A"
!
! INTERRUPT "B" LIST:
      BEGIN   3995,,(1,2)       !DEFAULT FL1-2 ON
      CALL    DAUSR1            !FILL IN 5 EVENT INFO WORDS
!
      BCOUNT                    !START OF FIXDAT #1 GROUP
      IF      FLG EQ 0,1100,(1) !SKIP IF FL1 OFF
      FIND    107,REL           !SKIP 107 WORDS (FILL IN LATER)
! READ PB GLASS ADC'S (156) + CERENKOV ADC'S (24)
      TRANS   2,2,1,0,174,,,,XR,QR,XQ,EL
      TRANS   2,2,17,0,6,,,,XR,QR,XQ,EL
      FCNA    9,2,26,0,XR       !CLEAR WHOLE ADC CRATE
      WRITE   17,1,2,0,"2,QR    !PULSE BIT 1 OF ND027 TO FLASH LED'S
```

Table B-1 (continued)

CAMAC.DEF list driver

```
      FIND    0,OLD           !GO BACK TO POSITION AT LAST "FIND"
! READ SCALERS (32, OR 64 WORDS)
      TRANS   0,4,1,0,32,,,,XR,QR,XQ,EL,LW
      CALL    DAUSR2,MAP      !SUM UP SCALER DATA & READ 036 DATA (43
WDS)
      FIND    0,OLD           !POSITION TO END OF EVENT
! READ PB GLASS ADC'S (156) + CERENKOV ADC'S (24)
      TRANS   2,2,1,0,174,,,,XR,QR,XQ,EL
      TRANS   2,2,17,0,6,,,,XR,QR,XQ,EL
1100  ECOUNT                  !END OF FIXDAT #1 GROUP
!
      BCOUNT                  !START OF FIXDAT #2 GROUP
      IF      FLG EQ 0,1200,(2) !SKIP IF FL2 OFF
      SET     X=10000         !LSI TIME OUT
1110  FCNA    1,1,3,0,XR,QR,XQ !TEST LSI READY
      IF      DLO NE 0,1120   !READY NOW
      SET     X=X,-1          !COUNT DOWN
      IF      X GT 0,1110     !LOOP UNTIL UNDERFLOW
      SET     ERR=ERR,1       !FLAG ERROR
```

Table B-1 (continued)

CAMAC.DEF list driver

```
      GOTO    1200
! READ LSI -- 200 DVM, 3 TRAILERS
1120  TRANS   2,1,3,0,203,,,,XR,QR,XQ,BB,BM,EL
      FCNA    14,1,3,0,XR      !CLEAR LSI READY BIT
1200  ECOUNT                   !END OF FIXDAT #2 GROUP
!
      FCNA    26,23456,28,9,XR !DATAWAY C ON CRATES 2-3-4-5-6
      WRITE   17,1,2,0,"1,QR   !PULSE BIT 0 OF NIM DRIVER (RESET)
      END                      !END OF LIST "B"
```

Table B-1 (continued)

CAMAC.DEF list driver

memory; the "CRATES" statement declares that all CAMAC crates 1 through 6 are active; and the "LAMLAT" statement defines the location of where the LAM latch module entered the CAMAC crates, in this case address #1 of CAMAC crate #1. The PDP-11/45 which we used was provided with 48K words of regular executable memory in which RTMULTI resided during normal running and 64K words of non-executable dynamic memory where RTMULTI variables and the data buffers were stored. The "LAM latch" is a push-button box which connects to a single-width CAMAC module through which the user may send an interrupt to the computer. In RTMULTI, it is used to send RTMULTI instructions to the program without actually typing them in on the keyboard. The connection between the 16 push-buttons and the RTMULTI instruction which they represent is made by another list, MENU.DEF.

The rest of the CAMAC.DEF file defines exactly what actions are taken if either of the two interrupts, Interrupt A or Interrupt B, is input at the Bison Box. The first set of instructions between the "BEGIN" command and the "END" command delineate the actions for an Interrupt A; while the second such set of instructions delineate the actions for an Interrupt B. The "BEGIN" command for an Interrupt A defines the maximum record size as 2495 words and sets the default for flags #1 through #5 as being "on". The records are variable length, and are stored contiguously in the data buffers; however, they do not overlap data buffers. Thus, the number of records in a data buffer is

variable depending on their lengths. RTMULTI automatically fills the first five words of every data record with the following information: data record byte count (2 bytes/word), data record type (1 if an Interrupt A; 2 if an Interrupt B), run number, two-word record sequence number. The "CALL" command instructs RTMULTI to pass control momentarily to subroutine DAUSR1, which fills in the next five words of the data record with the following data: one word of the current date, two words of the current time, one word containing a bit string of the flag bits, and one word containing the number of MUTES DMA (data mass access?) blocks, as will be explained later.

The data records were further divided internally into "blocks". Each block began with a word stating how long the block was while the remainder of the block contained the actual data for a logical group of connected information. The CAMAC.DEF instructions which delineated the definition of a block were "BCOUNT" and "ECOUNT". At all times, RTMULTI maintains a pointer into the data buffer of its current location which is incremented after each operation. Thus, up to this point, RTMULTI has filled in the first ten words of a data record and the pointer is now pointing at the eleventh word. A "BCOUNT" command tells RTMULTI to remember the current location but skip to the next location for the next instruction. When the "ECOUNT" instruction is encountered, RTMULTI inserts in the remembered location the number of words written since the "BCOUNT" instruction, thus defining the size

of the block, and then returns the pointer to the word after the end of the block.

The blocks defined for an Interrupt A record were: the FIXDAT #1 block containing fixed length data from the ADC's, the scalers, the latches, and the TDC's; the FIXDAT #2 block containing the fixed length data from the P-tube ADC's via the LSI-11; the NANOMAKER block containing the variable length data from the 80 cm MWPC's; the UI block containing the variable length data from the U of I MWPC's; and a variable number of MUTES DMA blocks each containing a variable length of data from the drift chambers.

Returning to the CAMAC.DEF list and the "BCOUNT" instruction for the FIXDAT #1 block to begin, the next instruction is an "IF" command which instructs RTMULTI to skip to the line labeled 100 if the flag FL1 (indicated by the 1 in parentheses; actually, the least significant bit in the flag register word) is equal to zero or "off". Such an "IF" statement is located directly after the beginning of each block; thus, if a certain CAMAC flag is off, a corresponding block of data is not entered into the data buffer. This is accomplished by skipping directly to the "ECOUNT" statement such that the data block in question is represented by a single word containing a data block word count of one--the word itself. The "FIND" command moves the current word pointer 145 words further relative to the current

position but also stores the old position for retrieval later. The two "TRANSFER" (shortened to "TRANS") commands following execute a CAMAC DMA transfer; the parameters send CAMAC a function code 2 (read) from crate 2, station 1, subaddress 0 for 174 words followed by another read from crate 2, station 17, subaddress 0 for 6 words. The various parameters at the end of the command list tell RTMULTI to return an error if there is no "X response" or "Q response" or if the number of addressed words read does not equal the exact number demanded. The "X response" is a CAMAC response indicating the unit is present; the "Q response" indicates that the unit's data is digitized and ready for transferral. These commands read in all the ADCed information which was digitized in CAMAC crate #2: the 156 lead glass ADC's and the 24 gas Cerenkov ADC's (not all channels were actually used). The "FCNA" instruction (an old CAMAC mnemonic for "Function, Crate, statioN, and subAddress") following sends a function 9 (clear) to the CAMAC crate controller in crate #2, station 26, subaddress 0 which zeroes all the ADC channels and prepares them for another gate and digitization. A "WRITE" (function 17) is then sent to crate #1, station 2, subaddress 0 to pulse the EG&G ND027 single-bit register NIM driver which initiates the "quick calibration" sequence as explained in Appendix C. While waiting for the "quick-cal" sequence to finish and the data to be digitized, the scalers, latches, and TDC's in crates #3 and #4 are read into the 145 words previously

skipped over. First, the "FIND" returns the current word pointer back to the stored location and also stores the location where the pointer is before restoration; then the "TRANFER" commands read the data into the data buffer. The "LW" parameter on the "TRANSFER" for the scalers states that these are long CAMAC words of 24 bits each instead of 16 bits which will be stored in the data buffer as two 16-bit words. By the time this data transferral is complete, the "quick-cal" sequence is also done and the ADCed information is ready to be read in again. This is accomplished by the "FIND", which returns the current word pointer back to the end of the data record, followed by the two "TRANSFER" statements.

The FIXDAT #2 block of 603 words is simply skipped for the moment, again using a "FIND" command, if the flag FL2 is "on". The NANOMAKER scanners are read into the next block if flag FL3 is "on". This is effected by using a "TRANSFER" statement with a CAMAC function code 2 (read) on crate #5, station 12, subaddress 0 for up o 390 words. The parameters at the end of the command tell CAMAC to read from a NANOMAKER scanner module until the "Q response" goes from an on to an off state, indicating the data from that module is exhausted, and then proceed to the next module in the crate up to the last module in the crate.

The U of I chambers' data is read into the next block if CAMAC flag FL4 is "on". The readout sequence is initiated by a "FCNA" command sending a CAMAC function code 4 (initiate) to crate #5, station 2, subaddress 0;] when the U of I readout module is ready it returns the "X response" which allows the next instruction to be executed. This is a "TRANSFER" with CAMAC function code 2 (read) to the same module and for up to 4095 words; the parameters at the end of the command tell CAMAC to keep reading from the same station and address until the "Q response" goes from an "on" state to an "off" state, truncating the data if it reaches the maximum record size.

The MUTES readout sequence was more complicated. Z is a general purpose register, first "SET" to zero, used to count the total number of MUTES DMA blocks. If CAMAC flag FL5 is "on" a "FCNA" is sent with CAMAC function code 14 (start readout) to the CAMAC crate controller in crate #6, station 26, subaddress 0. Then a read is initiated by a "TRANSFER" command with function code 2 (read) to crate #6, station 4, subaddress 0 for a maximum of 264 "long" (24 bits) words. The parameters also allow for truncation of the data if it would overflow the data record maximum size and for advancing to the next module when no "Q response" is received. Each such read constitutes one MUTES DMA block; after which, general purpose register Z is incremented and the process repeated until a read of less than or equal to 32 24-bit words occurs. This is all accompilshed via the "IF" and "SET" commands

between the lines labeled 450 and 500.

At this point, the CAMAC list returns to the task of filling the P-tube ADC data received from the LSI-11 if the CAMAC flag FL2 is "on". The data was transferred between the LSI-11 and the PDP-11/45 through a pair of twisted cable connected CAMAC data buffer modules. Because the transfer rate was slow, a time-out loop was established in the CAMAC list using general purpose register X. This register was counted down from 10,000 every time the LSI-11 did not test ready as determined by a "FCNA" command with function code 1 (read) to crate #1, station 1, subaddress 0. This command reads a single word from the CAMAC module into the CAMAC registers DLO and DHI. If DLO was found to be non-zero, then the CAMAC data buffer module on the PDP-11/45 was filled and ready to be read. If the entire count-down proceeded without the module ever found to be ready, then the error flag was "SET" and the readout of the LSI-11 information was skipped. Otherwise, the current word pointer is reset to where 603 words were previously skipped and the P-tube ADC values from the CAMAC data buffer module are filled into the data record via a "TRANSFER" with a CAMAC function code 2 (read) to crate #1, station 3, subaddress 0 for exactly 603 words all received from the same station and subaddress. The current word pointer is repositioned to the end of the data record with the "FIND" command and a clear is sent to the CAMAC data buffer module using a "FCNA" command with a CAMAC function code 14 (clear) to

the same station and address as before in crate #1. Finally, the current word pointer is positioned to the tenth word of the record with the "FIND" command, the number of MUTES DMA blocks is written into this word from general purpose register Z with the "PUT" command, the current word pointer is again repositioned to the end of the data record, a clear is sent to crates #2, #3, #5, and #6 with a "FCNA" command with a function code 26 (dataway clear) to station 28 and subaddress 9 in the CAMAC crate controllers, and bits 0 and 2 of the EG&G single-bit register NIM driver are pulsed with a "WRITE" command to crate #1, station 2, subaddress 0 to reset the logic and the apparatus readout electronics as explained in Appendix C.

The blocks defined for an Interrupt B record were: the FIXDAT #1 block containing fixed length data from the ADC's, the scalers, and the MAC 036 module; and the FIXDAT #2 block containing the fixed length data from the high-voltage CAMAC-readable DVM via the LSI-11. The "BEGIN" command allows a maximum data record length of 3995 words for an Interrupt B record. Note that the creation of the FIXDAT #1 block for the Interrupt B record proceeds exactly as with the Interrupt A record except for the "CALL" to subroutine DAUSR2 which calculated cumulative and spill-by-spill totals for the scalers and made the necessary CAMAC calls to a special module to read in the desired MAC data (beam line data) from the MAC 036 module. Then, the subroutine writes this data out to the data record and returns control

to RTMULTI and the CAMAC list. Thus, whereas an Interrupt A record has all the signals during an event of the ADCed and TDCed information, the Interrupt B record has the pedastals as found during no activity between spills. Likewise, the Interrupt A record has the cumulative scaler data; the Interrupt B record has the scaler data since the last spill and the magnet values read from the MAC crates. The FIXDAT #2 data is read in from the LSI-11 data buffer module as the P-tube ADC data was read in for the Interrupt A record. Now this data buffer contains the DVM readout values for the lead glass high voltages—a total of 203 values. Again, all the crates but #1 are cleared and the logic is reset.

Appendix C

The Trigger Logic

Almost all the logic was created in the logic NIM bins (Standard Nuclear Instrument Modules, 1974): one located in the upstream area above the U of I MWPC electronics, one located atop the steel hadron absorber near the M hodoscope, and several in the main electronics racks. LeCroy NIM units were used extensively (LeCroy, 1973-1978); also, LeCroy and custom-built CAMAC units in the CAMAC crates were gated, triggered, or reset by logic inputs as will be illustrated. A few custom units were also used in the logic: the PPPP delay unit—a custom-built Fermilab unit—to set the delays and gates to the ADC's; the MAC CAMAC single-bit register unit ND027 (Fermilab, 1974) to initiate calibration sequences and reset electronics at event completion; and the Bison Box (Fermilab, 1974) by which the computer was interrupted by the event trigger and by which the computer communicated the current trigger to the logic. All logic signals were negative NIM signals—i.e., logical "0" = 0 mV into 50 ohms and logical "1" = -800 mV into 50 ohms.

The heart of the trigger logic is shown in Figure C-1. The event trigger ("master trigger" or MT) was (Begrun A)+(Begrun B)+T. Begrun A and Begrun B are triggers to initiate calibration sequences and will be described later. T ("trigger") is the normal event trigger and is

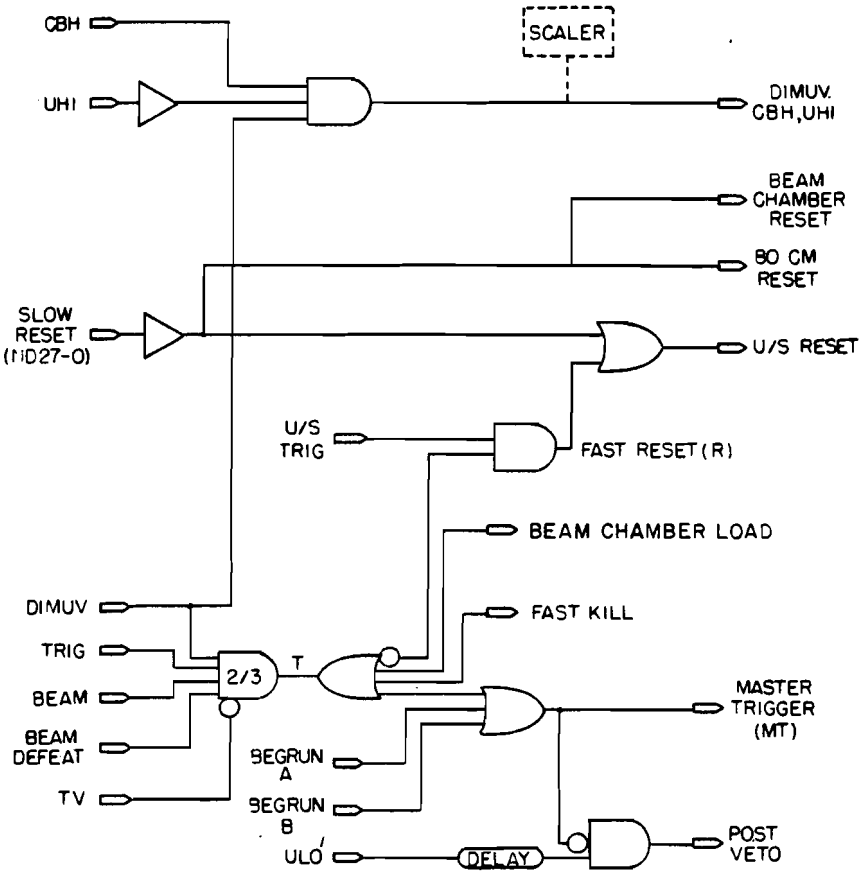

Figure C-1

Master trigger logic

formulated in a 4-fold majority logic unit with veto (LeCroy NIM Model 365AL; all logic signals are negative NIM signals unless otherwise specified). This unit could be set to accept any combination of 4 inputs and output a pulse if N inputs in coincidence occurred, where N=1 to 4. In our case, BEAM and BEAM DEFEAT were mutually exclusive, as will be shown later, so both inputs were connected. Then, depending on whether the dimuon trigger or another trigger was desired, DIMUV or TRIG was selected via a pin on the logic unit. The logic unit was then set for a two-fold coincidence (N=2) and was always vetoed by the trigger veto (TV). Thus, the trigger consisted of BEAM·DIMUV·$\overline{TV}$ for dimuon running, BEAM·TRIG·$\overline{TV}$ for other triggers which demanded a beam particle, and (BEAM DEFEAT)·TRIG·$\overline{TV}$ for triggers which did not need beam. DIMUV signifies a dimuon signal in the M hodoscope and will be discussed later. BEAM indicates a "clean beam" particle and interaction in the target; TRIG indicates the appropriate trigger was observed in downstream hodoscopes and/or the gas Cerenkov counter. Let us consider each of these in turn.

BEAM is defined as CBH·PRV·(U/S TRIG)·$\overline{\text{(BEAM DEFEAT)}}$ and is shown in Figure C-2. Here CBH is a "clean" beam signature in the U/S beam hodoscopes. The requirement for this signature is that each of the four x-measuring U/S beam hodoscopes (BH1,BH2,BH3,BH5) have a single element hit, and none of the veto wall "jaws" (Vxx) or veto wall hodoscope elements (VWALL) are hit (BH1·BH2·BH3·BH5·$\overline{BV}$ where BV =

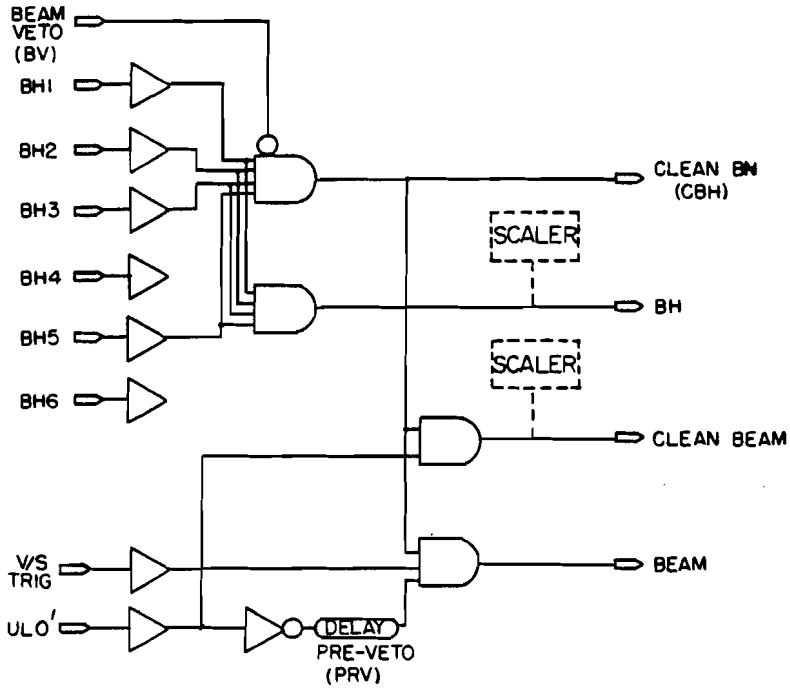

Figure C-2

Beam logic

VBE+VBW+VCE+VCW+VDE+VDW+VWALL). PRV represents the "pre-veto" signal; this signal was created from the complement of ULO', a logic signal representing a beam particle passing through the target, delayed by the interval between beam buckets and timed into BEAM. The purpose of this delayed signal was to veto events where another beam particle was found one accelerator RF bucket earlier than the candidate event; the bucket-to-bucket time being 1/(53 MHz)=18.9 ns. U/S TRIG symbolizes an upstream trigger defined in the upstream logic which will be discussed in detail later. BEAM DEFEAT vetoed BEAM and allowed event triggers without a beam particle. TRIG and DIMUV are shown in Figure C-3. TRIG and DIMUV represent the selection of trigger type by the coincidence of the desired event trigger and the Bison Box output register bit appropriate to the trigger type. This output register may be set by the on-line PDP-11/45 computer via MULTI, so any combination of trigger types was possible, although in almost all cases only a single trigger type was selected. The trigger types available and the corresponding Bison Box bit (BBn) were: the dimuon trigger (BB0), the charged K trigger (BB1), ULO or UHI (BB2), "Rover" (BB3), pulser (BB4), and halo (BB5). Additional Bison Box output register bits were used in the begin-run and between-spill calibration sequences, as will be explained later. Also, the out-of-spill bit (BB9) was on in conjunction with each of the above triggers to indicate that between-spill calibration records should be output to

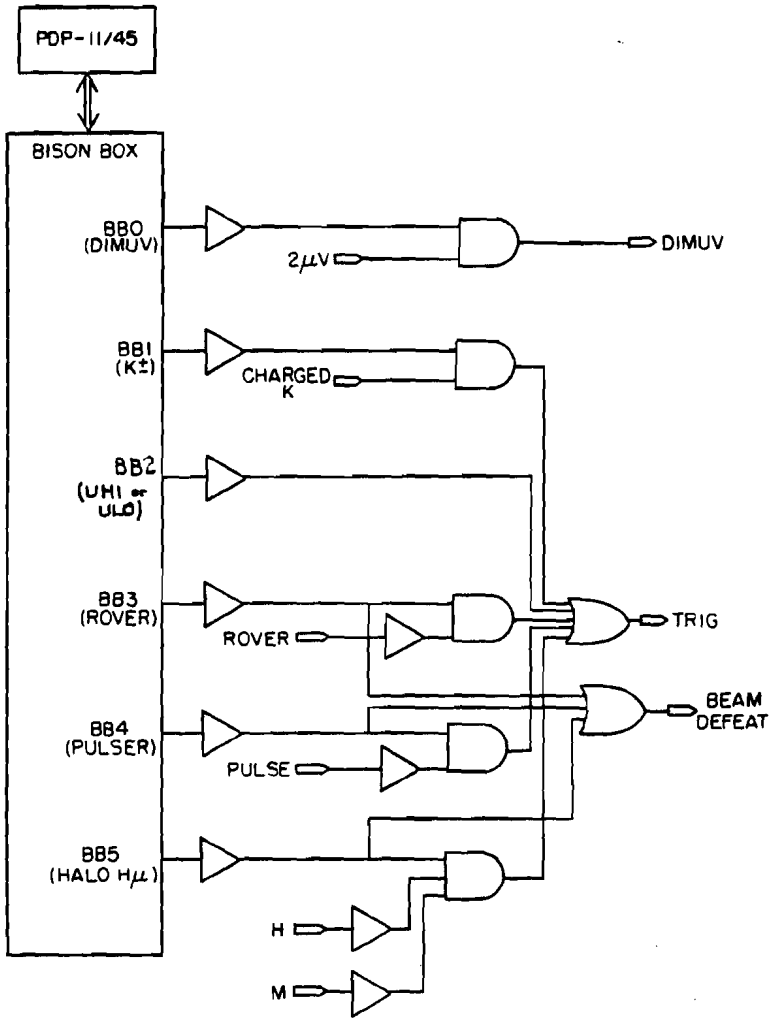

Figure C-3

Trigger logic

tape.

A short description of each of the trigger types is in order at this point; later, some types will be described in detail. The dimuon trigger was the normal running condition; this trigger required a clear dimuon signal in the M hodoscope with elements hit in opposite quadrants. The charged K (CK) trigger required one, two, or four charged kaon signatures in the gas Cerenkov counter; such a signature consists of a Cerenkov cell with no signal and a matching H hodoscope element with a hit. The UHI and ULO triggers are shown in Figure C-4. The UHI trigger consisted of a pulse height above a set threshold in T0, the small scintillator just before the target, and pulse heights above set thresholds in T1 and T2, the overlapping small scintillators just after the target. These signal were referred to as T0, T1-high, and T2-high, respectively. The ULO trigger only demanded T0, T1-low, and T2-low. T0, T1-low, and T2-low were discriminated such that at least a single beam particle would produce a logic pulse; T1-high and T2-high were attenuated and discriminated such that an average of two or more particles would produce a logic pulse. Thus, UHI is biased toward an interaction in the target and ULO is biased only toward a single beam particle passing through the target. The actual selection of UHI, ULO, or HALO was simply a matter of inserting a pin into the desired input selector at the logic module (a LeCroy NIM Model 364AL). UHI was necessary for the dimuon or charged kaon

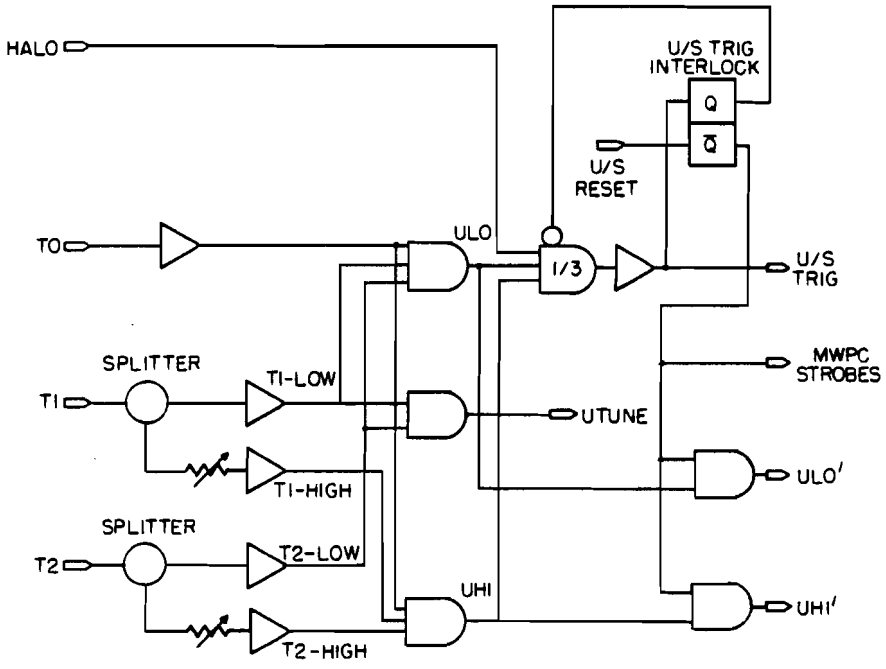

Figure C-4

Upstream logic

triggers, but BEAM (and therefore also UHI and ULO) was disabled for pulser, Rover, or halo triggers.

The Rover trigger used a small portable scintillator paddle ("Rover") as an input to the trigger so as to demand a particle at a specific location; this was useful in studying or trouble-shooting a specific piece of apparatus. The pulser trigger was used in conjunction with a pulse generator to trigger all the apparatus at any desired rate and without beam. This was useful in shaking down the apparatus and problem-shooting high rate effects. The halo trigger was used with beam but without beam particles; this trigger consisted of HALO H M—that is, at least one hit each in the veto jaws, the H hodoscope, and the M hodoscope. HALO was selected as the upstream trigger. This trigger was not a beam particle but a halo muon or cosmic ray which went through the entire apparatus; these were useful in calibrating portions of the apparatus which received few particles from interactions in the target.

The last component of MT is the trigger veto, TV, diagrammed in Figure C-5. The trigger veto consisted of BG+CBSY+(FAST KILL) where BG stands for the absence of the beam gate which was obtained from the Fermilab MAC system, CBSY represents "computer busy"—that is, the on-line PDP-11/45 was still recording and logging to tape the previous event—and FAST KILL was a special latch gated for 1 μs and started by

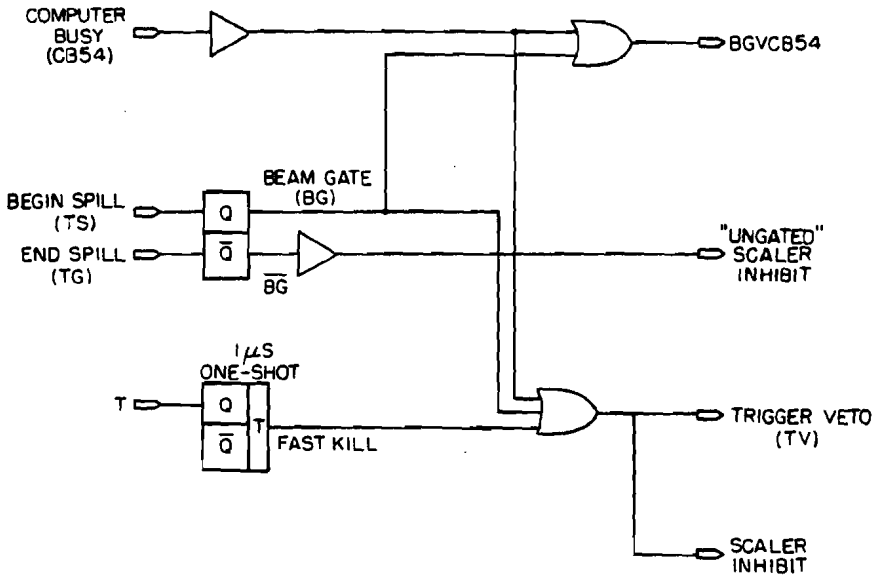

Figure C-5

Trigger veto logic

MT. The purpose of FAST KILL was to prevent recording a second event which occurred before the "computer busy" signal returned from the computer to the logic racks.

Figure C-6 shows how the master trigger signal is fanned out to initiate readout of all the equipment into the computer via CAMAC. The CAMAC TDC's for the M and H hodoscopes started timing from this fanout, the latch gate for the M and M' latches was initiated from this fanout; this signal served as the "load" signal for the 80 cm chambers' NANOMAKER readout system; the gate for the peak-voltage sensitive RIRODAC/LARC ADC system for the P-tubes was started by this fanout; and the ADC gates for the gas Cerenkov counter and the lead glass array were initiated by this fanout. Most importantly, the fanout of the master trigger served as Interrupt A into the Bison Box and thus, in turn, to the on-line computer. This interrupt controlled the readout of the CAMAC crates to the computer.

Figure C-7 and portions of the previous two figures illustrate the logic pertaining to the begin-run and between-spills calibration sequences. The capability of the on-line computer to change the Bison Box output register was incorporated in the begin-run calibration; the between-spills calibration was accomplished via hardware external to the computer. For the begin-run sequence, Bison Box output register bits BB6, BB7, and BB8 were employed and were named UFLASH,

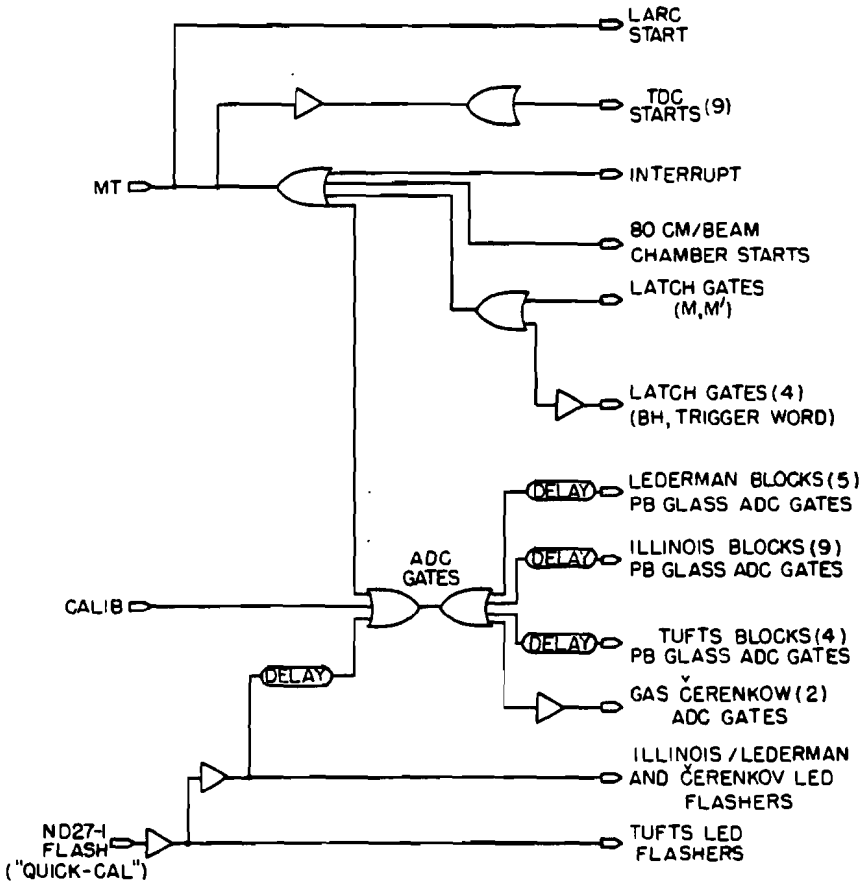

Figure C-6

Trigger fanout logic

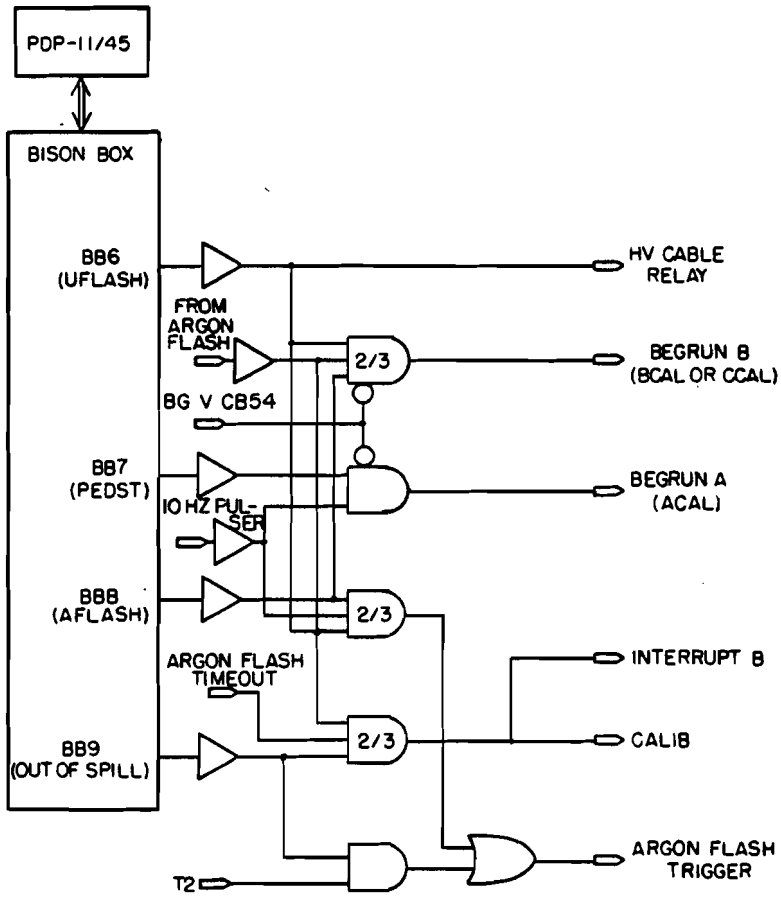

Figure C-7

Calibration logic

PEDST, and AFLASH, respectively. The on-line software controlled the begin-run sequence, first setting PEDST on for a fixed number of triggers (with a default of 100) to obtain pedestals for the ADC's, then setting UFLASH on for a fixed number of events (with a default of 50) where the transverse and longitudinal blocks were calibrated with their two separate argon flash lamp systems, and then setting AFLASH on for a fixed number of events (with a default of 50) where only the longitudinal blocks were calibrated by their argon flash lamp. This was accomplished by sending AFLASH to a high voltage cable relay which removed the high voltage from the Tufts argon flash lamp. The actual trigger to the argon flash lamp was (BB6+BB8)·(10 Hz pulser) which determines the rate at which calibration triggers were logged. However, the actual trigger to the computer was obtained from a discriminator which received a signal from a special phototube with a light fiber fixed to its face. This was necessary because the delay from when the argon flash lamp received its trigger to when it actually flashed was variable. Occasionally, no flash would occur; therefore an argon flash lamp time-out was derived from the argon flash lamp trigger, so that the logic would not become locked. The pedestal portion of the begin-run sequence was formed of PEDST and the pulser and vetoed by the beam gate and "computer busy"--that is, $BB7\cdot(10\text{ Hz pulser})\cdot\overline{(BG+CBSY)}$. This logic signal was referred to as Begrun A or ACAL in MULTI. Similarly, Begrun B consisted of either

BB8·(10 Hz pulser)·(argon flash disc)·$\overline{(BG+CBSY)}$ for AFLASH (known to MULTI as BCAL), or BB6·(10 Hz pulser)·(argon flash disc)·$\overline{(BG+CBSY)}$ for UFLASH (known to MULTI as CCAL). Begrun A or B were then ORed into the master trigger. Thus, these begin-run calibration records have the same format as normal event records.

On the other hand, between-spill calibration records have a different format and utilize the other available interrupt on the Bison Box known as Interrupt B. The logic signal for Interrupt B (CALIB) was (argon flash disc)·(argon flash timeout)·BB9 where BB9 was the Bison bit for between-spill triggers. The argon flash lamps were actually triggered by BB9·T2 where T2 is a signal originating from the MAC which falls between spills. Figure C-6 shows how CALIB is used to trigger digitizing of only the ADC gates.

Calibration signals from LED's flashed onto the lead glass blocks occurred after every event via the interaction of the on-line computer and special software within MULTI. When MULTI finished the readout of the CAMAC crates, it cleared the ADC's and set a single-bit output register in CAMAC crate 1 (MAC CAMAC Model ND027). The discriminated signal from this register was fanned out first to the LED flashers and then to the ADC gates, which were then read in again via CAMAC. This calibration sequence was referred to as the "quick calibration" or "quick-cal" and is shown in Figure C-6.

Special fast logic had to be devised for the U/S area because the Illinois chambers' electronics needed a load signal immediately after an interaction; otherwise, further interactions would add accidental hits to the real hits associated with this event. Thus, a logic rack containing the logic shown in Figure C-4 was placed right above the Illinois chamber electronics. This was where ULO and UHI were actually formed, near the target scintillators. ULO, UHI, or HALO was selected by a pin in the logic module. The output signal provided the U/S trigger which, in addition to forming part of the master trigger, was used as the load signal for the Illinois chambers and the drift chambers. Further load signals were inhibited by a flip-flop which was reset by the U/S reset. As can be seen in Figure C-1, this reset was either a fast reset (R) due to the trigger conditions not being met or a slow reset due to a single-bit register (MAC CAMAC Model ND027) set on by the PDP-11/45 after data collection was completed for an accepted event. The U/S reset initiated the strobe to the Illinois chambers and the drift chambers which caused the transmission of the chamber data from the electronics to the custom CAMAC modules in preparation for read-out by the on-line computer. ULO' and UHI' were formed from the coincidence of ULO and UHI with the reset signal from the flip-flop.

Now I will describe some of the logic signals that have only been mentioned as inputs so far in more detail. The beam veto and halo logic is shown in Figure C-8. The veto hodoscopes are described in the apparatus chapter. A veto wall logic pulse (VWALL) was formed by the union of all twenty veto wall hodoscope elements' signals and the four veto wall veto jaws' signals. This in turn was ORed together with the beam veto jaws located in Enclosure 104 to create the beam veto (BV) signal. A separate union of the veto wall veto jaws was formed to create the HALO signal. In conjunction with the required H and M signals required for TRIG, a HALOHM trigger was caused by one or more particles which passed through the veto wall jaws, the H hodoscope, and the M hodoscope.

Each H hodoscope element's anode output was discriminated and then timed in a TDC (LeCroy CAMAC Model 2228A). The eight-channel discriminators (LeCroy NIM Model 620BL) had an "OR out" signal; these ORs were than put in union to create the H logic signal which represented any H element hit. Also, certain combinations of the H elements entered into the charged K trigger, as will be explained shortly.

The M hodoscope logic was more complicated (Figures C-9 and C-10). The logic rack in which the following triggers were formed sat atop the steel hadron absorber near the M hodoscope for timing

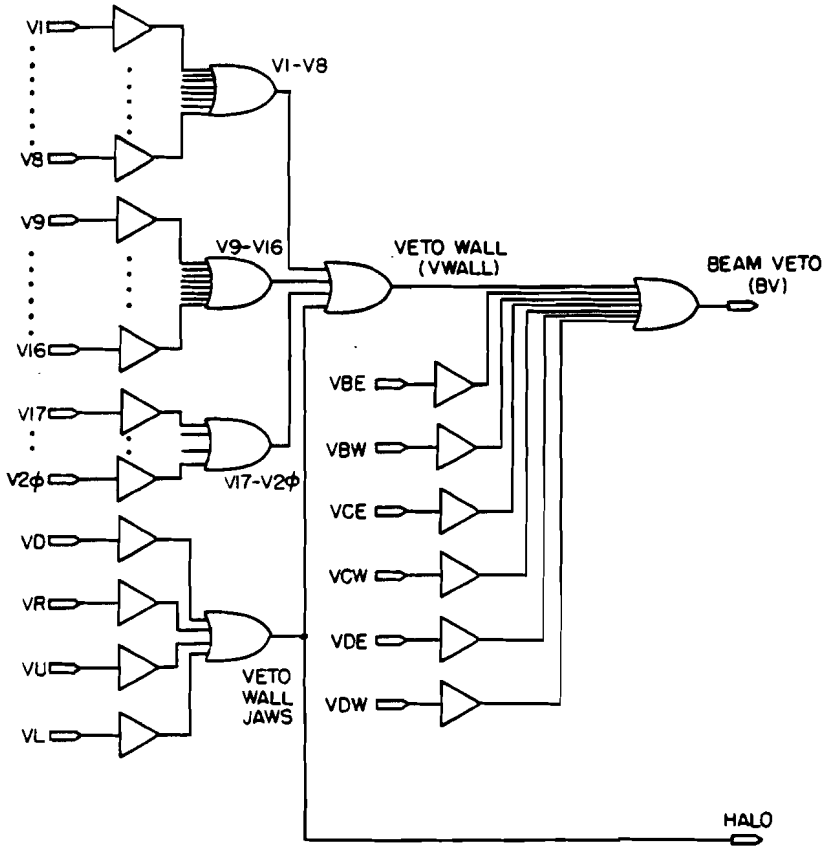

Figure C-8

Beam veto and halo logic

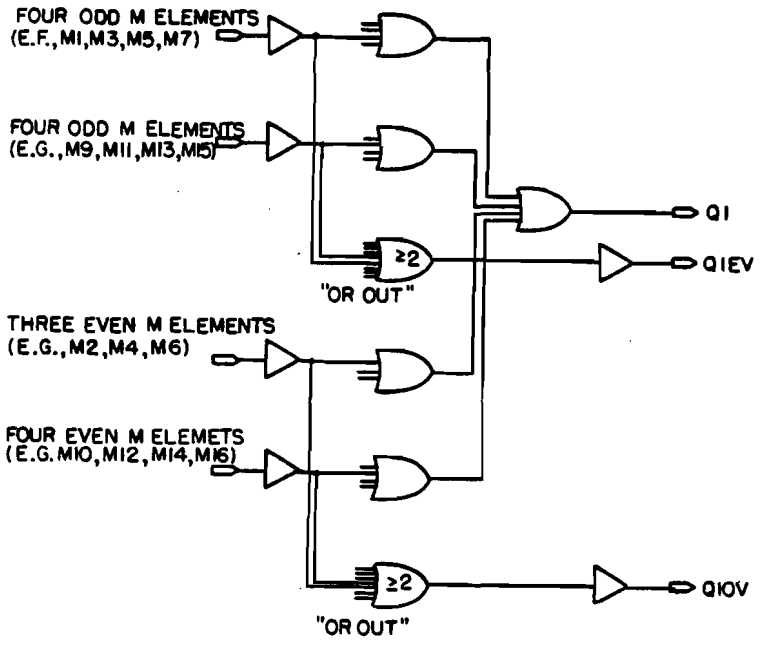

Figure C-9

M hodoscope quadrant logic

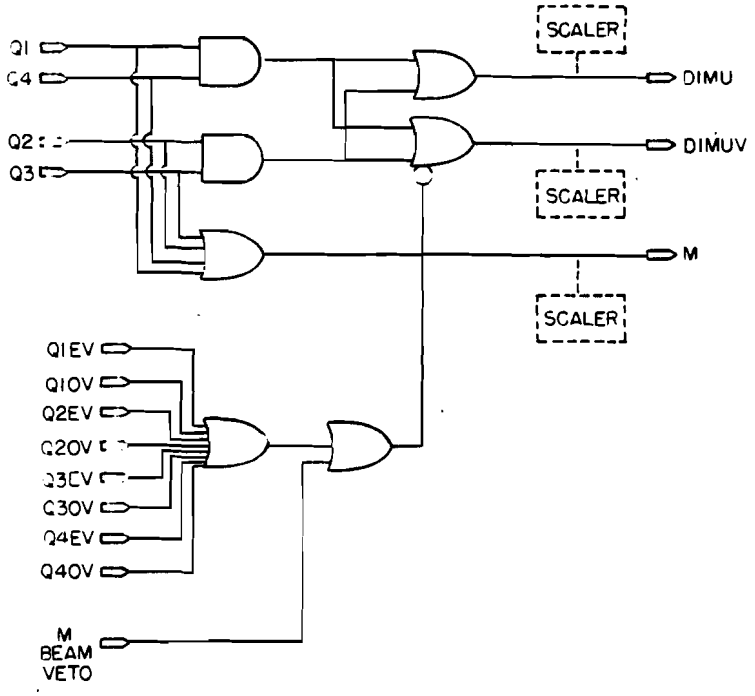

Figure C-10

M hodoscope logic

reasons. Two outputs were derived from it--M, which represented any M element hit; and DIMUV, which represented two hits in opposite quadrants of the M hodoscope. Each quadrant of the M hodoscope nominally consisted of fifteen elements and fifteen discriminated inputs were actually formed in the logic; however, only twelve physical counters existed for each quadrant. The actual selection of counters used in the dimuon trigger is discussed in detail in the apparatus section. Each quadrant was divided into two groups, the even-numbered and the odd-numbers counters, for eight groups of seven or eight elements each. Each discriminated signal from each counter was also latched, and each group was ORed in two units of four or three elements each, the output of which provided a TDC stop signal. Again, these signals were discriminated in the logic unit with an "OR out". This "OR out" signal had a variable discrimination level so that an output logic signal could be produced if two or more inputs produced logic pulses instead of one. These eight "OR out" signals were set in such a manner and vetoed the DIMUV signal in conjunction with a beam veto counter which sat directly behind the M hodoscope; thus, any quadrant could have at most one odd and one even element hit for the DIMUV signal. The purpose of this veto was to avoid large-angle showering in the steel hadron absorber during hadron punch-through. The possibility of adjacent counters firing had to be admitted because of the overlap between adjacent counters. An

additional veto was a logic signal from a small beam veto counter located at the center of the M hodoscope. This prevented punch-thru of beam particles from inducing a dimuon trigger. The discriminated M element pulses were also ORed for each quadrant; then a coincidence of opposite quadrants was demanded for the DIMUV signal. Also, all the M elements were ORed together to give the M signal.

The charged K (CK) trigger was output when a gas Cerenkov counter was not hit with one of the matching H elements behind it hit, corresponding to a charged kaon passing thru the Cerenkov and the H hodoscope with a momentum below the Cerenkov threshold for kaons. Only the middle eight Cerenkov cells and their matching H hodoscope elements were included in this trigger as shown in Figure C-11. Actually, as shown in Figure C-12, the trigger could be arranged several different ways by pin selectors in the final logic unit (LeCroy NIM Model 364AL). Almost always, the trigger was selected to be a dikaon trigger by demanding a coincidence of the K-west and K-east outputs; but once the trigger was selected to be four or more kaon signatures using the multiplicity unit (LeCroy NIM Model 380).

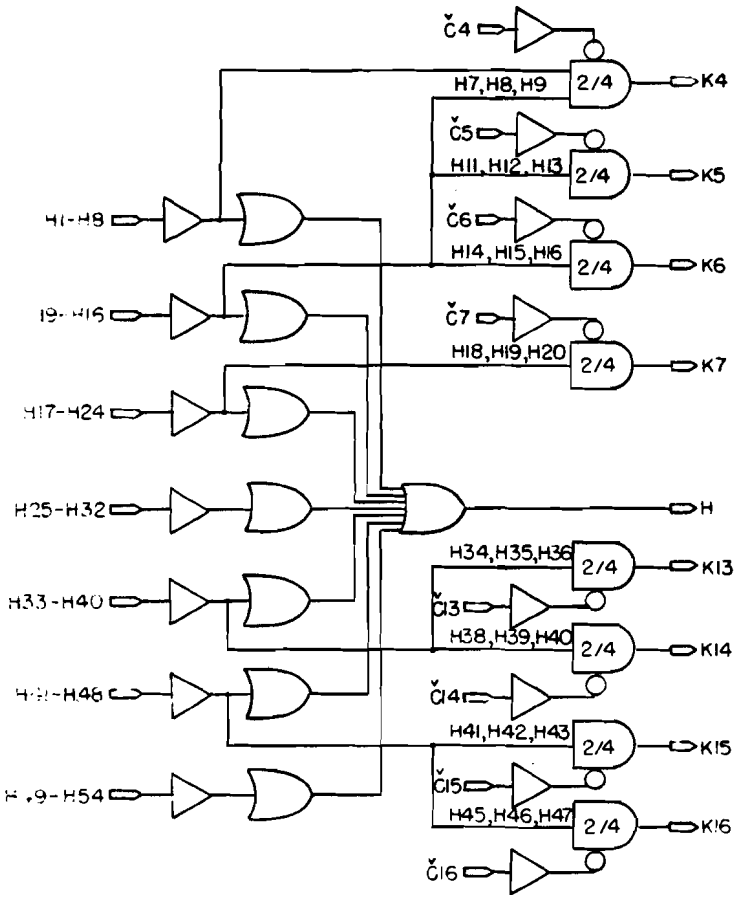

Figure C-11

H hodoscope logic

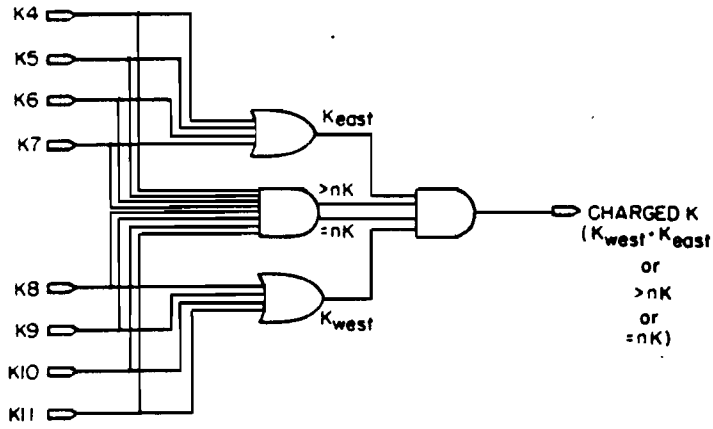

Figure C-12

Kaon trigger logic

REFERENCES

J.G. Abolins et al., Phys. Lett., 82B, 145 (1979)

G. Altarelli, Phys. Rep. 81, 1 (1982)

K.J. Anderson et al., Phys. Rev. Lett. 42, 944 (1979)

J.J. Aubert et al., Phys. Rev. Lett. 33, 1404 (1974)

J.E. Augustin et al., Phys. Rev. Lett. 33, 1406 (1974)

R. Barbieri, R. Gatto, and R. Kogerler, Phys. Lett. 60B, 183 (1976)

N.N. Biswas et al., Nucl. Phys. B167, 41 (1980)

J.D. Bjorken and S.L. Glashow, Phys. Lett. 11, 255 (1964)

S. Brandt, Statistical and Computational Methods in Data Analysis, 2nd edition, North-Holland Publishing Company (1970)

M.A. Branson et al., Phys. Rev. Lett. 38, 1331 (1977)

H.S. Budd, Ph.D. thesis, University of Illinois, 1983

A.J. Buras, "A Tour of Perturbative QCD", Conference on Photon and Lepton Interactions (1981)

CAMAC Diagnostic Language, Joseph R. Biel, Fermilab PN-93.1 (1978)

CAMAC DVM Control for the HP3485, Fermilab HN-10.1 (1972)

CAMAC, A Modular Instrumentation System for Data Handling, AEC NIM Committee Standard TID-25875 (1972)

CAMAC Organization of Multi-Crate System, AEC NIM Committee Standard TID-25876 (1972)

CAMAC Serial System Organization, AEC NIM Committee Standard

TID-26488 (1973)

C.E. Carlson and R. Suaya, Phys. Rev. D14, 3115 (1976)

F.E. Close, An Introduction to Quarks and Partons, fourth edition, Academic Press, New York, 1981

E-610 Muon Lab RTMULTI System Characteristics, Fermilab PN-196, T.Lagerlund and S.R.Hahn (1980)

C.O. Escobar et al., CBPF-NF-006/81 (1981)

J. Feller, "CASCADE - Electromagnetic Shower Simulation", private communication (1975)

Fermilab "Bison Box" Manual., HN-3 (1978?)

Fermilab Experimental Areas Control System Computer Users' Manual (MAC manual) (1974)

Fermilab MULTI User's Guide, PN-97.4 (1978)

M. Gell-Mann, Phys. Lett. 8, 214 (1964)

S.L. Glashow, J. Illiupoulos, and L. Maiani, Phys. Rev. D2, 1285 (1970)

V.A. Hanin and B.E. Stern, Nucl. Instr. and Meth. 157, 455 (1978)

S.W. Herb et. al., Phys. Rev. Lett. 39, 252 (1977)

S. Hossain, Ph.D. thesis, Tufts University, 1981

J. Iizuka, Prog. Theoret. Phys. Suppl. 37-38, 287 (1977)

R. Jackiw and S. Weinburg, Phys. Rev. D5, 2396 (1972)

R.L. Jaffe and K. Johnson, Comments Nucl. Part. Phycs. 7, 107 (1977)

T.B.W. Kirk et al., Phys. Rev. Lett. 42, 619 (1979)

LeCroy Technical Data sheets, LeCroy Research Systems Corporation (1973-1978)

E. Longo and I. Sestili, Nucl. Instr. and Meth. 128, 283 (1975)

Y. Lemoigne et al., Phys. Lett. 113B, 509 (1982)

H. Matis, Ph.D. thesis, University of Chicago, 1975?

P.Malhotra and R.Orava, Z. Phys. C17, 85 (1983)

Y. Nambu, Phys. Rev. D14, 4262 (1974)

Y. Ne'eman, Nucl. Phys. 26, 222 (1961)

V.A. Novikov et al., Phys. Reports 33C, 287 (1977)

Perfection Mica Company, Magnetic Shield Division, Material and Fabrication Guide (1976)

M. L. Perl et al., Phys. Rev. Lett. 35, 1489 (1975)

C. Peterson, proceedings of the Topical Workshop on Forward Production at High-Mass Flavors at Collider Energies, College de France, Paris (1979)

S. Pordes, Ph.D. thesis, Harvard University, 1976

J. Proudfoot, Ph.D. thesis, University of Oxford, 1978

Review of Particle Properties, Particle Data Group, LBL-100, April 1982

P.V. Schoessow, Ph.D. thesis, University of Illinois, 1983

V.Shekhter and L.Shcheglova, Sov. J. Nuc. Phys. 29, 567 (1978)

Standard Nuclear Instrument Modules, AEC NIM Committee Standard TID-20893 (Rev. 4) (1974)

Supplementary Information on CAMAC Instrumentation System, AEC NIM Committee Standard TID-25877 (1972)

C.N. Yang, Phys. Rev. 77, 242 (1950)

G. Zweig, "An SU(3) Model for Strong Interaction Symmetry and Its Breaking" (1964), Developments in the Quark Theory of Hadrons, edited by D.B. Lichtenberg and S.P. Rosen (1980)

VITA

Steve Hahn was born in 1950 in Chicago, Illinois. He attended public schools in Decatur, Illinois and graduated from Stephen Decatur High School in June, 1969. Within five years, this school had been razed to the ground. He attended the University of Illinois as an undergraduate beginning September, 1969. He received his B.S. in Physics in 1972 and his M.S. in 1973. He then left the academic environment for almost three years, taking up employment as a computer programmer in the "real world" and getting married to boot. He returned to the University of Illinois in 1976. During his graduate career, he held teaching and research appointments.